universität wien

DIPLOMARBEIT

Titel der Diplomarbeit

Radiative Transfer Effects on the Lyman-Alpha Forest

(Strahlungstransport Effekte im Lyman-Alpha Wald)

angestrebter akademischer Grad

Magister/Magistra der Naturwissenschaften (Mag. rer.nat.)

Verfasserin / Verfasser:	Adrian Manfred Partl
Matrikel-Nummer:	0206521
Studienrichtung (lt. Studienblatt):	A 066 861 Astronomie UG2002 Magisterstudium/Masterstudium
Betreuerin / Betreuer:	Prof. Dr. Gerhard Hensler

Wien, am 13. Nov. 2007

Lebenslauf

Adrian Manfred Partl

Persönliche Information

- Geburtsdatum: 16. August, 1982
- Geburtsort: Zürich, Schweiz
- Staatsangehörigkeit: Schweiz und Österreich

Ausbildung

1989 - 1995	Primarschule	Reichenburg, SZ, CH
1993 - 1994	1- jähriger USA-Aufenthalt Besuch der Middle School	Philomath, Oregon, USA
1995 - 1996	Gymnasium Nuolen Matura Typus B (Latein)	Nuolen, SZ, CH
1996 - 1998	Bezirksschule	Frick, AG, CH
1998 - 2001	Gymnasium Muttenz Matura Typus E (Wirtschaft) Erfolgreicher Abschluss des Gymnasiums am 14.12.2001 mit 73 Punkten	Muttenz, BL, CH
2002 – 2005	Bakkalaureatsstudium der Astronomie. Abschluss mit Auszeichnung am 14.10.2005	Wien, AT
Seit 01.10.2005	Magisterstudium der Astronomie Universität Wien	
Seit 01.10.2006	Beginn der Magisterarbeit in Zusammenarbeit mit dem Astrophysikalischen Institut Potsdam zum Thema „Radiative Transfer Effects on the Lyman-Alpha Forest“	

Abgabe der Magisterarbeit Ende November 2007

Vertiefende Ausbildung und Praktika

August 2003	Praktikum an der EMPA Dübendorf
Sommer 2005	Praktikum am Astrophysikalischen Institut Potsdam
Sommer 2006	Sommerschule „Supercomputational Cosmology“

Unterrichts-erfahrung

SS 2006	Tutor der Vorlesung „Einführung in die Astronomie 2“ bei Prof. Dr. Gerhard Hensler

Vorträge und Konferenzen

30.09.2006	Fachtagung AG – *Elektronische Facsimile-Editionen von ausgewählten Werken der Sammlung an der Universitätssternwarte Wien*
3. – 7.09.2007	Radiative Transfer Workshop ICC Durham UK – *Radiative Transfer Effects on the Ly-alpha Forest*
24.–29.09.2007	80th Annual Scientific Meeting of the AG in Würzburg – *Radiative Transfer Effects on the Ly-alpha Forest*

Potsdam den 13.11.2007

Radiative Transfer Effects on the Lyman-α Forest

Adrian Partl
Diplomathesis

In supervision by:
Prof. Dr. Gerhard Hensler (University of Vienna)
Dr. Volker Müller (Astrophysical Institute Potsdam)

To Manfred, Ruth, and Bettina

Contents

1 Introduction

Cosmological computational science is a rapidly evolving field in astronomy. Thanks to growing computational power almost every aspect of astronomy can be modeled using numerical simulations. This is true for all the different scale lengths, be it planetary formation, galaxy evolution or the evolution of the universe. Large success stories can be told in N-body simulations, hydrodynamics and magneto-hydrodynamics. Using grid or tree-codes it is possible to simulate up to $N = 2160^3$ particles, which is the current record holder in a gravity only simulation (the Millennium simulation by Springel et al. (2005)). In the hydrodynamic and MHD regime, one of the most impressive simulations is the one by de Avillez and Breitschwerdt (2005) of the interstellar medium using adaptive mesh refinement AMR techniques. They are able to resolve up to 1.25 pc in a $1\,\mathrm{kpc}^2 \times 10\,\mathrm{kpc}$ box.

In one discipline, this picture is not completely true. One physical quantity is still very hard to solve for and only in recent times did algorithms for solving this quantity emerge. This is the radiative transfer equation. A wealth of experience has been gained in stellar astrophysics on how to solve this equation, and very impressive results can be obtained with these methods. Unfortunately, these methods are only applicable for very special cases: stars.

The complexity of the transfer equation is reduced by special assumptions or exploitations of symmetries. This strategy cannot be used in more general cases, like radiative transfer in cosmological simulations. Symmetries do not exist and to make things worse, the optical depths are too low, that any locality can be assumed. Localities make things a whole lot easier.

In this work we want to pick up an existing algorithm for general radiative transfer calculations and apply this to a cosmological setting. We want to verify a simplistic model of the Lyman-α forest, and check it with a more accurate description by incorporating effects neglected in these analytical prescriptions. Dense filaments absorb the UV background and can reduce the radiation field around them. Then recombining electrons produce a diffuse radiation component, which might also influence results. These effects are observable in the synthetic spectras we construct and can be analysed statistically.

We show, that these effects do not influence the Ly-α forest greatly, but still to a noticeable extend. Shadowing around dense filaments increases the optical depths near them and hints are seen, that this affects statistical properties of the forest. A diffuse component only plays a minor role in the Ly-α forest, but still it is noticeable. It is possible that we still underestimate the effect, due to the difficulties in simulating recombination radiation.

In order to solve the question of photoevaporation of dwarf galaxies, any numerical code has to perform well in solving the transfer equation. This is also important in the question of which objects are responsible for the UV

background at low redshift.

We can demonstrate, that our code is capable of being used in cosmological setups at low redshift, at least in the context of the Ly-α forest. Up to now, radiative transfer codes have only been applied to the high redshift regime. No one tried to check, if the transfer solvers do a good job in the low density regimes at low redshift.

Radiative transfer is a very exciting new field in astronomy. Due to the fact, that almost all the data collected by observers stem from photons, it is even more interesting to see how photons propagate in the universe.

The structure of this thesis will be as such. First we want to motivate the reader for our work and give a short introduction to the Lyman-α forest and the diverse field of cosmological radiative transfer. Different methods for solving radiative transfer are introduced to put the method used in this thesis into the broader context.

We then want to discuss the model of Hui and Gnedin for the Lyman-α forest in detail. This is the model we want to check and refine using radiative transfer. For this, we study the model in great detail. We address possible objections and develop models to use with our dark matter only cosmological simulations. Of course these models need to mimic observational findings.

In the next chapter we then want to develop the numerical scheme for simulating radiation in a cosmological context. We then test our version of the scheme extensively to make sure that it is working and we study limitations of the scheme. Then we can apply our code to the Lyman-α forest and obtain results from our detailed model. These results are then analysed and we will focus on differences between the Hui and Gnedin model and ours. These results are then discussed and we draw our conclusions.

1.1 Motivation

When pointing a preferably big telescope to a high redshift quasar, and attaching a preferably high resolution spectrograph to it, one will get a spectrum similar to the one in Figure 1.1.1. If the redshift is high enough, the ultra-violet (UV) Ly-α emission line ($1215.67\,\text{Å}$) of the QSO (Quasi Stellar Object / quasar) will be redshifted sufficiently to be visible, as is the case in the spectrum presented here. The emission line is located at the right side of the plot, around $5600\,\text{Å}$.

Blueward of this emission line one can see a wealth of different absorption lines, called the Lyman-α forest. In 1971 Lynd was puzzled by unidentifiable absorption lines blueward of the Ly-α emission line. He proposed, that these lines in his spectrum of 4C 05.34 could be Ly-α lines lying at lower redshift than the observed QSO. He stems this argument from the fact, that all these absorption lines lie blueward of the Ly-α emission line (Lynds (1971)).

That these lines are really Ly-α absorption lines has been proved by looking for correlated Ly-β lines (Oemler and Lynds (1975)). Then the question arose, whether these Ly-α absorption lines are produced by intervening clouds at different redshifts, or whether these clouds are ejectas of the QSO itself. Sargent

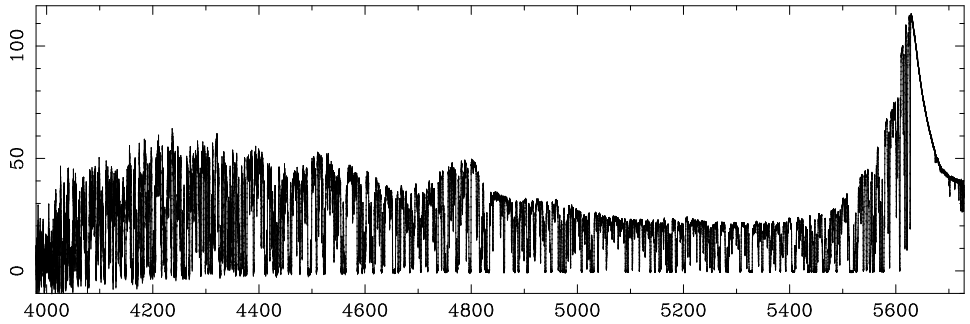

Figure 1.1.1: High resolution spectrum of the $z_{em} = 3.62$ QSO1422+23 ($V = 16.5$), taken with the Keck High Resolution Spectrograph (HIRES). Plot taken from Rauch (1998). The horizontal axis gives wavelength in $\mathrm{\AA}$, while the vertical axis gives photon flux in arbitrary units.

et al. (1980) analysed six QSO spectra and came to the conclusion, that if these clouds were ejected by the QSO, they would need to have enormous velocities of up to 20% of the speed of light. Also, the distribution of the number density was similar in all their QSOs. A fact that cannot be easily explained with ejected media.

They conclude, that these lines are produced by different hydrogen Ly-α absorbers at different redshifts. By analysing the lines in more detail it can be seen, that not all lines are produced by hydrogen only, but some are caused by metals like Si, O, C, N and others (see Schaye et al. (2007), Rauch et al. (2001), Cowie et al. (1995) and many more). This complicates any analysis of observational data. On top of this forest of absorption lines one can see the varying continuum spectrum of the QSO.

Each absorption line has a specific profile, called the Voigt profile. By fitting such profiles to the absorption lines, one can measure column densities and the temperature of these systems. Ly-α forest lines have column densities below $N(HI) < 10^{17}\ \mathrm{cm}^{-2}$ (Rauch (1998)). With higher column densities the gas becomes optically thick to UV photons. At densities between $10^{17} < N(HI) < 10^{19}\ \mathrm{cm}^{-2}$ the wings of the absorption line start to produce a dip in the continuum. In these systems, hydrogen is still neutral enough, so that radiation emitted by the quasar below $\lambda < 912\mathrm{\AA}$ is totaly absorbed in the Lyman limit. This results in a totaly saturated line. Such systems are called Lyman Limit Systems LLS (Rauch (1998)). At densities above $N(HI) > 10^{19}\ \mathrm{cm}^{-2}$ a deep trough is visible in the Ly-α forest. These features are called Damped Lyman Alpha systems DLA. All these different systems can be seen in a beautiful plot by Charlton et al. (2000) reproduced here in Figure 1.1.2.

Different statistical properties can be derived to characterise the Ly-α forest. In the course of this work we will look closer at some of the statistical properties, like transmission or temperature statistics. For a good overview of all

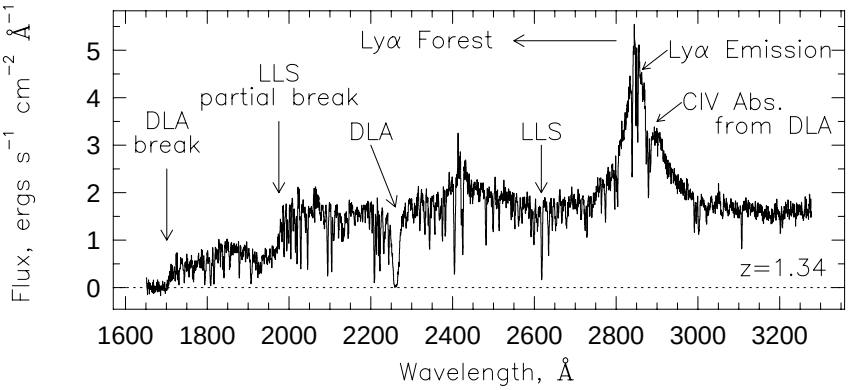

Figure 1.1.2: Spectrum of the $z_{em} = 1.34$ PKS0454+039 quasar showing all possible absorption features in the Ly-α forest. Plot taken from Charlton et al. (2000)

the properties of the Ly-α forest see the review by Rauch (1998). One of the interesting statistical measures is the line number density dn/dz. It describes the evolution of the forest in time and is given by a power law

$$\frac{dn}{dz} = \left(\frac{dn}{dz}\right)_0 (1+z)^{\gamma} \tag{1.1.1}$$

where $(dn/dz)_0 = 9.06 \pm 0.40$ for $z > 1.5$ and $\gamma = 2.19 \pm 0.27$ for $N_{HI} = 10^{13.64-16}$ cm^{-2} as is derived by Kim et al. (2001).

This is only true if measurements are taken well outside the influence of the QSO. Something interesting happens near the Ly-α emission line of the QSO. Slightly blueward to the emission line, the line number density decreases if one approaches the emission line. This lack of absorption near the QSO is called the proximity effect (Bajtlik et al. (1988)). In the surroundings of the QSO the UV background flux is enhanced by the quasar's own flux. Therefore any absorbing cloud in the vicinity of the QSO is more ionised, which results in a reduction of Ly-α line number density near the QSO.

Simple analytical models exist with which observers are able to derive numerous properties, like the UV background flux. The proximity effect is also a very good test case for any radiative transfer code. It could be, that inhomogeneities caused by shadowing could influence the effect. Whether this influences the way observers analyse the proximity effect needs to be studied. With the work presented here, this would be possible. One study going into this direction has be done by Maselli et al. (2004). Their findings are interesting, since they could not find any big influence of a source on its surroundings, except if they assumed extremely high star formation rates in the galaxy they studied.

The first theoretical modeling of Ly-α lines was done by Spitzer in 1956. He concluded, that galaxies have large gaseous halos giving rise to the absorption lines seen in the forest. The idea that these Ly-α absorption lines stem from

pressure confined clouds between the observer and source was discussed heavily in the literature until 1997 when Hui and Gnedin ended the discussion.

The two proposed a model based on outputs of cosmological dark matter simulations. By mapping dark matter densities to gas densities and applying a simple ionisation model, they were able to synthesize Ly-α spectra by picking random lines of sights through their box. A statistical analysis of their spectra revealed all the observed statistical properties, with which the discussion about the origin of the forest ended. The Ly-α is thus a direct consequence of the filamentary structure of the universe.

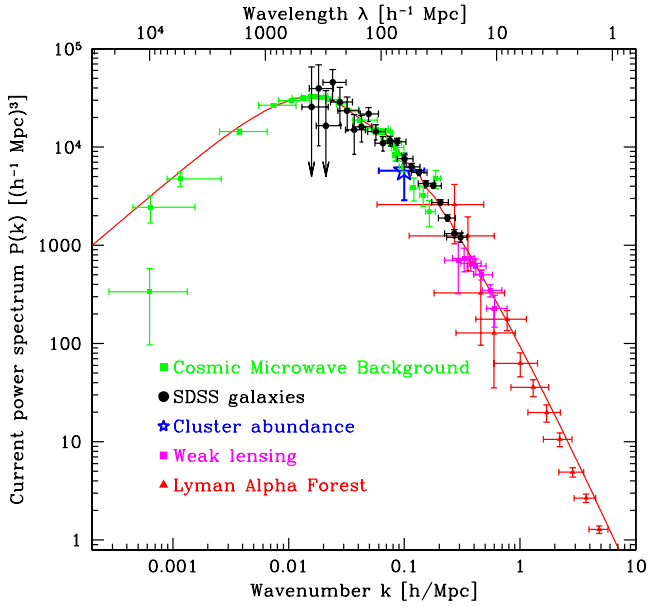

Figure 1.1.3: The power spectrum as measured by Tegmark et al. (2004). The Ly-α forest is capable of probing small scales of the universe. Measurements of the Ly-α forest constrain the power spectrum at higher wavenumber k.

The Ly-α forest is thus a very interesting tool to probe the structure of the universe. It is like a fingerprint off all the structure on the spectra of a quasar. It is therefore not surprising, that the Ly-α forest can be used to determine the small scale part of the density power spectrum. Using the Ly-α forest, the cosmological models can be better constraint. The forest determines the shape of the higher wavenumber part of the power spectrum. This is best seen in a plot by Tegmark et al. (2004) reproduced in Figure 1.1.3. A good understanding of the physics in the Ly-α forest is thus very important for understanding our universe better. It will help observers obtain better data for constraining the evolution of our universe.

1.2 Cosmological Radiative Transfer

Solving radiative transfer in unspecified geometry is not an easy task. In principle one needs to solve the seven dimensional transfer equation. Since this is an impossible task, at least with today's and near future computers, some other strategies need to be thought of.

Solving the transfer equation for the very special case of Local Thermal Equilibrium LTE is relatively easy and straight forward. Radiation effects only influence its surroundings locally, making things a lot easier. This approximation is applicable in a dense medium or to put it in a numerical formulation, when the mean free path of a photon is smaller than the cell size. If this is not the case, radiation from a totally different place reaches the cell and affects quantities there. One cannot speak of LTE anymore (Choudhuri (1998)) and things start to get complicated.

Some strategies exist to calculate radiative transfer and we want to present them briefly. This shall not be an excessive discussion of all the available codes, for this we want to guide the reader to the cosmological radiative transfer code comparison project by Iliev et al. (2006). Since no analytical way of solving the transfer equation exists, one needs to compare each code with the others to see, if several methods reveal comparable solutions or not. But even then it is not granted that a particular scheme is correct. How difficult all this is, can be seen in the fact that all the different codes do not necessary agree with each other.

The code comparison project takes 11 codes of participating groups and solves the same problems with each code. The output is then compared with all the other codes. By doing this it is possible to see how well each scheme performs and maybe why problems exists.

The simplest test case for a radiative transfer code is an isothermal Strömgren sphere. Results of the codes for its size vary by about 5% to the analytical solution. The difference starts to grow if photoheating is turned on in the calculation. In this case, the variation grow to 10%.

The point where no code really agrees is in the thickness and structure of the ionisation front itself. Some codes produce thicker fronts, since the medium outwards of the sphere gets preheated by different processes. And there the disagreement starts. Some codes implement recombination radiation, which allow preheating of the medium in front of the HII region through a diffuse radiating front. Others are able to calculate the transfer equation at different wavelengths, allowing higher energy photons to penetrate the ionisation front well into the medium lying ahead of it. Other only solve a monochromatic case. How greatly these solutions (especially in the temperature domain) vary is shown in a reproduction of Figure 14 of the comparison project's first paper, given here in Figure 1.2.1.

One observation that can be made is that at least all the ray tracing codes (C^2-Ray, CRASH, ART, RSPH, IFT) agree more or less. The problem lies more in matching results of other methods and to understand the differences.

Now is the time to discuss different codes and quickly introduce the reader to each method. With this it will be understandable, where or at least why all

these differences arise. This will also put the method used in this work in a broader picture.

Ray-Tracing The most widely used method for solving the radiative transfer equation is ray-tracing. In this method, the transport equation is solved using grids. Many different codes use the principles of this method, but implementation and the strategy on how the physics is solved varies from code to code. Ray-tracing is in fact widely used in a somewhat modified way by the computer graphics industry.

Some of the codes using ray-tracing are C^2-Ray (Mellema et al. (2006)), ART (Nakamoto et al. (2001)), FTTE (Razoumov and Cardall (2005)), the hybrid characteristics FLASH-HC code (Rijkhorst et al. (2006)), the radiation hydrodynamics code ZEUS-MP (Whalen and Norman (2006)), and a Monte-Carlo version called CRASH (Maselli et al. (2003)).

The common denominator of all these codes is, that they cast rays through the computational domain and solve the radiative transfer equation along these lines. This can be done in two different ways. The first method is to cast a ray from the source to each cell in the domain. This is called the long character-

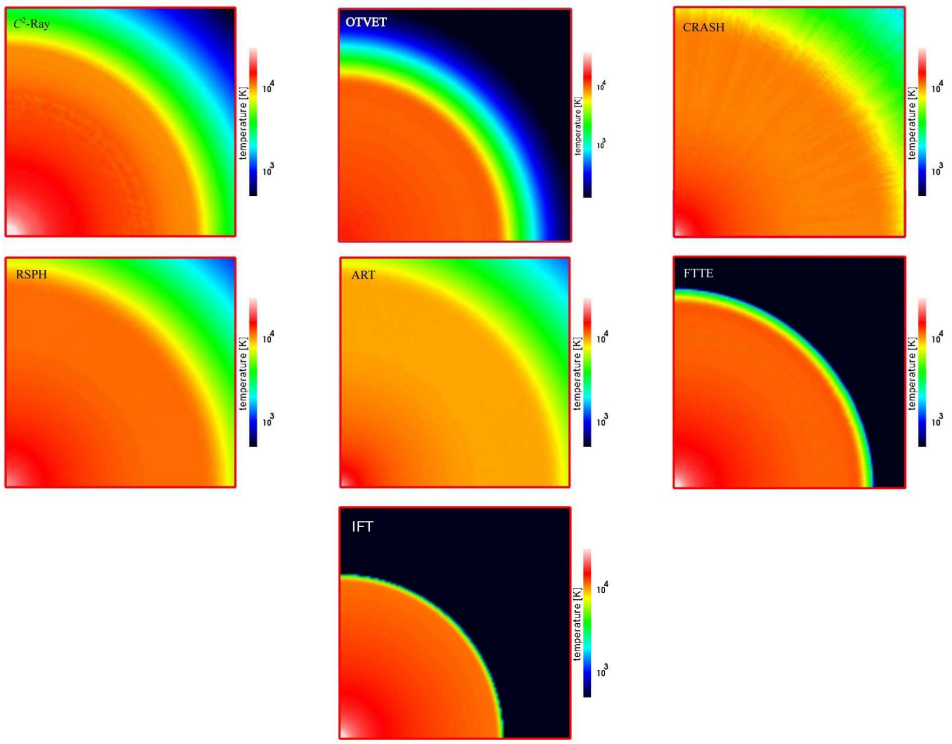

Figure 1.2.1: Test 2 (H II region expansion in an uniform gas with varying temperature) of the Comparison Project Iliev et al. (2006): Images of the temperature, cut through center of the simulation volume at time $t = 100\,\mathrm{Myr}$ for C^2-Ray, OTVET, CRASH, RSPH, ART, FTTE, and IFT.

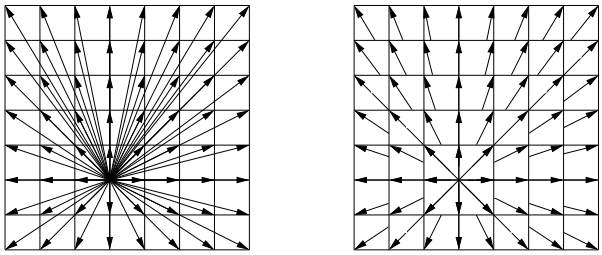

Figure 1.2.2: Comparison of the long (a) and short characteristics (b) method. Taken from Rijkhorst et al. (2006)

istics method and is computationally very expensive, since cells nearer to the source are processed multiple times.

A method addressing this redundancy is the short characteristics method. Here contributions of each cell are calculated independently and then using an interpolation scheme, rays to every cell in the grid are constructed using these preprocessed values.

Rijkhorst et al. (2006) gave a nice graphical representation of the two methods in their Figure 1, which is reproduced here in Figure 1.2.2.

Most of the codes mentioned before have one drawback. They assume Local Thermal Equilibrium (LTE), which means, that all radiative processes are seen as local processes. This gives rise to the “on-the-spot” approximation, with which a diffuse component by recombination radiation can be left out. The reasoning is as such: every photon stemming from a recombination event will find another neutral atom in the cell and ionise this atom. Thus, no recombination radiation exits the cell and is thus not needed in the solver.

There are some limitations to this approach. In a cosmological context, one deals with densities where the mean free path of a photon is magnitudes bigger than the size of the cells in the grid. The problem becomes thus non local. That this can have an influence on the final solution is demonstrated in Ritzerveld (2007). In his Figure 12.11, Ritzerveld demonstrated, that the diffuse component affects the regions of the ionisation fronts.

Some codes can include such a diffuse component using ray-tracing methods. In principle every cell can now be a source and ray-tracing needs to be carried out from each cell, to all the other cells. This is computationally extremely expensive.

A code including an intelligent version of such a strategy is for example ART which uses Λ-iteration for the diffuse part and the FTTE code. Another code capable of including recombination radiation is CRASH, the scheme used in this work.

CRASH is a Monte-Carlo ray-tracer, which means, that each source sends out rays of photons in a random direction. With this, the time steps in the simulation get very small but the number of rays to be processed is reduced.

Photons are propagated along these rays and energy is deposited in each cell. A big drawback of this method is its low angular resolution.

Some codes like ZEUS-MP or FLASH-HC are coupled to hydrodynamics. This is not that much of a technical challenge when using ray-tracing. Since a hydro time step is larger than the time scales of the radiation or the chemical solver, radiation and chemical evolution can be solved decoupled from the hydrodynamic solver. This is only possible, if a hydro time step is always bigger than the time scales of the other processes (Whalen and Norman (2006)).

OTVET - Optically Thin Variable Eddington Tensor (Gnedin and Abel (2001)) The Optically Thin Variable Eddington Tensor (OTVET) approximation was developed by Gnedin and Abel in 2001. Using the moments of the radiative transfer equation and the approximation of optical thinness they can formulate the Eddington tensor and solve for it. The Eddington tensor describes photons as if they form a sort of gas. The OTVET code has been coupled to hydrodynamical simulations.

This formulation has one big advantage that it scales linear with the number of sources. Due to this, Gnedin and Abel were the first to study the problem of reionisation (Gnedin (2000)). For many codes, this is still a big task and not easy to do.

One must note, that OTVET fails in optically thick parts. This is the case when two ionisation fronts that are about to overlap are present. In this case, the two fronts seem to attract each other and start to deviate from spherical symmetry (Iliev et al. (2006)). This is an unphysical effect and leads to deviations of about 17% from spherical symmetry.

SimpleX SimpleX (Ritzerveld (2007)) is a very interesting code. It makes no use of a structured grid, but uses an unstructured one instead. The grid is constructed in such a way, that grid points are separated by one mean free path. The points are then connected using the Delaunay tessellation technique. Thus, the grid is a direct function of matter density.

The radiative transfer equation is then solved by walking along the Delaunay lines. The fact that all points are spaced according to the mean free path makes the integration of the transfer equation especially easy. The code does not scale with the number of sources, which makes it an ideal candidate for diffuse radiation.

Unfortunately the code has its drawbacks. Since the grid is a function of the mean free path, it varies from wavelength to wavelength. To solve the polychromatic transfer case, a new grid has to be constructed for each wavelength, which probably poses a problem to efficiency.

Another problem of the code lies in the nature of the grid. Since photons only travel along the Delaunay lines that connect the grid points, and the grid is a function of matter density, photons tend to travel in the direction of the highest density. This is seen in Ritzerveld (2007) in his Figure 9.7 where SimpleX is compared to other codes of the comparison project. In the cosmological field test, all the codes have the filaments more neutral than SimpleX. It seems that

filaments do not shield radiation, instead they facilitate photon transportation. This is unphysical and a very big drawback of the scheme.

We want to end our short introduction to these different methods here. Unfortunately it would exceed the capacities of this work to explain the codes in more detail. The code used in this work will be discussed completely.

For all simulations and calculations used in this work, we adopted a WMAP 3 cosmological model with $\Omega_\Lambda = 0.7$, $\Omega_{baryon} = 0.04$, $\Omega_{DM} = 0.26$, and a Hubble constant of $h = 0.7$.

2 The Gnedin Model of the Ly-α Forest

In 1997 Hui and Gnedin produced the now widely accepted model of the Ly-α forest (Hui et al. (1997)). They showed, that the Ly-α forest is a direct product of cosmological structure formation. The hydrogen absorption lines trace cosmological structures such as filaments and voids. The statistical properties of this model match strikingly well with the observed properties of the forest (see below).

For the model to work, Hui and Gnedin derived a way to directly map dark matter densities to gas (i.e. hydrogen) densities (Hui and Gnedin (1997)). Applying a semi-analytical model to cosmological hydro-simulations they derived their so called "Equation of State" (it is in fact not a real EOS) which enables the use of dark matter only simulations. This makes things easy, but of course does not capture the complex processes involved in turbulent and shocked gas. Since these processes only play a bigger role in higher density environments, the effect on the Ly-α forest is small, for these systems show up in saturated lines only.

2.1 The Model

Ly-α ($10.196\,\mathrm{eV}$ or $1216\,\mathrm{\AA}$) or higher energetic photons are continuously redshifted as they travel through space and time. On their journey through space, they might end up meeting a hydrogen atom that absorbs the photon. It will excite the electron from the ground state to a higher state. This mechanism absorbs photons and reduces the light that reaches an observer on earth.

We can now quantify the amount of photon absorption by defining the optical depth as an integral over the line of sight where x is the comoving coordinate on the line of sight

$$\tau\left(\nu_{obs}\right) = \int_{x_A}^{x_B} n_{HI}(x)\sigma_\alpha(\nu_{rest})\frac{dx}{1+z} \tag{2.1.1}$$

The probability that a photon gets absorbed is then $e^{-\tau}$ which is also called the transmission probability. In Equation (2.1.1) x_A defines the location of the source on a line of sight. x_B accordingly describes the point of absorption/observation. n_{HI} gives the proper number density of neutral hydrogen at point x. σ_α is the cross section of the Ly-α absorption, which is a function of wavelength in the restframe of the absorbing atom at position x. z denotes the cosmological redshift.

The restframe wavelength in the system of the intervening atom is a combination of two effects. The main effect that has to be taken account for is cosmological redshifting of the photon. This can be expressed through $\nu_{obs}\,(1+z)$. A secondary effect that needs to be addressed is the fact, that the hydrogen atom will not be static in the general case. It will travel at some peculiar velocity v_{pec} in the direction of the line of sight. This motion will again red- or blueshift (Doppler-shift) the photon for the atom in question, an effect that can be described through $\nu_{obs}\,(1+z)\,(v_{pec}/c)$, where c is the speed of light. It needs to be noted, that $\frac{v_{pec}}{c} \ll 1$. The transformation to restframe wavelength is thus

$$\nu_{rest} = \nu_{obs}\,(1+z)\left(1+\frac{v_{pec}}{c}\right) \tag{2.1.2}$$

Since we will be using dark matter only simulation outputs given at a specific redshift, it is convenient to expand Equation (2.1.2) around a central redshift $\overline{z}$. Bared variables will denote quantities at redshift $\overline{z}$. First we need to define redshift z as

$$z = \frac{v}{c} = x\frac{\dot{a}}{a}\frac{1}{c} = xH\frac{1}{c} \tag{2.1.3}$$

where x has the same meaning as above and a is the expansion factor. H is the Hubble constant which is defined as $H = \dot{a}/a$. With this we can expand Equation (2.1.2) around $\overline{z}$ and get

$$\begin{aligned}
\nu_{rest} &= \nu_{obs}\,(1+\overline{z})\left(1+\frac{v_{pec}}{c}\right) + \nu_{obs}\,(z-\overline{z})\left(1+\frac{v_{pec}}{c}\right) \\
&= \nu_{obs}\,(1+\overline{z}) + \nu_{obs}\,(1+\overline{z})\,\frac{v_{pec}}{c} + \frac{1+\overline{z}}{1+\overline{z}}\nu_{obs}\left(1+\frac{v_{pec}}{c}\right)(x-\overline{x})\,\frac{\overline{H}}{c} \\
&= \nu_{obs}\,(1+\overline{z})\left(1+\frac{v_{pec}}{c} + \frac{\overline{H}}{(1+\overline{z})}\frac{1}{c}\,(x-\overline{x}) + \frac{\overline{H}}{(1+\overline{z})}\frac{v_{pec}}{c^2}\,(x-\overline{x})\right)
\end{aligned} \tag{2.1.4}$$

The term with c^2 can be omitted, since its contribution is too small. With this we get

$$\nu_{rest} = \nu_{obs}\,(1+\overline{z})\left(1+\frac{u}{c}\right) \tag{2.1.5}$$

with u being

$$u \equiv \frac{\overline{H}}{1+\overline{z}}\,(x-\overline{x}) + v_{pec}\,(x) \tag{2.1.6}$$

We will define one more velocity coordinate needed for mapping the flux to a point in the spectrum. The observed wavelength in the spectrum ν_{obs} is the wavelength of the Ly-α transition ν_α transformed into the restframe of $\overline{z}$ and from that point on redshifted by u_{obs}. This transforms the problem into velocity coordinates with zero point $\overline{z}$.

$$\nu_{obs} = \frac{\nu_\alpha}{1+\overline{z}}\left(1-\frac{u_{obs}}{c}\right) \tag{2.1.7}$$

We can now transform the coordinates of 2.1.1 into our new definitions. By noting that $dx = \frac{dx}{du}du$ Equation (2.1.1) transforms into

$$\tau\,(u_{obs}) = \int_{u_A}^{u_B} \frac{n_{HI}}{1+\overline{z}}\left|\frac{du}{dx}\right|^{-1}\sigma_\alpha du \tag{2.1.8}$$

For σ_α we need to take into account, that the cross section also depends on a thermal component (thermal broadening). This thermal broadening is expected to be Gaussian distributed and can be expressed as

$$\sigma_\alpha = \sigma_{\alpha,0} \frac{c}{b\sqrt{\pi}} e^{-(u-u_{obs})^2/b^2} \tag{2.1.9}$$

where $\sigma_{\alpha,0}$ is the cross section of the Ly-α transition $\sigma_{\alpha,0} = 4.5 \times 10^{-18}\mathrm{cm}^2$. b is the thermal broadening parameter

$$b = \sqrt{2\frac{k_B T}{m_p}} \tag{2.1.10}$$

where k_B is the Boltzmann constant, m_p is the mass of the proton and T the temperature of the gas. The form of Equation (2.1.9) only accounts for thermal broadening and does not include natural broadening of the line. To fully describe the broadening mechanisms, one needs the Voigt-profile function. The Voigt-profile is a convolution of the Gaussian thermal profile and the Lorentzian natural line profile. But in the regime of low column densities, the Lorentzian profile has little effect on the line, therefore it can be omitted. This is true for column densities less than about $10^{17}\,\mathrm{cm}^{-2}$ (see Hui et al. (1997) for further references).

Equation (2.1.10) can be extended by an expression describing turbulent motion smaller than the cell-size of the simulation. This turbulent motion we call in analogy to the same practise in stellar atmospheres “microturbulence” and a discussion is given in Chapter 2.7.

2.1.1 Proper Number Density

We now have the basic ingredients to create our synthetic Ly-α spectrum. The only problem still remaining is, how do we determine the proper number density of hydrogen and where do we get its temperature from, if we are only using dark matter simulation? We will first address the problem of number densities.

First we will define two quantities, that make life easier. The first one is the proper number density in terms of overdensity. The second one is the overdensity as such. The idea of overdensities is, that one only looks at the deviation of a cosmic mean value. The number density thus becomes

$$n_H(x) = \overline{n_H}\,(1 + \delta_{baryon}(x)) \tag{2.1.11}$$

where $\overline{n_H}$ is the cosmic mean number density at redshift $\overline{z}$ and δ_{baryon} is the overdensity of baryonic matter. This assumes, that all baryonic matter is hydrogen which might seem crude. The amount of hydrogen in the universe is very high, especially in the low density regime discussed here. About 90% of the total number density is attributed to hydrogen, the rest being mostly helium and a small fraction of metals. Therefore this is a reasonable and well working approximation for the Ly-α forest. The overdensity is thus defined as

$$\delta_{baryon}(x) = \frac{\rho_{baryon} - \overline{\rho}_{baryon}}{\overline{\rho}_{baryon}} \tag{2.1.12}$$

To calculate the number density, the rate equation needs to be solved.

$$\frac{dn_{HI}}{dt} = -n_{HI}\Gamma_{HI} + n_{HII}n_{e^-}R_{HII/e^-}(T) \tag{2.1.13}$$

Here Γ_{HI} is the HI-photoionisation rate and R_{HII/e^-} is the HII-recombination rate. Approximate values of these atomic quantities are $\Gamma_{HI} \approx 4\times10^{-12}J_{HI}\mathrm{s}^{-1}$ and $R_{HII/e^-} \approx 4.29\times10^{-13}\left[T/(10^4\mathrm{K})\right]^{-0.7}\ \mathrm{cm}^3\mathrm{s}^{-1}$ (see Hui and Gnedin (1997) for further details). J_{HI} is 70% of the flux of the ionising background radiation $J_{HI} = 0.7J_{912}/10^{-21}$ and T the gas temperature, with J_{912} being the background radiation intensity at $912\,\text{Å}$ wavelength in units of $\mathrm{ergs\ Hz^{-1}\ s^{-1}\ cm^{-2}\ sr^{-1}}$. We will assume, that the gas is in ionisation equilibrium which is shown to be reasonable later. This means $dn_{HI}/dt = 0$. Since the gas in the Ly-α forest is highly ionised and we are considering hydrogen only, we can further approximate n_{HII} and n_{e^-} by setting them equal to the total number density n_H. The fraction of neutral hydrogen is so small, that this is true (around 0.002% for $\delta = 0$ and $z = 3$ - see Chapter 2.1.5). This transforms 2.1.13 into

$$n_{HI} = \frac{1}{4\times10^{-12}\cdot J_{HI}[s^{-1}]}\cdot n_H^2\cdot 4.29\times10^{-13}\left(\frac{T}{10^4\mathrm{K}}\right)^{-0.7}[\mathrm{cm}^{-3}] \tag{2.1.14}$$

Since the universe considered here only consists of hydrogen, an expression for n_H can be easily found using the mean density for baryonic matter as mean density

$$n_H = \frac{\overline{\rho}_{baryon}\,(1+\delta_{baryon})}{m_p} \tag{2.1.15}$$

where m_p is the proton mass. The mean density is (including all unit conversions) with $h = H_0/100$

$$\begin{aligned}\overline{\rho}_{baryon} &= \frac{3}{8\pi G}H_0^2\Omega_{baryon}\,(1+z)^3 \\ &\approx 1.8\times10^{10}h^2\Omega_{baryon}\,(1+z)^3\left(3.3\times10^{-20}\right)^2[\mathrm{g\,cm^{-3}}] \\ &\approx 1.9\times10^{-29}h^2\Omega_{baryon}\,(1+z)^3\,[\mathrm{g\,cm^{-3}}]\end{aligned} \tag{2.1.16}$$

By substituting this into Equation (2.1.15) we get

$$\begin{aligned}n_H &\approx \frac{1.9\times10^{-29}h^2\Omega_{baryon}\,(1+z)^3\,(1+\delta_{baryon})\,[\mathrm{g\,cm^{-3}}]}{1.7\times10^{-24}[\mathrm{g}]} \\ &\approx 1.1\times10^{-5}h^2\Omega_{baryon}\,(1+z)^3\,(1+\delta_{baryon})\,[\mathrm{cm^{-3}}]\end{aligned} \tag{2.1.17}$$

We can now put Equation (2.1.17) into the expression for the number density of neutral hydrogen Equation (2.1.14) and obtain

$$n_{HI} = 1.3\times10^{-11}\left(h^2\Omega_{baryon}\right)^2(1+z)^6\,(1+\delta_{baryon})^2\,\frac{1}{J_{HI}}\left(\frac{T}{10^4K}\right)^{-0.7}[\mathrm{cm^{-3}}] \tag{2.1.18}$$

An expression for the temperature still needs to be found. Because we do not use a hydrodynamic simulations, dark matter densities need to be mapped to gas temperature. Fortunately there exists a relation between them, the so called “Equation of State”.

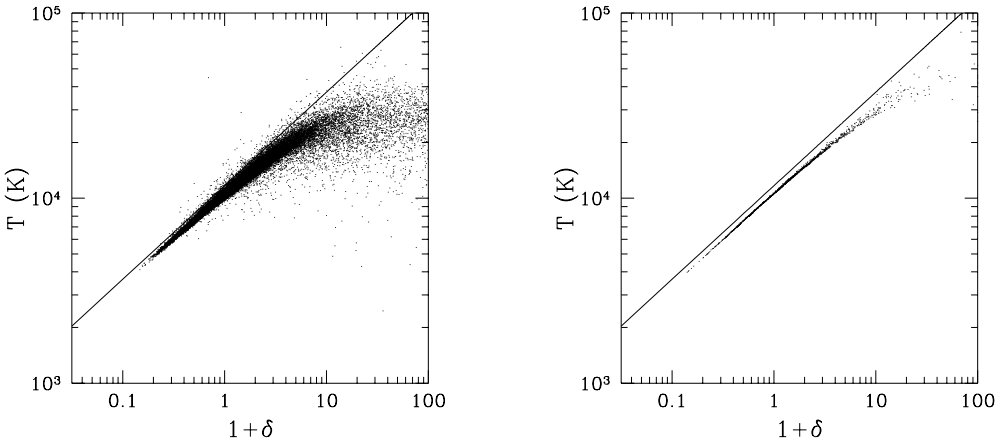

Figure 2.2.1: Comparison of the density-temperature relation in a full hydro simulation (left) with the semi-analytical model (right). The solid line represents the analytical approximation - the "Equation of state".

2.2 Mapping Dark Matter to Gas - The "Equation of State"

Hui and Gnedin found a practical relation between dark mater density and gas temperature (Hui and Gnedin (1997)). By taking a full hydrodynamical simulation and comparing this with a semi-analytical model, they were able to find a relation, they called the "Equation of state".

In principle their semi-analytical method is quite straight forward. By assuming a density evolution governed by the Zel'dovich approximation

$$1 + \delta = det^{-1} \left[\delta_{ij} + D_+(t) \psi_{ij} \right], \tag{2.2.1}$$

they were able to solve for the thermal evolution (Equation (2) in Hui and Gnedin (1997)). In Equation (2.2.1) δ_{ij} is the Kronecker delta and $D_+(t)$ is the linear growth factor. By supplementing this with a rate equations similar to Equation (2.1.13) and knowing the heating and cooling terms, temperatures can be derived. They included hydrogen and helium in their calculations.

Initial conditions were then chosen randomly from a Gaussian distribution for some fluid elements and the semi-analytical model was solved by evolving the density evolution according to Equation (2.2.1). The result is strikingly identical with the full hydro simulation. This can be seen in Figure 2.2.1, which was taken from Hui and Gnedin (1997).

The semi-analytical model does not show the turn-off at high densities. This is due to the fact, that the turn-off is governed by shocks and turbulence in the full hydro simulation. The Zel'dovich approximation corresponds to the motion of parallel sheets of matter. They evolve linearly as long as they do not cross (first-crossing). At the time of first-crossing, the approximation fails (Peacock (1999)). The density-temperature correlation is best fitted with a power law, as

can be seen in the semi-analytical model.

$$T = T_0 \left(1 + \delta\right)^{\gamma - 1} \tag{2.2.2}$$

Hui and Gnedin were able to analytically derive the power law correlation to further emphasize that the fit is physical. This is in fact the solid line plotted in Figure 2.2.1 which corresponds to a model with a sudden reionisation epoch at $1 + z = 9$. The full analytical model is given by Equation (2.2.2) and their Equations (19) and (22). T_0 and γ depend on the reionisation history of the universe and are redshift dependent. A reasonable range for both values are $1.2 < \gamma < 1.7$ and $3 \times 10^3 \mathrm{K} < T_0 < 3 \times 10^4 \mathrm{K}$. The approximation is good for overdensities $\delta \lesssim 5$ and reasonable good for $\delta \lesssim 10$. This can be seen in the right diagram of Figure 2.2.1.

Observational constraints have been derived by Schaye et al. (2000). They used high-resolution and high signal-to-noise quasar spectra to measure T_0 and γ. Using b-parameters of Ly-α absorption lines, they were able to compile Figure 2.2.2.

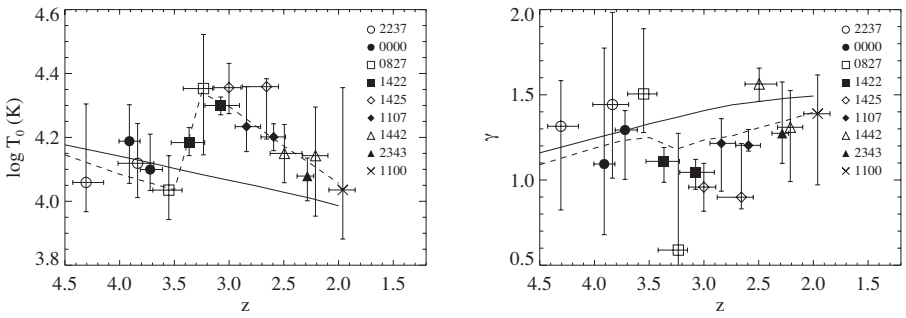

Figure 2.2.2: T_0 and γ as a function of redshift $4.45 < z < 1.88$ derived from observational data.

2.2.1 The Complete Model

We now have all the ingredients to complete the derivation of the Hui and Gnedin model. Combining Equation (2.1.18) with Equation (2.2.2) we obtain the equation that lets us map dark matter densities to hydrogen number densities.

$$n_{HI} = 3.0 \times 10^{-11} \left(\frac{2 \times 10^4 [\mathrm{K}]}{T_0}\right)^{0.7} \left(\frac{\Omega_{baryon} h^2}{0.02}\right)^2 \left(\frac{0.5}{J_{HI}}\right) \left(\frac{1+z}{4}\right)^6 \times \left(1 + \delta\right)^{2 - 0.7(\gamma - 1)} \left[\mathrm{cm}^{-3}\right] \tag{2.2.3}$$

With this, the opacities in the spectrum can be calculated. In principle the number densities enter Equation (2.1.8). The only addition is, that the opacities need to be summed up over multiple streams. It is possible, that different points in the interval $[x_A, x_B]$ refer to an identical value of u.

$$\tau\left(u_{obs}\right) = \sum \int_{u_A}^{u_B} \frac{n_{HI}}{1+z} \left|\frac{du}{dx}\right|^{-1} \sigma_\alpha du \tag{2.2.4}$$

We now assume, that du/dx is constant from one point on the line of sight to the next one, the same applies to n_{HI}. With Equation (2.1.9) and the assumptions made before we can analytically integrate Equation (2.2.4)

$$\tau\left(u_{obs}\right) = \sum \frac{n_{HI}}{1+z}\left|\frac{du}{dx}\right|^{-1}\sigma_{\alpha,0}\frac{c}{b\cdot 2}\left[\operatorname{erfs}\left(-\frac{\left(u_B-u_{obs}\right)^2}{b^2}\right)-\operatorname{erfs}\left(-\frac{\left(u_A-u_{obs}\right)^2}{b^2}\right)\right] \tag{2.2.5}$$

2.2.2 Summary of Method

1. Map dark matter particles to density and mean velocity field using Cloud In Cell weighting
2. Cut line of sight through the data cube -> δ_{baryon}, v_{pec}
3. Map peculiar velocities to velocities containing the Hubble expansion with Equation (2.1.6) -> u
4. Generate proper number densities, gas temperatures and b-parameters for the line of sight using Equations (2.2.3), (2.2.2), and (2.1.10) -> n_{HI}, T, and b
5. Generate an array for the spectrum with the desired resolution in velocity space -> u_{obs}
6. For each resolution element u_{obs} calculate τ by summation over all the cells on the line of sight using Equation (2.2.5) -> $\tau\left(u_{obs}\right)$
7. If desired, add noise to the spectrum (combination of readout noise and shot noise)

2.3 Is the Ionisation Equilibrium Applicable?

The model of Hui and Gnedin is based on the assumption that hydrogen is in ionisation equilibrium. That this is more or less the case for low redshifts can be shown by crudely solving the rate equation

$$\frac{dn_{HI}}{dt} = -\Gamma_{HI}n_{HI} + R_{HII}\left(T\right)n_e n_{HII} \tag{2.3.1}$$

To simplify the problem, the gas temperature is described by the "equation of state" $T = T_0\left(1+\delta_{baryon}\right)^{\gamma-1}$. Since hydrogen is considered only, we can set $n_e = n_{HII}$. With $n_{tot} = n_{HI} + n_{HII}$ and n_{tot} being related to the mean density as above $n_{tot} = \rho_{crit}\left(1+\delta_{baryon}\right)/m_p$. The equation describing the evolution of the plasma is then

$$\frac{dn_{HI}}{dt} = -\Gamma_{HI}n_{HI} + R_{HII}\left(T\right)\left(\frac{\overline{\rho}_{baryon}\left(1+\delta_{baryon}\right)}{m_p} - n_{HI}\right)^2 \tag{2.3.2}$$

The approximated values for the ionisation and recombination rates stated in the section above could be used. Here we have used the more accurate fits given in the Appendix of (Hui and Gnedin (1997)).

The differential Equation (2.3.2) can be analytically solved (but under the assumption, that the temperature is governed by the "Equation of state" only) and thus find with $n_H = \frac{\overline{\rho}_{baryon}(1+\delta_{baryon})}{m_p}$ and $n_\Gamma = \Gamma_{HI}/R_{HII}$

$$\frac{n_{HI}}{n_H} = 1 - \frac{n_\Gamma}{2n_H}\left(\sqrt{1+4\frac{n_H}{n_\Gamma}}\tanh\left(\frac{(t-\text{const})}{2\tau}\right) - 1\right) \tag{2.3.3}$$

with

$$\tau = \frac{1}{\Gamma\sqrt{1+4\frac{n_H}{n_\Gamma}}} \tag{2.3.4}$$

The characteristic time scale τ is for low densities identifiable with the photoionisation time scale. The characteristic time scale is dependant on the density of the medium and is smaller for higher densities. This might be counter intuitive at first, since one expects a denser medium to take longer to reach its equilibrium. In a denser medium, the number of recombinations are higher so one would expect the photoionisation rate to be reduced by some extend. Still the characteristic time is smaller. The higher recombination rate acts against photoionisation as such as that the medium cannot be completely ionised. The higher the density, the more atoms will stay neutral. Since only a fraction of the medium needs to be ionised at the rate Γ_{HI}, the equilibrium configuration is reached faster and therefore the characteristic time scale is lower.

The integration constant in Equation (2.3.3) can be obtained using $n_{HI}(t = 0)/n_H = 1$ as border condition and is

$$\text{const} = -2\tau\,\text{artanh}\left(\frac{2n_H}{n_\Gamma\sqrt{1+4\frac{n_H}{n_\Gamma}}}\right) \tag{2.3.5}$$

We can now derive the neutral fraction of the medium in the equilibrium configuration through

$$X_{HI}^{eq} = \lim_{t\to\infty}\frac{n_{HI}}{n_H} \approx \frac{n_H^2}{n_\Gamma} \tag{2.3.6}$$

How this quantity evolves with time and density is shown in Figure 2.3.1. Parameters found reasonable in reproducing the observational evidence for our simulations have been used for this task. The model-parameters are given in Section 2.5.

The higher the redshift, the more neutral hydrogen remains. This is mainly governed by the amount of UV background flux, since at higher redshift, less UV photons are present and the photoionisation rate is lower.

To calculate the time needed to reach the equilibrium, we can solve Equation (2.3.3) using (2.3.6) for t and find, that the ionisation equilibrium is reached fast and is thus well below the Hubble time. For redshift $z = 5.7$ the time to reach

the ionisation equilibrium is about 1.4×10^6 years comparing well with the age of the universe at that time $T_{5.7} = 1.46 \times 10^9$ years. Since the UV flux rises with decreasing redshift, the time to reach the equilibrium is even shorter at lower redshift. The ionisation equilibrium approximation is thus a good approximation for the model of the Ly-α forest.

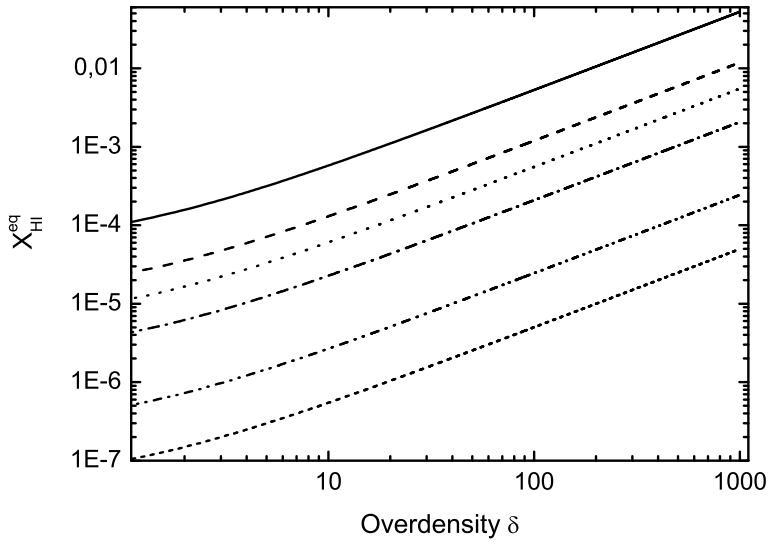

Figure 2.3.1: Redshift and density evolution of the equilibrium neutral fraction X_{HI}^{eq}. Lines give different redshifts from top to down at $z = 5.7, 4.9, 4, 3, 2, 1$

2.4 Resolution Study

An extensive resolution study has been carried out to find the best resolution for our simulations. The goal is to fully capture the properties of the Ly-α forest and simulate as big a box as possible. We therefore compared two simulations, one $100\,h^{-1}\,\mathrm{Mpc}$ box sized (256^3 particles) (Müller and Maulbetsch (2004)) resampled to a 100^3, 200^3, and 400^3 density and velocity grid. The second simulation with $50\,h^{-1}\,\mathrm{Mpc}$ boxsize and 512^3 particles was mapped to a 400^3 grid. The resolution of the grids highly influences the statistical properties of the Ly-α forest. This can be seen by eye in Figure 2.4.1. Here the same LOS with differing resolution is shown. With higher resolution, more lines are visible in the spectrum and therefore more cosmological structures play an effect. In the low resolution spectrum, some big features seem to be present, which tend to disappear with higher resolution.

Substructure in the different halos is smoothed away with lower resolution. Therefore in low resolution spectra only big and wide features are seen. To properly model the Ly-α forest, the relatively small cosmological features are needed.

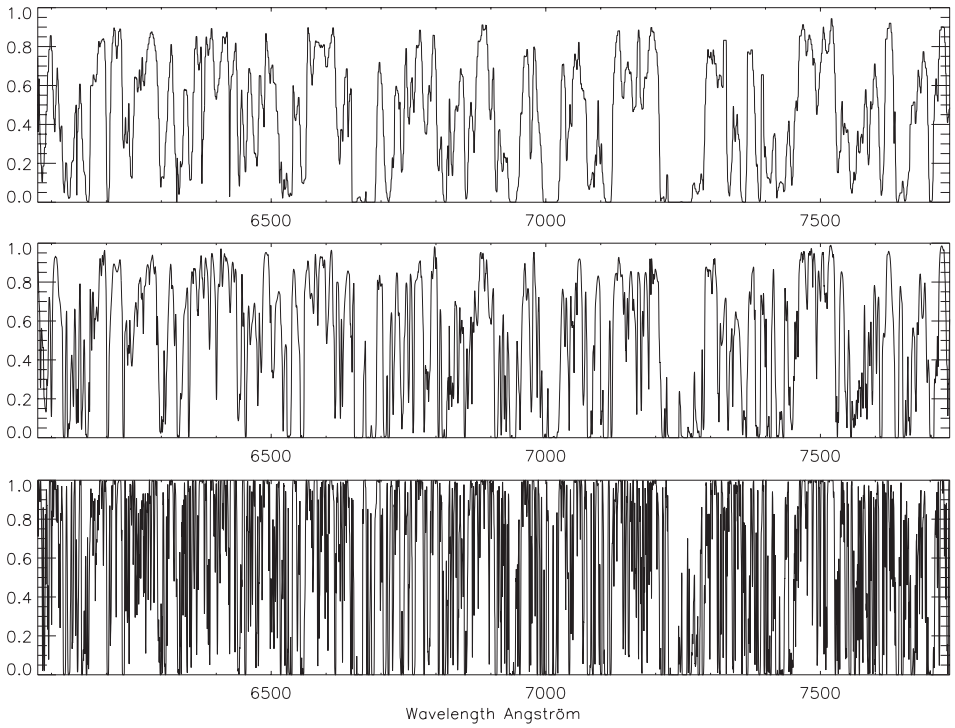

Figure 2.4.1: The effect of grid resolution on the resulting spectra for $z = 4$ using the $100\,h^{-1}\,\mathrm{Mpc}$ box size simulation. Shown here are spectra generated of the same line of sight with the following sizes of one resolution element (from top to bottom): $1\,h^{-1}\,\mathrm{Mpc}$, $0.5\,h^{-1}\,\mathrm{Mpc}$, and $0.25\,h^{-1}\,\mathrm{Mpc}$

The effect of resolution on the spectrum can be best seen in the statistical properties of the spectrum. We will first look at the probability distribution function of the normalized flux (PDF). A discussion of observational findings is given in the Section 2.5. For this comparison the PDF of McDonald et al. (2000) is used.

In Figure 2.4.2 the effect of resolution on the PDF is compared for the $100\,h^{-1}\,\mathrm{Mpc}$ simulation with the three different mappings. For this, the free parameters for each spectrum are kept the same. The lower the resolution, the higher is the deviation of the observed PDF at low opacities. In the middle range the change is quite small, especially at redshift $z = 3$. At the saturated end of the PDF the effect of resolution is high again. The lower the resolution, the lower is the peak at $F = 0.0$. The peak at $F = 1.0$ is getting higher, the higher the resolution is and seems to be diverging. It can be argued, that this is not at all in agreement with the observational data. It must be noted, that observational data is always subjected to noise which we did not include in our analysis of the PDF. Noise will be responsible for redistribution of photons at the lower and upper end of the PDF, smoothing the distribution.

Another possible effect for the rise of the peak at $F = 1.0$ is the low mass resolution of the $100\,h^{-1}\,\mathrm{MPc}$ simulation. With bigger box sizes, the mass

resolution drops. By mapping particle data to a density grid it is possible, that certain cells will contain no particle, even when using the adapted weighting scheme. These cells will appear, if the mass resolution is too low, therefore the density in these regions is too low to be resolved. Cells containing no density will be totally transparent. This could be another possible explanation for the diverging peak. Therefore a higher resolution simulation with smaller box size was chosen, to gain higher mass and spatial resolution.

In general we can say, that too low a resolution will work as smoothing on the Ly-α spectrum. Small scale features are washed out and merge to cells with high density. The density in these cells is thus over-estimated and big saturated lines are the result of this. The line number statistics of the Ly-α forest is thus directly influenced by resolution.

In further discussion of the PDF we will use noise free descriptions of the PDF by Becker et al. (2006). They fitted lognormal distribution functions to observed PDFs, convolving the distribution function with a Gaussian kernel to account for noise. With this it is possible to generate noise free PDFs from the fitted data and the effects of noise can be circumvented.

The second interesting statistical property of the Ly-α forest is the b-parameter distribution. For this, Voigt-profiles need to be fitted to the spectrum. A detailed discussion on Voigt-profile fitting (especially automatic fitting) is given in sec-

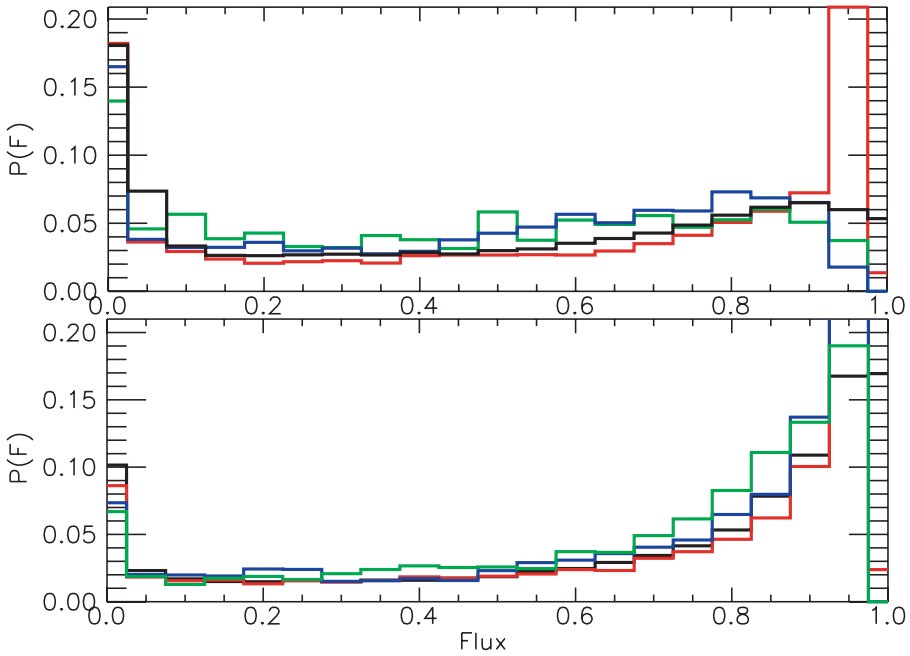

Figure 2.4.2: The effect of grid resolution on the probability distribution function of the unified flux for a $100\,h^{-1}\,\mathrm{Mpc}$ simulation at $z = 4$ (top) and $z = 3$ (bottom). The black line is the observed PDF by McDonald et al. (2000). The green line represents the PDF of the $1.0\,h^{-1}\,\mathrm{Mpc}$ mapping for one resolution element. Blue is $0.5\,h^{-1}\,\mathrm{Mpc}$ per element and red $0.25\,h^{-1}\,\mathrm{Mpc}$ per element.

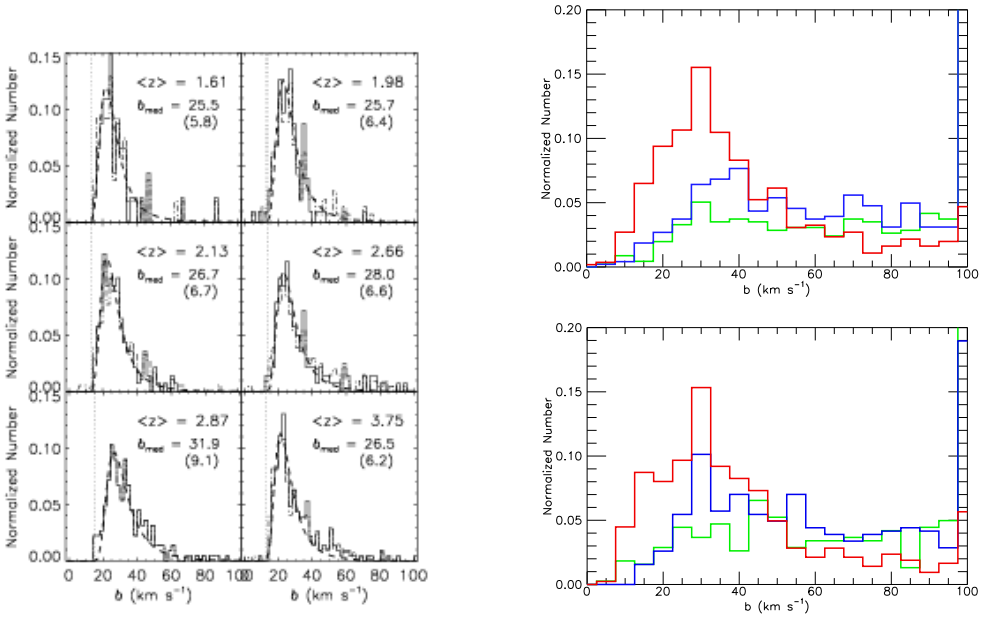

Figure 2.4.3: The effect of grid resolution on the b-parameter distribution for a $100\,h^{-1}\,\mathrm{Mpc}$ simulation at $z = 4$ (top right) and $z = 3$ (bottom right). Color coding is equal to Figure 2.4.2. For comparison Figure 10 of Kim et al. (2001) is reproduced here. The reason why the distribution differs from the observed one for large b-values lies in a problem with AUTOVP. See section 2.5.3.1 for more information.

tion 2.5.3.1.

Observational data for the b-parameter distribution was given by Kim et al. (2001) using their extensive line list containing over 600 fitted Ly-α lines derived from five quasar spectra. By comparing their Figure 10 (reproduced in Figure 2.4.3) with the b-parameter distribution of our spectra, it can be seen, that resolution has an extremely large impact on that quantity. In this analysis we used the AUTOVP automatic Voigt profile fitting code introduced in Davé et al. (1997). Our problems with AUTOVP are addressed in section 2.5.3.1 as well as a proof of concept for a different fitting approach used in this work to check the b-parameter distribution. The high probability for b-parameters over $b \geq 50\,\mathrm{km\,s^{-1}}$ is due to our problems with AUTOVP. AUTOVP was unable to correctly fit the spectrum, it inserted many broad lines with very high b-parameter. The effect of this is clearly seen in the b distribution (Figure 2.4.3).

With increasing resolution the b-parameter distribution moves into the direction of the observations, as can be seen in Figure 2.4.3. Things start to look good with a resolution of a minimum of $0.25\,h^{-1}\,\mathrm{Mpc}$ per cell.

Using the experience gained here, we decided to use a $50\,h^{-1}\,\mathrm{Mpc}$ simulation box, mapping it to a 400^3 density and velocity grid, with the resulting resolution of $0.125\,h^{-1}\,\mathrm{Mpc}$ per cell. This will be shown to reproduce the statistical properties of the forest adequately. In principle, resolutions of less than

$100\,h^{-1}\,\mathrm{kpc}$ need to be realised to fully capture all the physics in the Ly-α forest (McDonald et al. (2005)). This is hard to achieve since the large scale properties of the universe are also important for the Ly-α forest. We think, the $50\,h^{-1}\,\mathrm{Mpc}$ box size with the 400^3 mapping is a good compromise, since we almost achieve the cited resolution of $0.1\,h^{-1}\,\mathrm{Mpc}$.

2.5 Our Models

As a basis for generating our Ly-α spectra and the subsequent considerations we used a dark matter only simulation. The simulation was run using the GADGET2 code (Springel (2005)) with 512^3 particles and a particle mass of $m_p = 7.75 \times 10^7 h^{-1} M_\odot$. 3rd year WMAP cosmology has been used for the simulation (Spergel et al. (2006)) with $\sigma_8 = 0.7$ (Maulbetsch et al. (2007)).

The parameters for the Ly-α spectra synthesis giving the best results in fitting the observational data are shown in Table 2.1. The parameters for T_0 and γ are based on observations made by Schaye et al. (2000). We read the values for T_0 and γ from their Figure 6, which is reproduced here as Figure 2.2.2, and only varied them in the range of the error bars. The effects of T_0 and γ on the PDF are in fact quite small as can be seen in section 2.6. So the only remaining parameter for fitting the simulations is J_{HI}. Unfortunately it is only weakly constrained by observations and theory (Bianchi et al. (2001)).

Since no observational data was available for redshift $z = 1.0$, the parameters were gained by simply extrapolating the available data. The only quantity that we could match with high certainty for that redshift was the effective opacity.

To quantitatively see how close our models match with the observed data, we also give the values of the χ^2 goodness of fit test in Table 2.1. For comparison, the χ^2 value for a χ^2-distribution with 19 degrees of freedom (the number of bins in our PDF) and a probablilty that our models match with $P = 0.90$ is $\chi^2_{0.90} = 27.2$ (Brandt (1992)). Since the χ^2 of our models are below this value, we consider them as quite good. It can be seen, that the lower the redshift, the better the fits are.

To increase the reliability of the statistical data gained through our simulations, we randomly chose one hundred different lines of sight and synthesised

z	$T_0[K]$	$\log T_0$	γ	J_{HI}	χ^2	χ^2_{micro}
5.7	1.8×10^4	4.26	1.00	0.09	19.0	36.3
4.9	1.7×10^4	4.23	1.20	0.15	18.8	43.9
4.0	1.5×10^4	4.18	1.15	0.25	8.7	23.4
3.0	2.3×10^4	4.36	1.10	0.30	3.6	56.6
2.0	1.05×10^4	4.02	1.45	0.60	1.75	72.8
1.0	0.8×10^4	3.90	1.60	0.65		

Table 2.1: Parameters for the Ly-α synthesized spectra. χ^2 values describe PDF without microturbulence. χ^2_{micro} includes microturbulence.

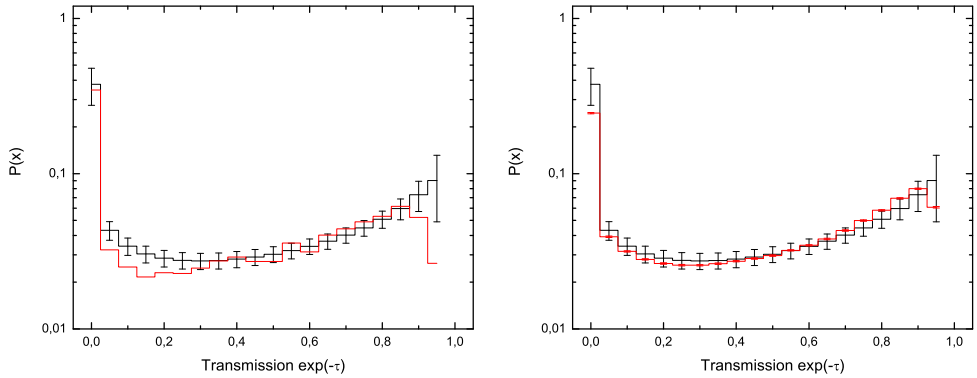

Figure 2.5.1: The PDF of a single line of sight (left) compared with the mean PDF derived from one hundred randomly chosen lines of sight (right). The black line shows observational data and the red line is the PDF derived by our simulation.

a spectra for each. The PDF of each LOS were then combined and a mean PDF was derived for comparison with observational data. This was necessary, because the PDF of one line of sight was still irregular, even though a very long line of sight of 500 Mpc length was chosen. The difference between the PDF of one line of sight and the mean PDF is shown in Figure 2.5.1 for $z = 4.0$.

2.5.1 Mean Effective Optical Depth

A simple way to characterise the overall property of the Ly-α forest spectrum is the mean effective optical depth τ_{eff}. This is defined as

$$\tau_{eff} = \langle -\ln F \rangle \tag{2.5.1}$$

Schaye et al. (2003) give observational data for the effective optical depth in their Figure 1. Our data is adjusted to their measurements as is done in Figure 2.5.2. Where there are no data points available, we assume the correlation in the dataset to continue.

In our fitting process, the mean effective optical depth was the first criteria we tried to match. By doing this, we could bring the free parameters nearer to the values that could reproduce the observed PDF. After the mean opacity corresponded to the observed values, the free parameters could be adjusted in more detail to closer match the observed mean PDFs.

2.5.2 Flux Probability Distribution Function (PDF)

A second statistical measurable property is the (normalized) flux probability distribution function. It describes the probability that a certain flux level is reached in the spectrum.

Many different observationally derived PDF exist (for example Kim et al. (2001), McDonald et al. (2000)). The problem with these data is, that they

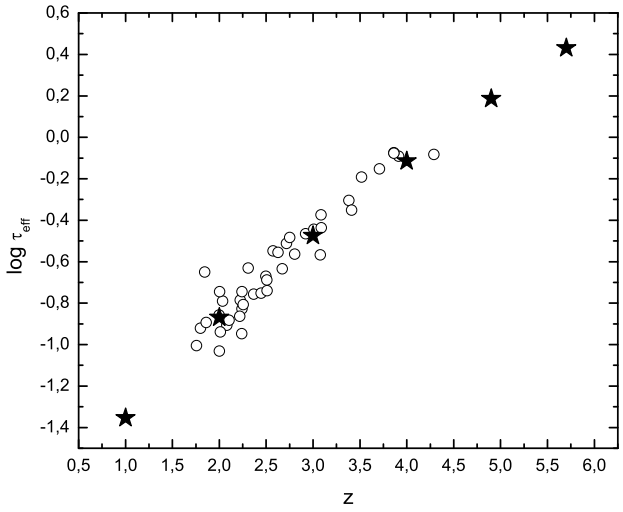

Figure 2.5.2: The effective optical depth of our models (stars) in the context of measurements by Schaye et al. (2003). Open circles represent their data points excluding the effect of metal lines in the QSO spectrum.

are based on a small number of QSO spectra. In Becker et al. (2006) the PDF of 63 HIRES QSO spectra is analysed. By looking at their data, it can be clearly seen, that the variation between different QSOs with similar redshift is very high. With this in mind, we constructed mean PDF function out of their lognormal fits to the data and compared these with ours. The advantage of this, as already mentioned, is that the effects of noise on the PDF are highly reduced, so that a direct comparison with our simulated PDFs is possible. The error bars gained from constructing the mean was the only error considered in fitting the PDF and are Poisson. Influence by observational errors and errors of the fits given by Becker et al. (2006) were not included in the analysis. In reality this would enlarge the error bars even more.

With this in mind, we tried to match the PDF as well as possible but at some points a good fit was hard to find. The main problem lies in matching the two extreme points of the PDF (i.e. the lower and the upper part). For these parts a compromise had to be found. In other parts of the PDF, the match is good in the 2 sigma region as can be seen in Figures 2.5.3 - 2.5.5.

Fitting the PDF was not an easy task, especially at high redshift the shape of our PDFs does not match the observed shape well. By looking at χ^2 values of our fits, we can say, that the models are quite good. Our fits are getting better, the lower the redshift gets. In Table 2.1 it can be seen, that the fits at high redshift are not that good as at lower redshift. This arises from the high redshift PDF being a little bit off at the lower flux part (see Figure 2.5.3). Many reasons can be responsible for this. Finding the right parameter for J_{HI} was very difficult, since it had the biggest effect on the PDF. This is shown

in section 2.6, where the effects of the different parameters are discussed. It could therefore be, that our parameters at high redshift are not well chosen or there is a problem with the model. The fit for $z = 2.0$ and $z = 3.0$ have a very low χ^2 since these fits are straight on the observational data.

Another possible explanation for our fits not matching the observed PDF at high redshift could be the low normalisation of our dark matter simulation with $\sigma_8 = 0.7$. This directly influences structure formation and would mean, that structures are not evolving as fast as they really did. Higher density regions do not form that fast and the simulated PDF would show less saturated lines. A fact that would be directly seen in the Ly-α spectra. Indication for this is seen in the PDF for $z = 5.7$ and $z = 4.9$. There the overall shape of the PDF does not match the observed one. The observed PDF show a slight 'S' form for both redshifts. Our PDFs also follow this form, but the 'S' is stronger. The overall form of the PDF cannot be greatly influenced by choosing different parameters. It can therefore be seen, that low density regions are more numerous than high density regions, emphasizing our argument.

In the PDF for $z = 5.7$ it can be seen, that our PDF matches most parts of the observed one. At the important point $F = 0.0$ the deviation of the fit to the observations is big. To match this point better, J_{HI} needs to be decreased. But then the rest of the PDF would decrease as well and would not match the observations anymore. Thus varying J_{HI} does not help. If one argues, that for high density regions the ionisation equilibrium is not yet reached, these parts would be more opaque and more saturated lines would be seen in the spectrum.

It is therefore hard to say, why we cannot match our PDFs better to the observed data for high redshift. A reasonable explanation is the low normalisation σ_8 of our simulation. Further we cannot say what effects the ionisation equilibrium could have on the PDF. The fraction between the time to reach equilibrium and the Hubble time is small, but it could be, that it is still big enough to have an effect on the PDF at high redshift. Further radiative transfer effects might be responsible for the deviations. We are going to address this question in more detail in Chapter 5, where we study possible transfer effects in detail.

To illustrate the problems of fitting the PDF, we show the PDF at $z = 4.0$ for different J_{HI} values. The problem with this PDF is, that the probability at the right end of the PDF is too low. It could be, that the observational data are biased by continuum fitting. If the continuum was placed too low, then a higher probability is reached for $F = 1.0$. But changing the continuum level only compresses the shape of the PDF to the left but does not affect the overall shape.

By increasing J_{HI}, the probability at the right end is increased. This is seen in Figure 2.5.6. But while in the right part of the PDF reaches the real distribution, the rest of the PDF starts to deviate greatly. Changing J_{HI} just a little can have a very big impact. For us a fit was considered good when as much of the PDF as possible matched.

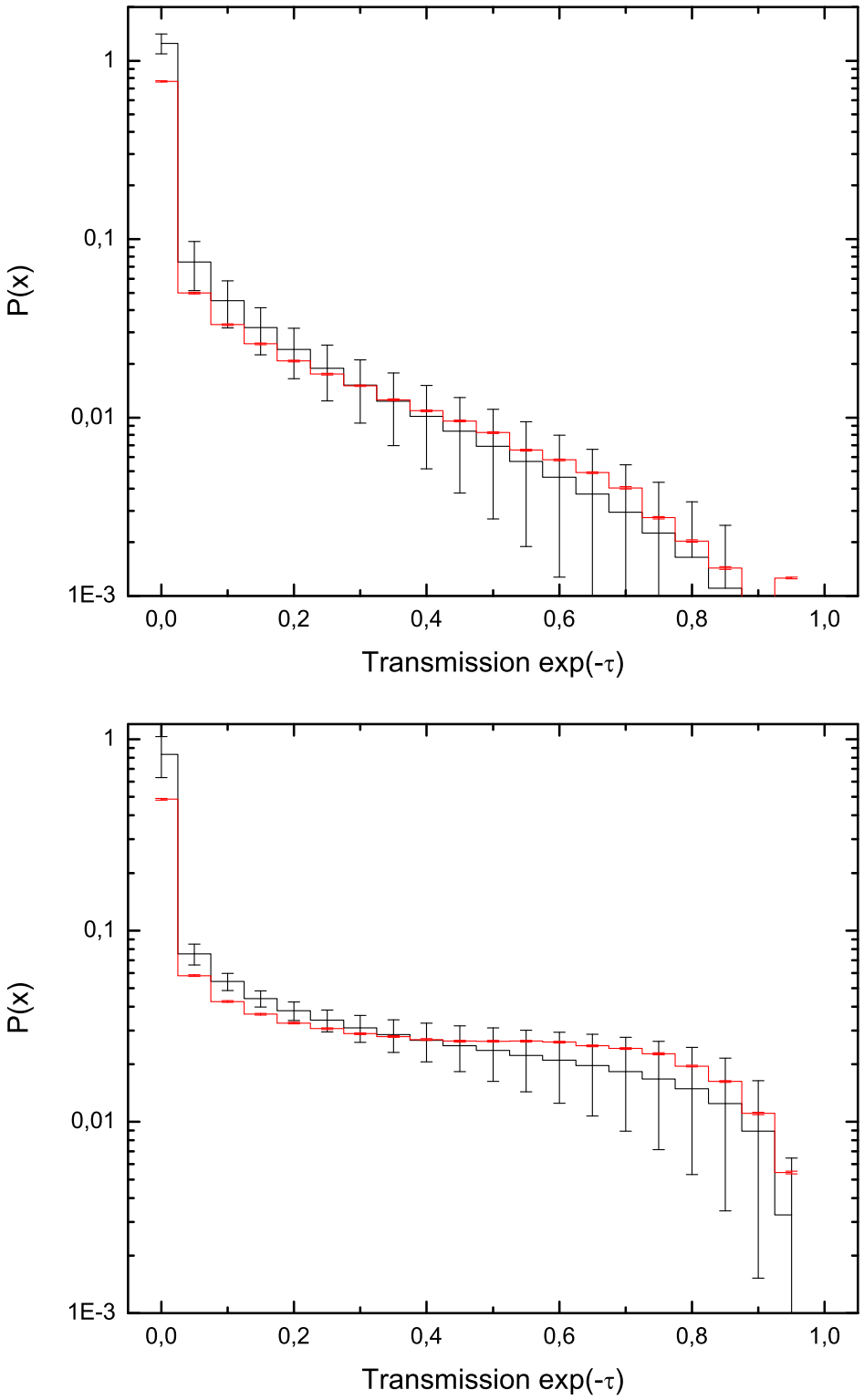

Figure 2.5.3: PDF of our simulated spectra (red) compared with mean PDFs obtained from observational data by Becker et al. (2006) (black). Redshifts are from top to bottom: 5.7, 4.9. Error bars give 1σ deviation without considering errors of the lognormal fits to the data and the data itself.

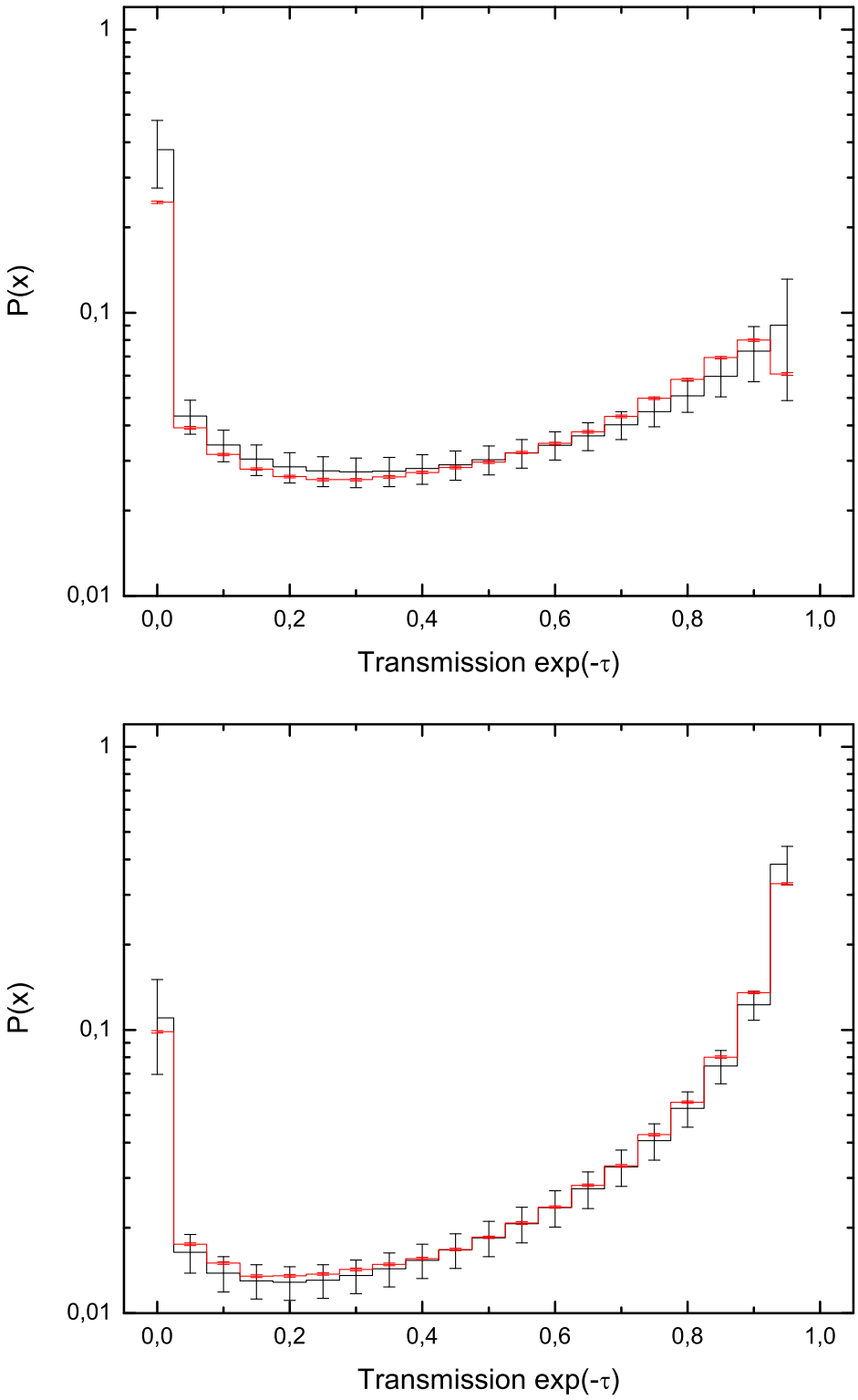

Figure 2.5.4: Continuation of Figure 2.5.3. Redshifts are from top to bottom: 4.0, 3.0. Error bars give 1σ deviation without considering errors of the lognormal fits to the data and the data itself.

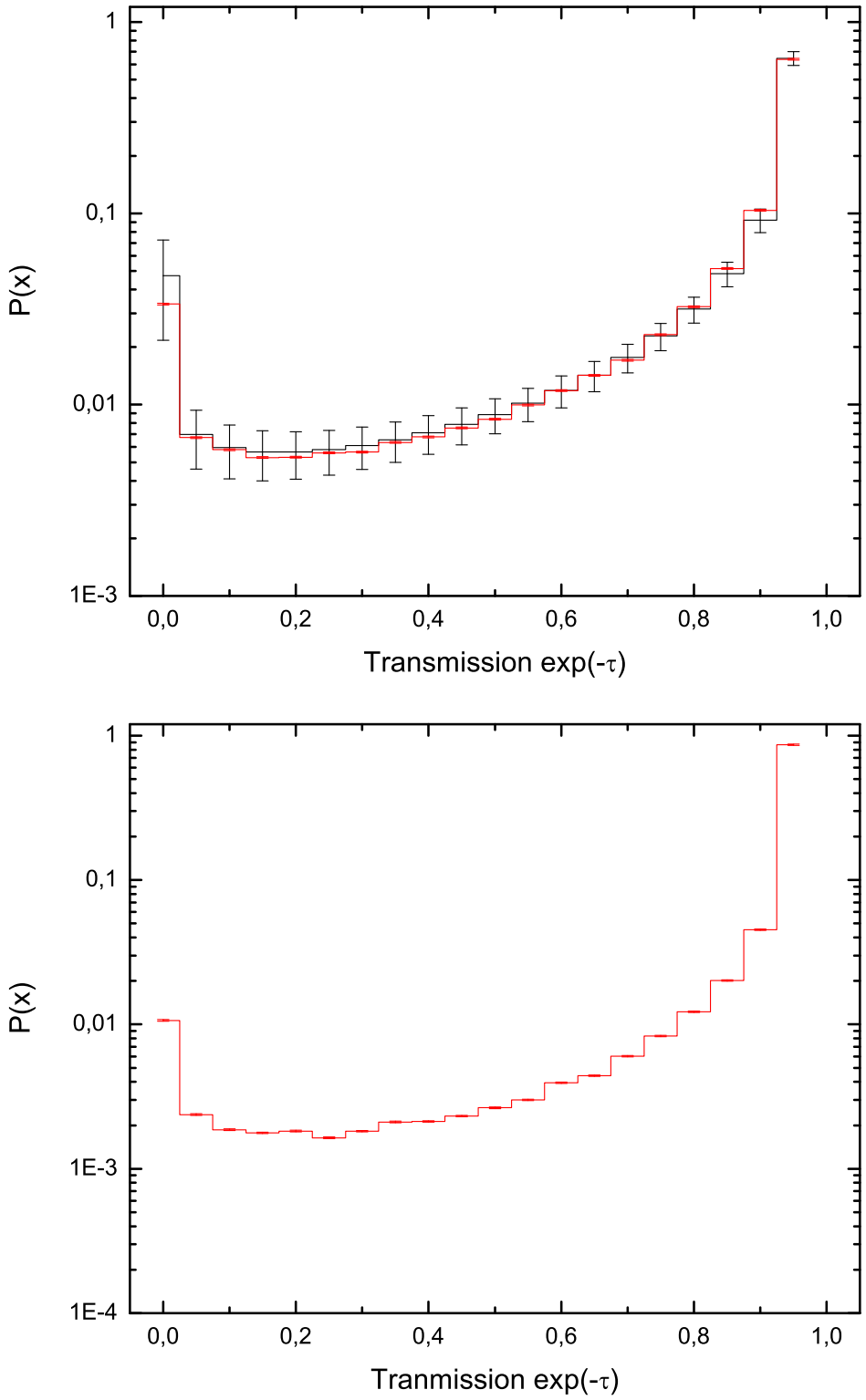

Figure 2.5.5: Continuation of Figure 2.5.3. Redshifts are from top to bottom: 2.0, 1.0. For $z = 1.0$ no observational data for comparison was available. Error bars give 1σ deviation without considering errors of the lognormal fits to the data and the data itself.

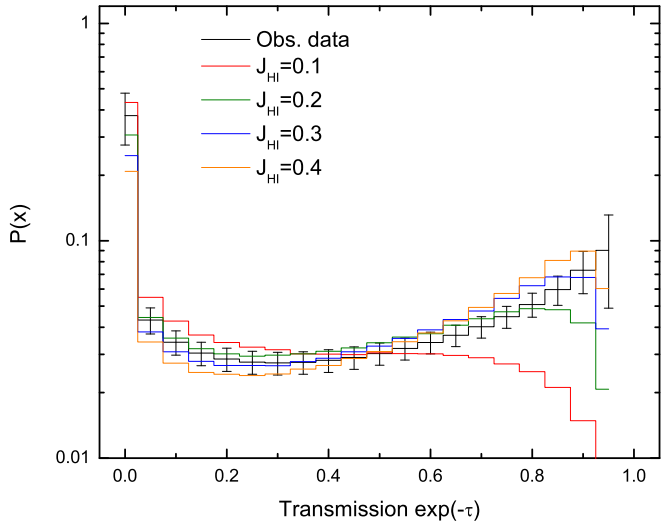

Figure 2.5.6: The PDF at $z = 4.0$ for different values of J_{HI}. The black line represents the observational data by Becker et al. (2006).

2.5.3 b-Parameter Distribution

A further statistical property is the b-parameter distribution. The b-parameter (see Equation 2.1.10) is a temperature measure of an intervening cloud (not solely, because turbulent motion can also influence the b-parameter). It affects the width of a spectral line, in contrast to the number density, which only influences the depth of the line.

To measure the b-parameter, Voigt-profiles need to be fitted to the spectrum. This is only convincingly possible, when a spectral line is not blended. Is a spectral line blended, more than one profile need to be fitted to the complex. Mathematically speaking, the problem of inverting blended Voigt-profiles has an infinite number of solutions. Many possible ways exist to fit blended lines. Since at high redshift, most of the lines are blended, these line lists are highly uncertain. No observer and no automated code will produce the same line list for the same spectra. The problem of automatic line fitting will be addressed later in connection with our problems with AUTOVP and the proposal of a new fitting algorithm.

By looking at the observationally deduced b-parameter distribution (Figure 2.4.3 left panel), it can be seen, that there is almost no evolution of the distribution with redshift (at least in the redshift range covered by the data). In a rough picture this is reproduced with our simulation (see Figure 2.5.7). For measuring the b-parameter distribution in our synthesized spectra, we used the proof-of-concept algorithm described in the next subsection. At higher redshift, especially $z = 5.7$, a broadening of the distribution can be seen. This is due to the fact, that at these high redshifts, it becomes merely impossible to fit Voigt-profiles properly to the spectrum, because the lines are heavily saturated and blended.

At lower redshift, the distribution can be reproduced surprisingly well. At $z = 3$ our code finds too many lines with $b \approx 30\,\mathrm{km\ s^{-1}}$ but the overall trend is reproduced. This vanishes at $z = 2$, where not so many blends exist anymore and we reproduce the observations nicely.

With confidence we can say, that the method described here and applied to our simulations is reproducing the observational findings. That the model proposed by Hui and Gnedin reproduces all the statistical properties of the Ly-α forest has been known since the introduction of the model. It is now time for us, to use this model as the basis for applying radiative transfer in the cosmological context and see how other effects (like the proximity effect of QSO) influence the Ly-α forest.

Because of all the uncertainty in the fitting procedure the b-parameter cannot be used to say much about fine changes in its distribution. The errors are too high. Only the rough features can be considered. This is quite unfortunate, since this quantity gives information about the temperature of the medium, which would be very interesting to study in greater detail.

2.5.3.1 Voigt-Profile Fitting

Spectral lines in the Ly-α forest can be fitted with a Voigt-profile. The profile resembles the physical mechanisms that create the line; damping of the line and thermal broadening. The optical depth in the line can be described with

$$\tau_i(\lambda) = C_i \cdot N \cdot a \cdot H[a, x(\lambda)] \tag{2.5.2}$$

where N is the column density, $H[a, x(\lambda)]$ is the Voigt-profile function and C_i and a are constants defined as

$$C_i = \frac{4\sqrt{\pi^3}e^2}{m_e c}\frac{f_i}{A_i} \tag{2.5.3}$$

Here m_e is the electron mass, A_i is the Einstein-coefficient of the ith atom transition and f_i is the matching oscillator strength. All the other constants have their usual meaning.

$$a = \frac{\lambda_i^2 A_i}{4\pi c \Delta\lambda_D} \tag{2.5.4}$$

where $\lambda_i = hc/E_i$ with E_i being the ith energy level and h the Planck constant. $\Delta\lambda_D = (b/c)\,\lambda_i$ is the term responsible for thermal broadening. The Voigt-profile function is now given by

$$H(a, x) = \frac{a}{\pi}\int_{-\infty}^{+\infty}\frac{e^{-y^2}}{(x-y)^2 + a^2}dy \tag{2.5.5}$$

with $x = (\lambda - \lambda_i)/\Delta\lambda_D$ and $y = \nu/b$ where ν is the wavelength.

These profiles need to be fitted to the QSO spectra in order to deduce the column density and the b-parameter. In real observational data, this process is a delicate and time consuming process, since QSO spectra not only include Ly-α but higher transitions of hydrogen as well. Furthermore different elements

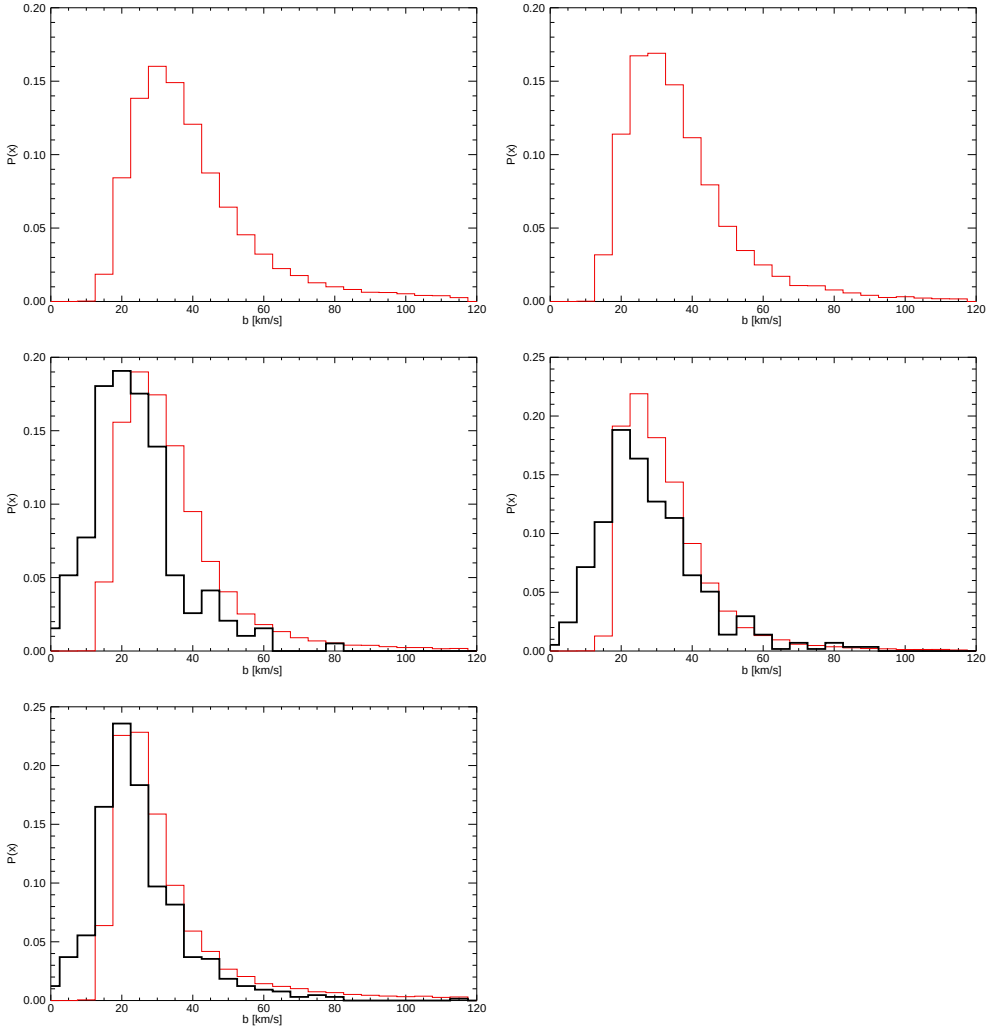

Figure 2.5.7: b-parameter distribution in our spectra (red line). Where available, observational data by Kim et al. (2001) is shown (black line). Redshifts shown from left to right and top to bottom are: 5.7, 4.9, 4.0, 3.0, and 2.0. Lines below $b \leq 20\,\mathrm{km\ s^{-1}}$ in the observational data are introduced by the fitting algorithm used when it tries to fit the noise. They should not be considered.

that blend with other lines are present. In synthesized spectra we know with which element and transition we are dealing and an automated fitting process seems appropriate.

A widely used automatic Voigt-profile fitter is AUTOVP described in Davé et al. (1997) and available at his homepage (http://ursa.as.arizona.edu/~rad/). AUTOVP works as such, that lines are fitted to the spectra by using some kind of algorithm including χ^2-minimization. Then when the initial fitting model has been found, a second χ^2 minimization is carried out, this time looking for lines that do not affect the spectrum (artifacts of the algorithm). These lines are excluded from the list and a new χ^2 is computed. Also the line parameters in the final list are slightly changed to further minimize χ^2.

Though widely used, we had some major problems with the tool, that could not be solved with tweaking the input parameters. AUTOVP gives different results, if the resolution of the spectrum is changed, even if this does not affect the overall appearance of the spectrum. It seems that AUTOVP is assuming some kind of resolution. The result even changes dramatically when the spectrum is split up into different sections. This needs to be done otherwise AUTOVP fails or is extremely slow. Splitting it up in 10 slices gives a different result, than splitting it into 20.

Motivated by this, we tried to adapt a new fitting algorithm which is in fact very fast and resolution independent (as long as lower resolution does not affect the overall appearance of the spectrum). The algorithm presented here has been used to derive the b-parameter distribution in 2.5.7. We need to emphasize, that the algorithm was only developed to a proof-of-concept state. It is not working perfectly and there are many cases where the result is not satisfactory. Adding to this, no treatment of saturated lines is included. Sometimes the algorithm fits saturated lines, sometimes it does not. The results given in saturated lines is only sometimes satisfactory. A clear treatment needs to be added. Besides this incompleteness, the result is surprisingly good.

First of all, we need to use an approximation to Equation 2.5.5 since this integral cannot be solved analytically. For this we used a newly found expression for the Voigt-profile described in García (2006). This is their Equation 25 and 24 which we reproduce here

$$H\left(a,x\right) \approx e^{-x^2}\left[1 - a\frac{2}{\sqrt{\pi}}K(x)\right] \tag{2.5.6}$$

with

$$K(x) = \frac{1}{2x^2}\left[\left(4x^2+3\right)\left(x^2+1\right)e^{-x^2} - \frac{1}{x^2}\left(2x^2+3\right)\sinh x^2\right] \tag{2.5.7}$$

The idea now is to fit the lines as follows. First, we look for minima in the spectrum. These minima represent spectral lines which we can intuitively identify. We take one of these minima and try to fix a Voigt-profile to that point, since the minimum is the center of the profile.

The minimum of the Voigt-profile we want to fit the line with, needs to be at the same place as the minimum point we have found. It should not change

when we either change the column density or the b-parameter. This means, that changing one of these two free parameters automatically implies a certain value for the other parameter, when a second point on the line is used to solve for the remaining unknown variables of the Voigt profile function.

We now take Equation (2.5.6) at the central point $x = 0$ and solve the Equation for $H(a(b), 0)$, resp. $N(b)$. This results in

$$N(b) = \frac{\tau_0 \gamma^2 \delta^2 b^2 \sqrt{\pi}}{\alpha\beta \left(\gamma\delta \cdot b \cdot \sqrt{\pi} - 2\beta\right)} \tag{2.5.8}$$

with τ_0 being the optical depth at the central point and the other constants

$$\begin{aligned} \alpha &= C_i \\ \beta &= \lambda_i^2 A_i \\ \gamma &= 4\pi c \left(1 + z\right) \\ \delta &= \frac{\lambda_i}{c} \end{aligned}$$

To solve Equation 2.5.8 for b, we need a second point of the spectral line profile and project this into the restframe description of the Voigt-profile with

$$x(b) = \frac{\lambda_x - \lambda_0}{\Delta\lambda_D} = \frac{\lambda_x - \lambda_0}{b \cdot \delta}$$

where λ_0 is the frequency of the central point and λ_x is the frequency of a point next to the central point on the spectrum. For the point x we know the optical depth τ_x. Now taking 2.5.2 for the point x on the spectrum we get

$$\tau_x = \alpha \frac{\beta}{\gamma\delta \cdot b} H\left(a, x\right) N(b) \tag{2.5.9}$$

Adding all the pieces we find an expression for $\tau_x(b)$ that can be numerically solved for b

$$\tau_x = e^{-x(b)^2} \left[1 - \frac{\beta}{\gamma\delta \cdot b} \frac{2}{\sqrt{\pi}} K\left(x(b)\right)\right] \frac{\tau_0}{1 - 2\beta\gamma\delta \frac{1}{\sqrt{\pi} \cdot b}} \tag{2.5.10}$$

The algorithm proposed now works like this:

1. Find all the minima in the spectrum
2. Pick one minimum and get the central optical depth τ_0
3. For each pixel surrounding the central point (maybe up to 10 pixels left and right), solve 2.5.10 - Do this as long as the deviation in the resulting b is not big, because if it is deviating to much, we are influenced by another line.
4. Create the mean value of all the b-parameters derived for each pixel, weighting pixels with more sTable results (usually those further away from the centrum, because the inversion of 2.5.10 is more stable there and not so much affected by uncertainties in the position of the minimum)

5. Do this for the left and the right side of the line. Choose the b-parameter that is lower for that line to be the correct one (because asymmetric lines are the result of two different lines blended together and these need to be separated)

6. When there are no minima left, subtract the current model spectra and start at point 1 again with the residual spectra.

7. Do this until you reach a threshold where you decide to stop.

It is now advisable to take the model line list and do a χ^2 minimization like AUTOVP is doing in the second phase of the analysis. We tried to put our model into the AUTOVP χ^2 minimizer but failed, because even there AUTOVP seems to be resolution dependant.

The analysis shown in 2.5.7 is done the way described here, without the χ^2 minimization proposed at the end.

2.5.3.2 Proof-of-Concept

The proposed algorithm works extremely well for a single line, reproducing almost exactly the parameter of the test line. Even for weakly blended lines, the performance is quite good. Applying the algorithm to simulated spectra sometimes gives a very good result, sometimes it seems, that some fine tuning or further ideas in the algorithm are needed. How well or bad the fit is can be seen in Figure 2.5.8.

In the upper panel a good fit is shown. At $\lambda = 5330\text{Å}$ it can be seen, that the algorithm still misses lines. Why this is still the case needs to be evaluated. On the right side of the same graph a saturated line can be seen. The algorithm was able to fit it. The minimum of this line found by the algorithm was somewhere to the right of the left foot-point of the saturated line. The algorithm could only recognise the left flank of the line, because it could not find the right side (the evaluated minimum of the line was to far to the left). Therefore it is not surprising, that the right flank does not fit. As mentioned before, saturated lines are not treated explicitly yet, this is still something that needs to be implemented.

The bad example in the lower panel shows a problem with the method. For example left to $\lambda = 4910\text{Å}$ a triplet can be found. The fit does not match the triplet at all. The reason for this lies in the simple fitting procedure. The spectrum is fitted from left to right, processing the minima in this order. This is too simple. In the case of the triplet the strongest component should be fitted first. This is the middle one in that case. This component needs to be subtracted from the triplet and then the other two can be fit. The algorithm needs to be improved for cases like these.

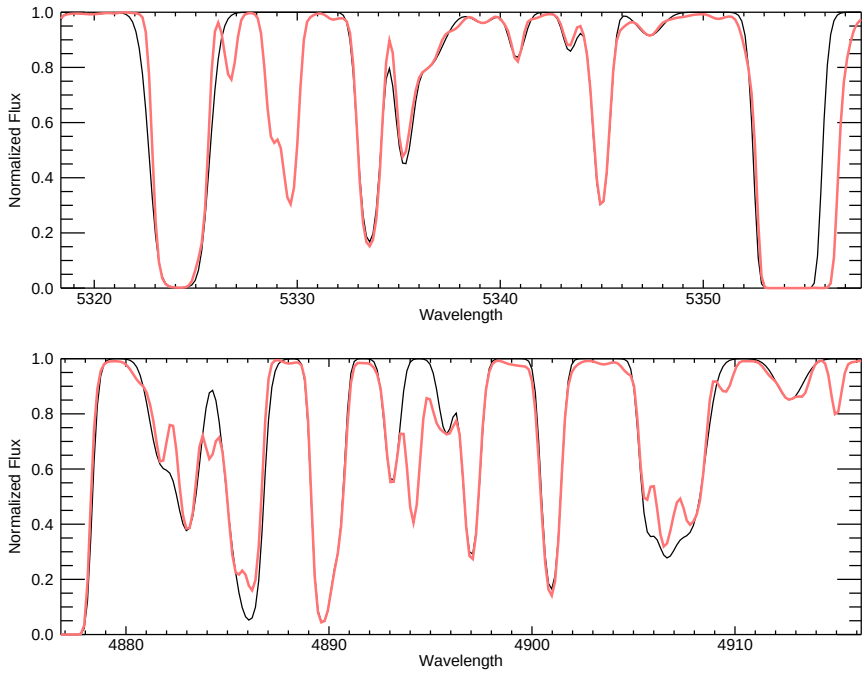

Figure 2.5.8: A good (top) and bad (bottom) example of Voigt-profile fits produced with the fitting algorithm proposed here. The red spectrum is the original synthesized spectrum. The black line represents the fit by the algorithm. Sometimes lines are missed and sometimes the fit is really off.

2.6 The Effect of T_0, γ, and J_{HI} on the PDF Shape

We now want to discuss the effect the different model parameters have on the PDF. For this we took our initial model for $z = 5.7$ and $z = 3.0$ and varied only one parameter.

The first parameter we are going to discuss is T_0. In Figure 2.1.8 the effects are shown. The influence of T_0 is quite different at the two redshifts. At $z = 5.7$ increasing the mean temperature just leads to an increase in probability at flux higher than 0.1. The curvature at the right side is influenced by higher temperatures. Opacities from the saturated part of the spectrum decrease a little bit, therefore more lower density regions in the spectrum become somewhat thinner; i.e. regions that were on the brink of becoming optically thin.

Things start to look different at $z = 3.0$. In principle the effect is the same. At high flux $F \geq 0.9$ the probability rises a little bit (between 0.2 and 0.3). Where probability is rising, it must fall at some other place, which is near the lower part of the PDF. The effect of a higher mean temperature is surprisingly small, even at $F = 1.0$. Physically this is understandable. The gas at $z = 3.0$ is already highly ionised. Thus a higher gas temperature (which increases the ionisation fraction due to reduced recombination) will have only little influence. At $z = 5.7$ the medium is still partly neutral, therefore the effect is higher.

Now we want to look at the parameter responsible for ionisation, the UV flux J_{HI}. We expect to see an increase in transparency with increasing J_{HI}. Exactly this can be seen in Figure 2.6.2 for redshift $z = 5.7$. An increase in the ionising flux increases the probability of the medium being more transparent. It is interesting, that the PDF drops at the right side for high flux levels. It seems that only a small fraction of the gas is thin enough, to be ionised. The rest of the gas is so dense, that more flux has no effect on the opacity.

The transparency increases as well for $z = 3.0$. Here there probability is being redistributed from every point in the PDF to $F = 1.0$. Since the gas is already highly ionised, an increase in the ionisation rate quickly ionises the rest of hydrogen, leaving it completely transparent.

Now for the last of the free parameters γ. This parameter mainly influences the temperature of under-dense regions. For $\gamma = 1$ the temperature is constant. Any value above this will make the temperature for $\delta < 1$ to fall and $\delta > 1$ to rise. The higher γ, the faster the temperature falls at low density and the higher is the increase of temperature at high densities. This means that with higher γ the gas should become less transparent for low densities. The opposite should happen for high densities. The effect does not manifest itself greatly in the high density regions though.

In Figure 2.6.3 the effect for the low density regions can be seen best at $z = 5.7$. There the opacity rises with higher γ, influencing the slope of the distribution at the low density end. For $z = 3.0$ the effect on high densities is clearly seen. The medium becomes more transparent for higher γ making it more probable to find flux levels higher than zero. The effect on the low density side is not that big. At $F = 1.0$ probability falls only a little bit. The combination of both effects increases the probability in the remaining region of the PDF.

The parameter influencing the PDF the most is definitely J_{HI}. We have seen that the other parameters play only a minor role compared to the flux of the ionising radiation.

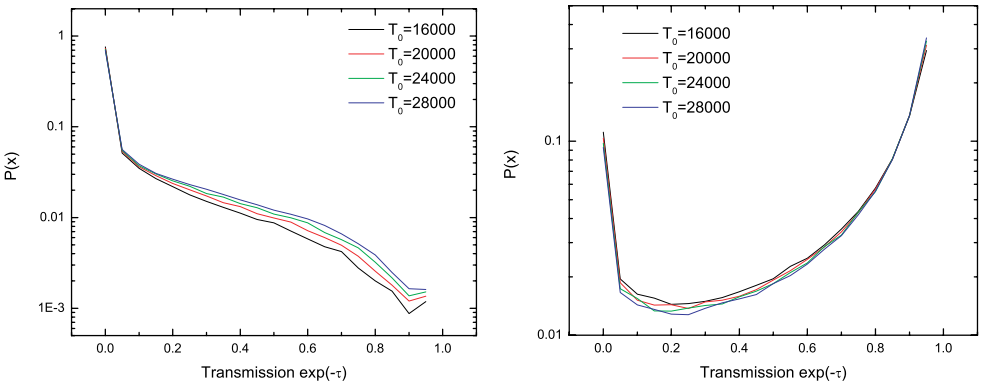

Figure 2.6.1: Influence of T_0 on the PDF at redshift $z = 5.7$ (left) and $z = 3.0$ (right)

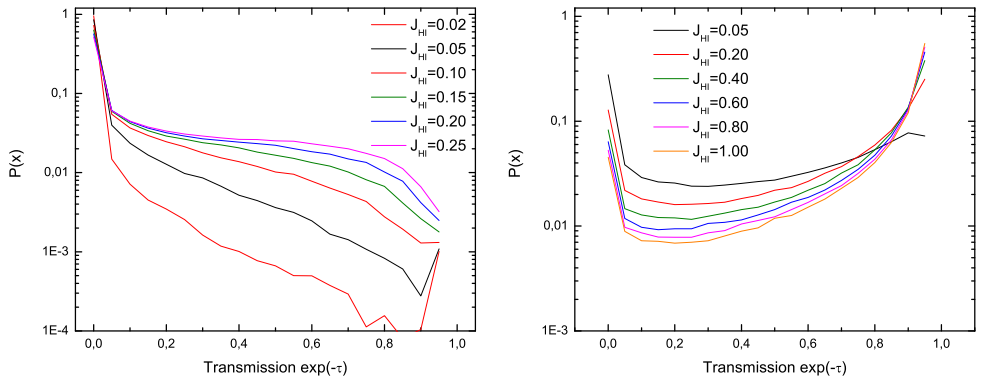

Figure 2.6.2: Influence of J_{HI} on the PDF at redshift $z = 5.7$ (left) and $z = 3.0$ (right)

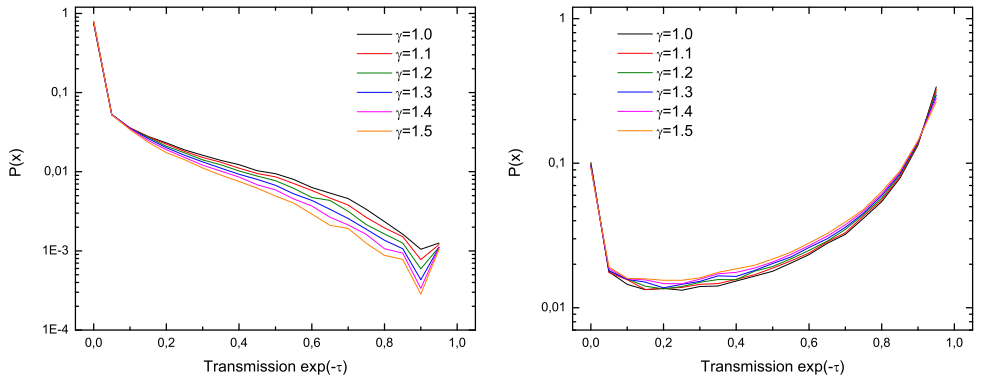

Figure 2.6.3: Influence of γ on the PDF at redshift $z = 5.7$ (left) and $z = 3.0$ (right)

2.7 Microturbulence - Velocity Dispersion

The need to simulate the Ly-α forest as highly resolved as possible and still capture as much of the universe as possible lead to the idea of combining sub resolution effects and adding them to the spectrum synthesis. In analogy to a practise known as microturbulence to the stellar astrophysicist, we tried to expand the b-parameter used in Equation (2.1.9) by a similar quantity.

$$b' = \sqrt{b^2 + \xi^2_{micro}} \tag{2.7.1}$$

The idea was to include the turbulence inside each cell (described by the velocity dispersion of the particles in each cell) to our model. It should be thus possible to capture effects, that are below the resolution of the simulation.

We mapped the velocity dispersion of the dark matter particles to a grid, weighting the dispersion according to the number of particles in the cell. Sometimes only one or two particles are present in each cell, leading to an overestimation of the microturbulence.

The velocity dispersion was then added to the b-parameter as stated in Equation (2.7.1). Since only the velocity dispersion in the direction of the line of sight is needed, the total dispersion needs to be projected onto the LOS. Since the velocity dispersion is the total dispersion of all spatial coordinates,

$$v_{total\,disp} = \sqrt{v^2_{x\,disp} + v^2_{y\,disp} + v^2_{z\,disp}} = \sqrt{3 \cdot v^2_{disp}} \tag{2.7.2}$$

we need to divide by a factor of $\sqrt{3}$ to obtain the projected velocity dispersion along the LOS.

When including this additional temperature to our spectra, we have problems reconstructing the observed PDF. The effective optical depth poses no problem since the scatter in the observational data is big and the values lie in the error bars. Microturbulence affects the probability distribution greatly. Using the same values of T_0, γ and J_{HI} derived for our simulation, the effects on the PDF is shown in Figure 2.7.3.

For some redshifts higher values of J_{HI} would be needed, to make the data fit again, for others lower J_{HI}. The redistribution in probability space is due to the additional broadening of certain lines. This can be clearly seen in the b-parameter distribution Figure 2.7.4.

While for high redshift the effect is quite small for the b-parameter, the effect in the PDF could be easily corrected through a higher J_{HI}. But for lower redshift the b-parameter gets heavily redistributed and the PDF changes its overall shape.

That the effect on the b-parameter is quite small at high redshift could have its origin in the cosmic evolution. The mean density is decreasing with lower redshift. This directly influences the mean temperature, so the same is true for T_0 after $z = 3$. A combination of both lets the velocity dispersion play a more important role with lower redshift since thermal effects become smaller, even if the mean velocity dispersion is decreasing as well. However the dispersion does not decrease as fast as the other two quantities. This means that at high redshift, line broadening would be mainly governed by the temperature. At lower redshift the effect of the temperature drops and turbulent motion can influence the spectrum more and more.

It can be argued, that we did not try to find new parameters for the PDF including microturbulence. Therefore we fitted the PDF including microturbulence to reproduce the observational data and obtained new J_{HI} values. We

z	$T_0[K]$	$\log T_0$	γ	J_{HI}	χ^2
5.7	1.8×10^4	4.26	1.00	0.13	40.7
4.9	1.7×10^4	4.23	1.20	0.20	17.4
4.0	1.5×10^4	4.18	1.15	0.40	9.6
3.0	2.3×10^4	4.36	1.10	0.80	4.6
2.0	1.05×10^4	4.02	1.45	1.1	6.4

Table 2.2: Parameters for the Ly-α synthesized spectra including microturbulence. It can be clearly seen, that the J_{HI} values needed for these fits are too high.

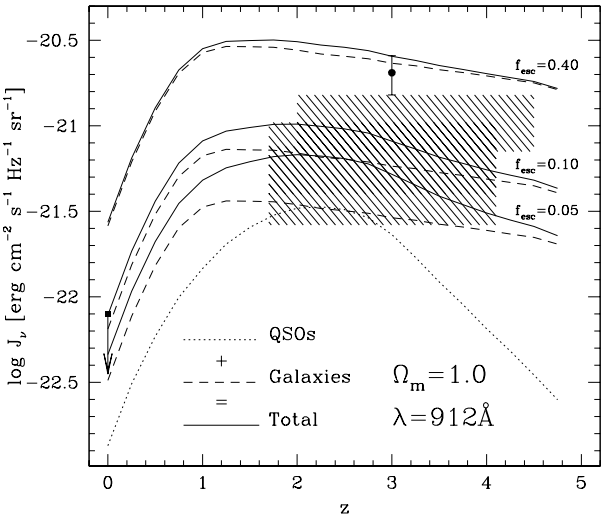

Figure 2.7.1: UV background at $\lambda = 912\text{Å}$ for different models by Bianchi et al. (2001) using different galaxy photon escape fractions. The models are derived for a $\Omega_m = 1$ universe. The separate contributions of the different components included in the models are shown.

did not change the parameters for the effective equation of state T_0 and γ, since microturbulence does not alter the state of the gas globally. To obtain maching PDFs the UV flux parameter had to be increased by a great amount.

The new values for J_{HI} are too big, if they are compared to models of the UV background flux (we used the ones given by Bianchi et al. (2001)). Bianchi et al. created models of the UV background including contribution by quasars and galaxies. The new J_{HI} would only fit, if a photon escape-fraction of $f_{esc} = 0.4$ is assumed, which is unrealistic. To compare our new values of J_{HI}, see Figure 2.7.1. One has to keep in mind that $J_{HI} = 0.7\, J_{912}$ and that the models presented by Bianchi et al. only holds for a $\Omega_m = 1.0$ universe.

The fits as a whole are quite good, χ^2 values are almost as good, as without microturbulence. A complete listing of the fit parameters including microturbulence is given in Table 2.2.

Plots of the fitting PDF using microturbulence are shown in Figure 2.7.5. The b-parameter distribution did not change, since it is not dependent on J_{HI}. We kept the other parameters constant, since there is no reason that the physical status of the gas should change by including microturbulence.

We therefore conclude, that including a microturbulence in the way we have done, is not really feasible. In our implementation of the microturbulence, the effect is too large due to the low number statistics in the velocity dispersion (see χ^2_{micro} values in Table 2.1). Statistical effects play a role, since the velocity dispersion and thus the microturbulence is determined only by a small number of particles in a cell. By plotting density against the velocity dispersion (2.7.2) it can be seen, that scatter is great at low densities (i.e. the probability is high over a big part of the dispersion axis). That the idea of a microturbulence is not at all unphysical can be seen in the visible exponential relation between

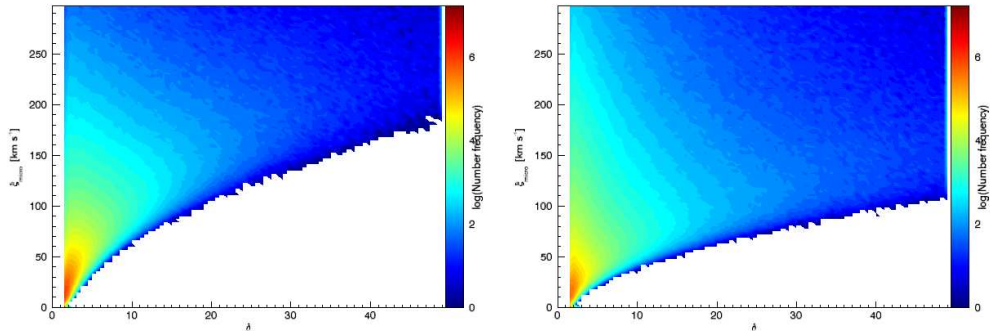

Figure 2.7.2: Relation between overdensity and the microturbulence ξ_{micro}. Left plot shows $z = 5.7$ the right plot $z = 3.0$. The colour coding describes probability distribution. Blue means low probability, red high.

density and velocity dispersion.

Further studies with hydro simulations would be needed to fully discuss the effect of a microturbulence on the Ly-α spectrum. That microturbulence has an influence can be seen in our plots of the PDF, but the quantitative effect cannot be determined. Including a microturbulence would directly affect the parameters T_0, γ and J_{HI} since other values need to be found to make the PDF fit again.

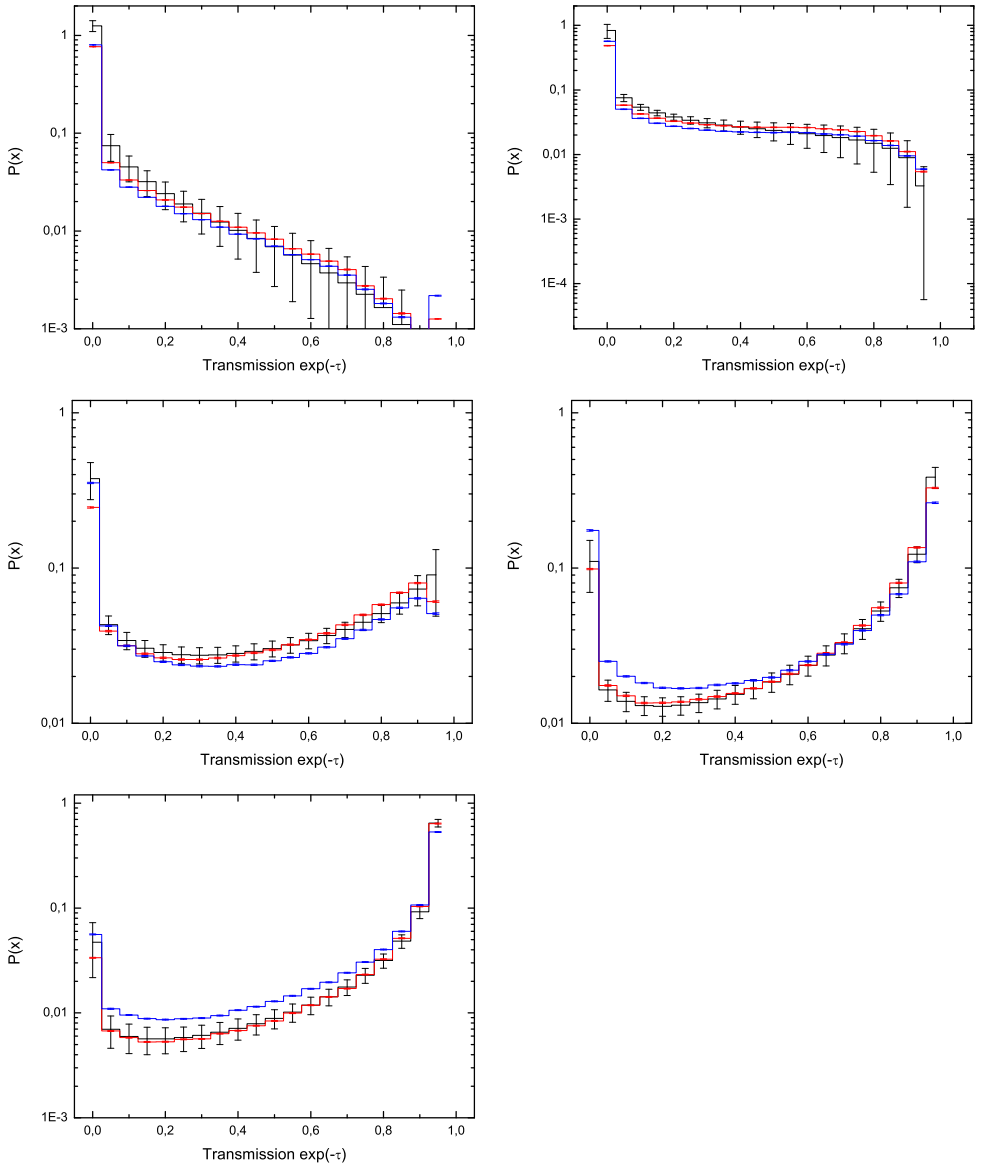

Figure 2.7.3: PDF of our simulated spectra without (red) and with (blue) microturbulence compared to mean PDF obtained from observational data by Becker et al. (2006) (black). Redshifts in the plots are from left to right and top to bottom: 5.7, 4.9, 4.0, 3.0, and 2.0.

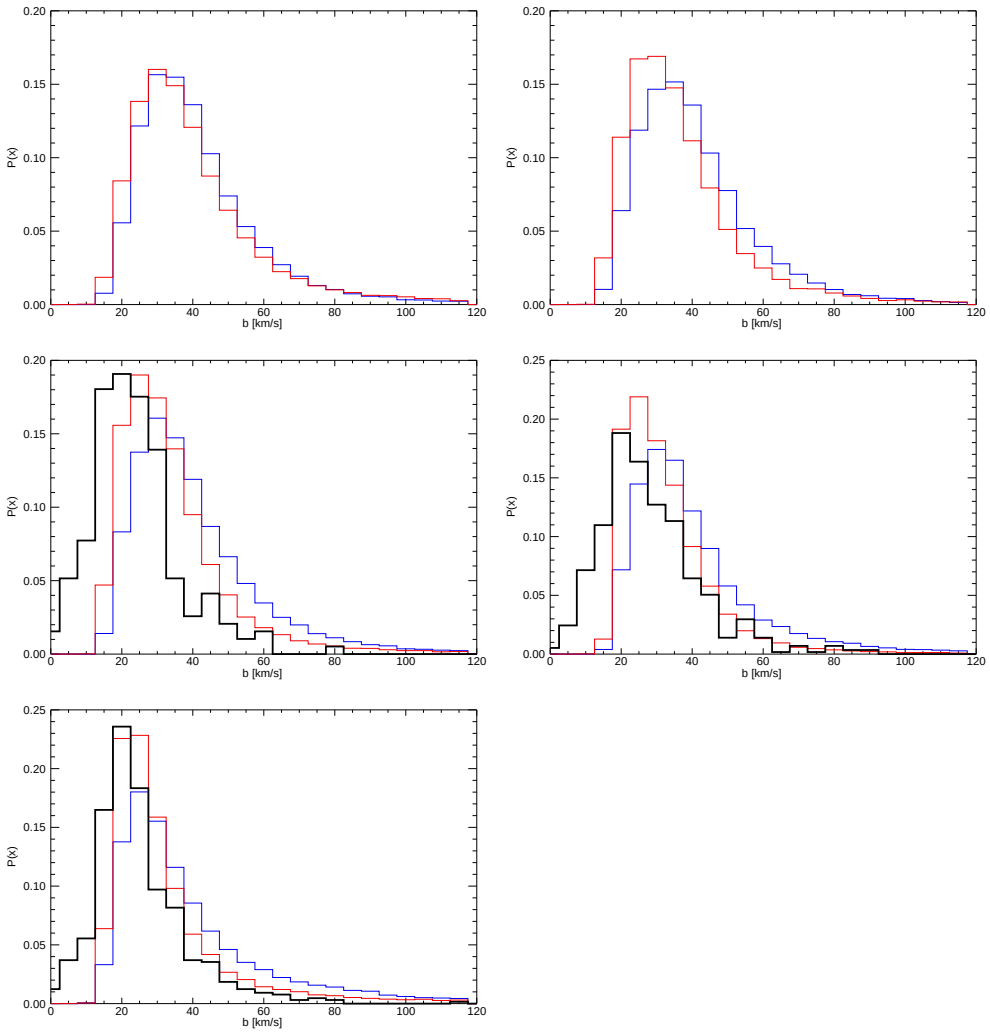

Figure 2.7.4: b-parameter distribution in our spectra. Thin red line is the model without microturbulence and the blue line represents the model including it. Where available, observational data by Kim et al. (2001) is shown (thick line). Redshifts shown from left to right and top to bottom are: 5.7, 4.9, 4.0, 3.0, and 2.0.

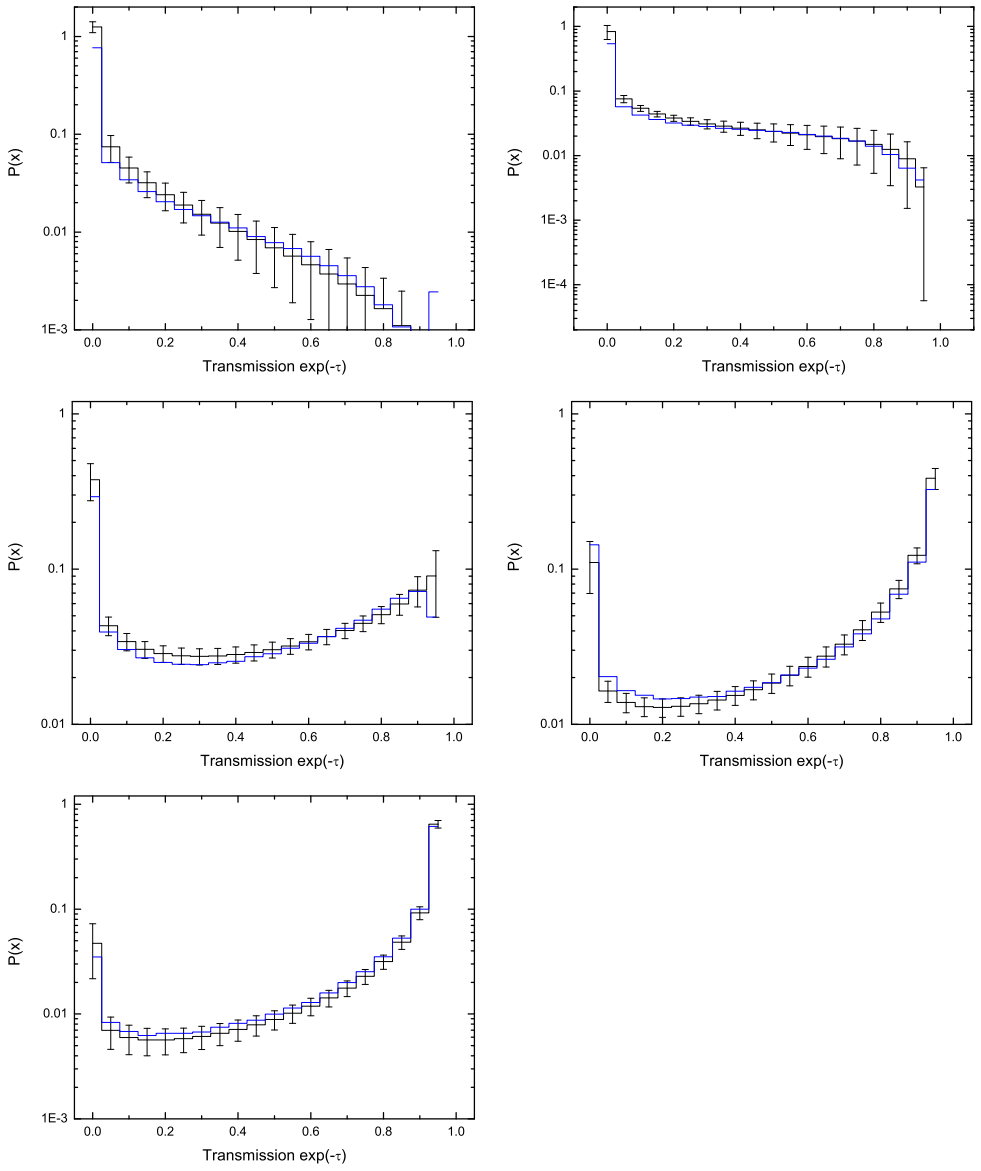

Figure 2.7.5: PDF of our simulated spectra including microturbulence (blue) now fitted to the observational data by Becker et al. (2006) (black). Redshifts in the plots are from left to right and top to bottom: 5.7, 4.9, 4.0, 3.0, and 2.0.

3 Radiative Transfer - Method

3.1 Radiative Transfer - a Short Introduction

The equation describing the macroscopic interactions of photons with matter is difficult to solve. The difficulty lies mainly in the multidimensionality of the transfer equation. Let us assume that some radiation $I_\nu\left(\vec{r},\vec{\Omega},t\right)$ in the interval $d\nu$ passes through a cell ds and cross section $d\sigma$ in time dt. The direction of the ray is given by $\vec{\Omega}$, with the light cone opening angle $d\omega$. The transfer equation is then

$$\begin{aligned}&\left[I_\nu\left(\vec{r}+\Delta r,\vec{\Omega},t+\Delta t\right)-I_\nu\left(\vec{r},\vec{\Omega},t\right)\right]d\sigma d\omega d\nu dt\\&=\left[\eta_\nu\left(\vec{r},\vec{\Omega},t\right)-\chi_\nu\left(\vec{r},\vec{\Omega},t\right)I_\nu\left(\vec{r},\vec{\Omega},t\right)\right]ds d\sigma d\omega d\nu dt\end{aligned}\tag{3.1.1}$$

with η_ν being a source term from processes like reionisation and χ_ν is a sink term for absorption. This can be written in a cosmological context in comooving coordinates as (Norman et al. (1998))

$$\frac{1}{c}\frac{\partial I_\nu}{\partial t}+\vec{\Omega}\cdot\nabla I_\nu\frac{1+z}{1+z_{em}}-\frac{H(t)}{c}\left(\nu\frac{\partial I_\nu}{\partial\nu}-3I_\nu\right)=\eta_\nu-\chi_\nu I_\nu\tag{3.1.2}$$

where $H(t)$ is the time dependant Hubble constant and z_{em} the emission redshift of the photon.

The full solution can be obtained by solving for all of the seven dimensions, namely the three components of $\vec{r}$, the two angular components ϕ and θ, the frequency ν, and the time t. The "unusual" variables in this transport equation are the angular components, and many different ways of visualising these two components in the whole problem setup can be found in the literature. In principal, these two variables are responsible, that at a given point in space, all photons coming from different angles of the local "sky" are included. At a given point, photons can arrive from different angles, therefore integration over the whole "sky" at every point is necessary.

Even with today's computers, we are far from fully solving the radiative transfer equation. Simplifications and models are needed. In stellar astrophysics different methods to approximate Equation (3.1.1) exist. The most simple approximation used is the concept of a plane parallel atmosphere. More sophisticated approaches exist and for a thorough overview see (Mihalas (1978) or Peraiah (2002)).

In extragalactic astronomy (and modern stellar astronomy), the plane parallel atmosphere cannot be used. Different simplified geometries can be applied,

like spherical symmetry for a HII-cloud or a cylindrical model for spiral galaxies. But it can be easily understood, that these models have its limitations, and that a geometry independent method needs to be developed. For example to simulate the effect of dust in a galaxy, Monte-Carlo simulations have been used, like in (Jonsson (2006)).

In cosmology, radiation transfer is an emerging field. Different groups develop different schemes for solving the equation. Mostly they rely on one approximation: all the radiation effects are treated locally (which on galactic scales is true, if the medium is dense, i.e. the optical depth is high enough). This leads to the so called "on-the-spot" approximation, excluding scattering phenomena. One of the codes applying this approximation is for example C^2-Ray by Mellema et al. (2006).

As has been pointed out by different groups, this cannot be applied in cosmological contexts (Maselli et al. (2003) and Verhamme et al. (2006)). Ritzerveld (2005) argues, that about 12% of HII regions are in fact dominated by diffuse radiation. The densities in the intergalactic medium are so low, that scattered photons can travel for many kpc, until they are scattered once again or finally absorbed. This non-locality poses a big problem for many numerical schemes. In Figure 3.1.1, the mean free path

$$r_{mean} = \frac{1}{\alpha_{H0} n_{H0}} \tag{3.1.3}$$

for different overdensities is plotted. By comparing the mean free path to the cell size in a simulation one can determine, if the "on-the-spot" approximation is valid or not. It is valid for cell sizes bigger than the appropriate mean free path of a photon.

To include scattering processes in a numerical scheme, one can choose a Monte-Carlo method. This is the easiest scheme for a diffuse component. It is also possible to have diffuse components in ray-tracing codes, but such a scheme is inefficient. A box with N_c^3 cells would need N_c^6 more rays cast per time step. Each cell is a source and needs to be traced to each cell in the box.

Ciardi et al. (2001) and Maselli et al. (2003) introduced such a Monte-Carlo scheme. Their code, called CRASH, can handle hydrogen and helium only, but different species can be included easily.

Based on their method, we implemented their scheme and added our own formulation for background photons. Further we can study light cone effects with our code. For this we propagate photons at the speed of light and problems arising with this implementation of CRASH will be discussed. Before we can go into more details of the scheme itself, we want to start with general topics, like all the atom physical effects implemented in our version of CRASH or a quick introduction to Monte-Carlo methods.

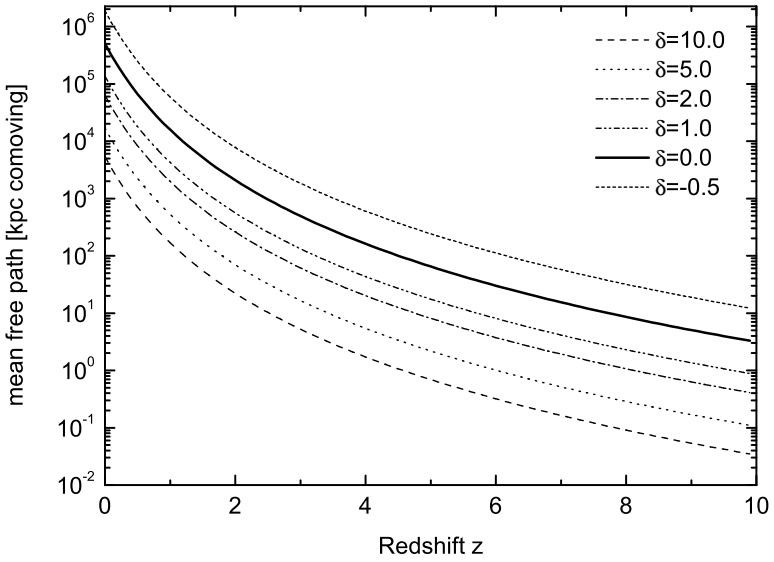

Figure 3.1.1: Mean free path of a photon in different overdensities. For this analysis only hydrogen is considered and the model of Gnedin was applied to map overdensities δ to gas density. The mean free path is given in comoving units.

3.2 Atom Physics

3.2.1 Photoionisation

Hydrogen can be photoionised if radiation with energies higher than $13.6\,\mathrm{eV}$ is absorbed by an atom. The electron will pass the ionisation threshold and the remaining energy will be transferred to the electron as kinetic energy. The reaction describing photoionisation of hydrogen can be written as

$$HI + \gamma \rightarrow HII + e^-$$

for $\gamma \geq \epsilon_{ion}$, where ϵ_{ion} is the energy needed to ionise the atom. If the energy of the photon exceeds the ionisation energy, the remaining energy is transferred to the electron as kinetic energy,

$$h\nu = \epsilon_{ion} + \frac{1}{2}mv^2 \tag{3.2.1}$$

The probability, that a photon is absorbed, is governed by the photoionisation cross-section. The cross-section for neutral hydrogen used in CRASH is originally taken from Osterbrock (2006) and is

$$\sigma_{H^0}(\nu) = 6.3 \times 10^{-18} (\nu/\nu_{th,HI})^{-3} \qquad [\mathrm{cm}^2] \tag{3.2.2}$$

where ν_{th,H^0} is the ionisation threshold frequency $\nu_{th,H^0} \approx 3.3 \times 10^{15}\,\mathrm{s}^{-1}$. The absorption caused by hydrogen is proportional to the amount of hydrogen atoms per volume. Therefore it can be expressed by means of the cross section and the number density

$$d\tau = \sigma_H(\nu)\, n_{HI}(\vec{x})\, ds \tag{3.2.3}$$

The absorption probability $P(\tau)$ is then

$$P(\tau) = 1 - e^{-\tau} \tag{3.2.4}$$

3.2.2 Recombination

When free electrons interact with ionised atoms, two things can happen. In an optically thin gas, the electron will recombine directly to a certain level n. This is called Case A recombination. In thicker nebulae the recombination will not be directly to level n. Instead the electron will first populate a higher level and from there on cascade downward, which is called Case B (Osterbrock (2006)).

For example, consider an electron recombining with an ionic hydrogen core. The final state of the electron shall be the first level $n = 1$. In Case A recombination the electron would directly go to the first level and therefore release a photon with energy $\geq 13.6\mathrm{eV}$. In Case B a certain probability exists, that the electron for example will populate level $n = 2$ first and then from there on go down to $n = 1$. Now two photons have been released, one with energy $\geq 3.4\mathrm{eV}$ and one $Ly\beta$ with $10.2\mathrm{eV}$.

Physically these two effects are included in the recombination rate α and depending on the problem the appropriate rates need to be chosen. Recombination is dependent on the kinetic energy of the electrons in the gas (i.e. the temperature), because if the kinetic energy is high, it is unlikely that the electron will be captured by the atom potential.

The total recombination rate for hydrogen where all the different recombination probabilities for each level of the atom have been considered is given by (Cen (1992))

$$\alpha_{HI}(T) = 8.40{\times}10^{-11} T^{-1/2} \left(\frac{T}{10^3\,[\mathrm{K}]}\right)^{-0.2} \left(1 + \left(\frac{T}{10^6\,[\mathrm{K}]}\right)^{0.7}\right)^{-1} \quad [\mathrm{cm}^3\mathrm{s}^{-1}] \tag{3.2.5}$$

In CRASH, only recombination events leading to photons able of re-photoionising atoms elsewhere are considered. In the case of hydrogen, these are only (direct) events to the $n = 1$ level. Therefore the recombination rate to the first level is needed and we fitted the data derived by Hummer (1994) with a function similar to Equation (3.2.5)

$$\alpha_{1,HI} = 1.5703{\times}10^{-11} T^{-1/2} \left(\frac{T}{10^3\,[\mathrm{K}]}\right)^{-0.0251} \left(1 + \left(\frac{T}{10^6\,[\mathrm{K}]}\right)^{0.9541}\right)^{-1} \quad [\mathrm{cm}^3\mathrm{s}^{-1}] \tag{3.2.6}$$

3.2.3 Diffuse Radiation by Recombining Electrons

Given the facts discussed about photoionisatoin (Section 3.2.1), it is understandable that in the recombination process any kinetic energy the electron possessed before recombining is given to the emitted photon. We therefore expect a continuous spectrum above the ionisation energy, since electrons will populate velocity space continuously.

To calculate the spectrum produced by recombination we need to solve the recombination part of the transfer equation. Since this will be an important part of the radiative transfer scheme, the complete deduction for the spectral distribution of diffuse emission will be given in detail. The notation found in Mihalas will be used, so that a direct comparison with Mihalas is possible.

We start with the radiative transfer equation

$$\mu\left(\frac{\partial I_\nu}{\partial z}\right) = -n_0 p_\nu h\nu I_\nu + n_1 n_e\left(v\right) F\left(v\right)\left(\frac{h^2\nu}{m}\right) + n_1 n_e\left(v\right) G\left(v\right) I_\nu\left(\frac{h^2\nu}{m}\right) \tag{3.2.7}$$

Here, $F(v)$ is the spontaneous recombination rate (i.e. collision of a thermal electron with an ionic atom core) and $G(v)$ is the induced recombination rate. Induced recombination occurs, when the electromagnetic field of a photon stimulates the electron to recombine with the ion. The electron can be interpreted as an oscillating dipole that is in resonance with the passing photon. Depending on the phase of the two oscillators, the electron dipole looses energy, resulting in a downward transition, which in turn emits a second photon.

Neglecting stimulated emission, the emissivity of the spontaneous recombination is

$$\eta_\nu = n_1 n_e(v) F(v) \frac{h}{m} \cdot h\nu \tag{3.2.8}$$

The probability that an atom is ionised by a photon with the wavelength ν shall be p_ν. Then, the absorption coefficient is $\alpha_\nu = h\nu p_\nu$. Equation (3.2.8) thus becomes

$$\eta_\nu = n_1 n_e(v) F(v) \frac{h}{m} \frac{\alpha_\nu}{p_\nu} \tag{3.2.9}$$

Since we are interested in the radiation caused by recombining electrons, and the velocity distribution of the electrons directly affect the emitted spectra, we enter the Maxwell distribution

$$n_e(v) = n_e\left(\frac{m}{2\pi kT}\right)^{3/2} \exp\left(-\frac{mv^2}{2kT}\right) 4\pi v^2 \tag{3.2.10}$$

in the equation above and get

$$\eta_\nu = n_e\left(\frac{m}{2\pi kT}\right)^{3/2} \exp\left(-\frac{mv^2}{2kT}\right) 4\pi v^2 \cdot n_1 F(v) \frac{h}{m} \frac{\alpha_\nu}{p_\nu} \tag{3.2.11}$$

The Saha-Equation gives the fraction of ionised atoms in a plasma in relation to the neutral component. This equation can only be applied if Local Thermal Equilibrium (LTE) is assumed.

$$\left(\frac{n_0}{n_1}\right) = n_e\left(\frac{g_0}{2g_1}\right)\left(\frac{h^2}{2\pi mkT}\right)^{3/2} \exp\left(\frac{\epsilon_{ion}}{kT}\right) \tag{3.2.12}$$

Here, g_0 and g_1 are the statistical weights of the neutral and the ionised state. The statistical weight is calculated by $g_i = 2J + 1$ where J is the total angular momentum of the species. In case of HI, $g_0 = 2$ and HII $g_1 = 1$.

By noting that the ionisation energy ϵ_{ion} is connected in the following way $h\nu = \epsilon_{ion} + \frac{1}{2}mv^2$ (see Equation 3.2.1), we can enter the Saha-Equation into (3.2.11) and get

$$\eta_\nu = n_e \left(\frac{m}{2\pi kT}\right)^{3/2} \exp\left(-\frac{mv^2}{2kT}\right) 4\pi v^2 \cdot \frac{\frac{n_0}{n_e}\left(\frac{2g_1}{g_0}\right)\left(\frac{h^2}{2\pi mkT}\right)^{-3/2}}{\exp\left(\frac{h\nu}{kT}\right)\exp\left(-\frac{1}{2}\frac{mv^2}{kT}\right)} F(v)\frac{h}{m}\frac{\alpha_\nu}{p_\nu} \tag{3.2.13}$$

A relation between the photoionisation probability p_ν and the recombination rate $F(v)$ can be found. This is the so called Einstein-Milne Relation and is derived as followed (again using the Mihalas notation):

In thermodynamical equilibrium, the number of ionisations equals the number of recombinations. The equation of ionisation equilibrium with $B_\nu = h\nu I_\nu$ being the specific intensity is

$$n_0 p_\nu B_\nu = n_1 n_e(v)\left[F(v) + G(v)B_\nu\right]\frac{h}{m} \tag{3.2.14}$$

With some minor conversions we get

$$B_\nu = \frac{n_1 n_e F(v)\frac{h}{m}}{n_0 p_\nu m - n_1 n_e(v)G(v)h} = \frac{F(v)}{G(v)} \Big/ \left(\frac{m n_0 p_\nu}{n_1 n_e(v)G(v)h} - 1\right) \tag{3.2.15}$$

which is identical to Equation (4-90) in Mihalas (1978). From the Planck law we also know, that the specific intensity in thermal equilibrium is

$$B_\nu(T) = \frac{\left(2h\nu^3/c^2\right)}{e^{h\nu/kT} - 1} \tag{3.2.16}$$

By comparing Equation (3.2.15) with (3.2.16) (i.e. equating the nominator and denominator of each equation), we find

$$F(v) = \left(\frac{2h\nu^3}{c^2}\right) G(v) \tag{3.2.17}$$

and

$$\frac{p_\nu}{G(v)} = \frac{h}{m} n_e(v)\frac{n_0}{n_1} e^{h\nu/kT} \tag{3.2.18}$$

The velocity distribution of the electrons is again governed by Equation (3.2.10). For the term n_0/n_1 we can enter the Saha-Equation. Again, keeping in mind that $h\nu = \epsilon_{ion} + \frac{1}{2}mv^2$ for recombining electrons using (3.2.12) one finds

$$\frac{p_\nu}{G(v)} = \left(\frac{h}{m}\right)\frac{n_e\left(\frac{m}{2\pi kT}\right)^{3/2}}{\exp\left(\frac{mv^2}{2kT}\right)} 4\pi v^2 \frac{1}{n_e}\left(\frac{2g_1}{g_0}\right)\left(\frac{h^2}{2\pi mkT}\right)^{-3/2}\left(\frac{\exp\left(\frac{mv^2}{2kT}\right)}{\exp\left(\frac{h\nu}{kT}\right)}\right)\exp\left(\frac{h\nu}{kT}\right) \tag{3.2.19}$$

Simplifying yields

$$p_\nu = \frac{8\pi m^2 v^2}{h^2 g_0} G(v) \tag{3.2.20}$$

By using (3.2.17) we find the Einstein-Milne Relation

$$p_\nu = \frac{4\pi c^2 m^2 v^2}{h^3 \nu^3} \frac{g_1}{g_0} F(v) \tag{3.2.21}$$

We can now enter Equation (3.2.21) in (3.2.13) and we get

$$\eta_\nu = \frac{n_e \left(\frac{m}{2\pi kT}\right)^{3/2} \exp\left(-\frac{mv^2}{2kT}\right) 4\pi v^2 \cdot \frac{\frac{n_0}{n_e}\left(\frac{2g_1}{g_0}\right)\left(\frac{h^2}{2\pi mkT}\right)^{-3/2}}{\exp\left(\frac{h\nu}{kT}\right)\exp\left(-\frac{1}{2}\frac{mv^2}{kT}\right)} F(v) h\alpha_\nu}{m\frac{4\pi c^2 m^2 v^2}{h^3\nu^3}\frac{g_1}{g_0}F(v)} \tag{3.2.22}$$

Simplifying again, gives us Equation (4-101) in Mihalas (1978) - the equation for the emissivity of recombining electrons

$$\eta_\nu = \frac{2h\nu^3}{c^2} n_0 \alpha_\nu e^{-h\nu/kT} \tag{3.2.23}$$

We need to transform n_0 in the equation above to n_1 using the Saha-Equation, since when all of the plasma is ionised, $n_0 = 0$ and there Equation (3.2.23) fails. Entering (3.2.12) gives

$$\eta_\nu = \frac{2h\nu^3}{c^2} n_e n_1 \left(\frac{g_0}{2g_1}\right)\left(\frac{h^2}{2\pi mkT}\right)^{3/2} \exp\left(\frac{h\nu}{kT}\right) \exp\left(-\frac{\frac{1}{2}mv^2}{kT}\right) \alpha_\nu \exp\left(-\frac{h\nu}{kT}\right) \tag{3.2.24}$$

The term $\frac{1}{2}mv^2$ is the kinetic energy, and is thus the difference in energy between the ionisation frequency and the frequency of the photon $E_{kin} = \frac{1}{2}mv^2 = h(\nu - \nu_0)$. With this we get the spectrum of the diffuse emission as in Ciardi et al. (2001) Equation (16)

$$\eta_\nu = \frac{2h\nu^3}{c^2}\frac{1}{2}\frac{g_0}{g_1}\left(\frac{h^2}{2\pi m_p kT_e}\right)^{3/2} \alpha_\nu e^{-h(\nu-\nu_0)/(kT_e)} n_e n_1 \tag{3.2.25}$$

which is proportional to

$$\eta_\nu \propto \nu^3 \alpha_\nu e^{-4.8\times10^{-11}\cdot\nu/T} \tag{3.2.26}$$

This formulation will be used when we include the diffuse component in our code.

3.2.4 Collisional Ionisation

The thermal motion of atoms can lead to spontaneous ionisation due to collisions. Electrons will be removed from a neutral atom due to the coulomb potential of a bypassing electron or atom. This is the mechanism to free electrons that would be hard to free using radiation only, like in ionised oxygen OVI.

Collisional ionisation requires high temperatures, otherwise the atom-atom interaction is too weak. For hydrogen, a semi-empirical approximation to the collisional ionisation probability per atom and per unit time P_{nk}^{coll} exists (Lequeux (2005))

$$P_{nk}^{coll} \simeq 7.8 \times 10^{-11} T_e^{1/2} n^3 e^{-\chi_n} n_e \qquad [\mathrm{s}^{-1}] \tag{3.2.27}$$

where n is the quantum number from where the ionisation starts, k is the continuum level and χ_n is the ionisation potential from level n in units of kT_e, i.e. $\chi_n = \epsilon_{ion}^n / kT_e$. For all other species complex calculations need to be performed to derive this quantity and precomputed tabels can be found at the National Institute of Standards and Technology homepage `http://physics.nist.gov/PhysRefData/Ionization/atom_index.html`.

In CRASH, the following collisional ionisation rate for hydrogen is used

$$\gamma_{HI}(T) = 5.85 \times 10^{-11} T^{1/2} \left[1 + \left(\frac{T}{10^5} \right)^{1/2} \right]^{-1} e^{-157809.1/T} \qquad [\mathrm{cm}^3 \mathrm{s}^{-1}] \tag{3.2.28}$$

3.2.5 Cooling Processes

As can be seen in the rates given above, all the processes discussed (except the photoionisation cross-section) are temperature dependent. In turn radiative transfer effects influence the temperature of the plasma. For example an increase of particle density due to ionised electrons (in constant volume) will adiabatically raise the temperature. Also, depending on the wavelength of the photons, newly ionised electrons possess kinetic energy, again resulting in temperature changes.

Other heating and temperature processes exist and we will shortly talk about each one that was incorporated into our version of CRASH. Effects, that are not discretely modelled in the code are combined in the so called “cooling function”. The cooling function describes, how much the temperature changes due to the combination of certain processes, as a function of temperature and chemical composition of the plasma. The change in total energy due to different processes can be summarised to (Dopita and Sutherland (2003))

$$\dot{Q}\left(n_e, T_e, Z_A\right) = \dot{Q}_{line} + \dot{Q}_{coll} - \dot{Q}_{rec} - \dot{Q}_{phot} + \dot{Q}_{Brems} \pm \dot{Q}_{Compt.} \tag{3.2.29}$$

The different processes responsible for cooling the gas are collisional excitation cooling in emission lines $\dot{Q}_{line}$, collisional ionisation cooling $\dot{Q}_{coll}$, recombination heating $\dot{Q}_{rec}$, photoionisation heating $\dot{Q}_{phot}$, cooling through Bremsstrahlung $\dot{Q}_{Brems}$, and heating or cooling through the Compton effect $\dot{Q}_{Compt.}$.

If one assumes, that only the ground state of the ions are populated (this is true for the low densities in the intergalactic medium), the total energy change is only dependent on the electron and species density. This is not the case for Bremsstrahlung cooling. The total energy change can now be written as

$$\dot{Q}\left(n_e, T_e, Z_A\right) = n_e n_A \Lambda\left(T_e, Z_A\right) \tag{3.2.30}$$

Λ is the so called cooling function, and the cooling rates given below, are part of this cooling function which is the sum of the different cooling process rates. In our simulation, the cooling function is thus dependent on T, n_e, n_{HI}, and n_{HII} only, since for simplicity we have not included helium yet.

3.2.5.1 Collisional Ionisation Cooling

When an atom is being ionised through a collision, energy of the projectile will transfer into the overcoming of the ionisation potential by the ionised electron. The projectile will loose kinetic energy and thus the temperature decreases.

We use the same cooling rates as given in the original CRASH code

$$\zeta_{HI}(T) = 1.27 \times 10^{-21} T^{1/2} \left[1 + \left(\frac{T}{10^5}\right)^{1/2}\right]^{-1} e^{-157809.1/T} \qquad [\mathrm{erg\ cm^3 s^{-1}}] \tag{3.2.31}$$

3.2.5.2 Collisional Excitation Cooling

The same mechanism as in collisional ionisation is at work with excitation cooling. The only difference is, that the transferred energy is too low to unbind the electron. It is just raised to a higher level.

The cooling rate used here is

$$\psi_{HI}(T) = 7.5 \times 10^{-19} \left[1 + \left(\frac{T}{10^5}\right)^{1/2}\right]^{-1} e^{-118348/T} \qquad [\mathrm{erg\ cm^3 s^{-1}}] \tag{3.2.32}$$

3.2.5.3 Recombination Cooling

Adiabatic cooling and heating is followed in the code, by considering the changes in number density appropriately. Adiabatic cooling due to recombining electrons is thus treated through that process. The loss of kinetic energy due to these recombining electrons is not included in the adiabatic cooling process and therefore needs to be handled separately.

Therefore the recombination cooling rate

$$\eta_{HI}(T) = 8.70 \times 10^{-27} T^{1/2} \left(\frac{T}{10^3}\right)^{-0.2} \left[1 + \left(\frac{T}{10^6}\right)^{0.7}\right]^{-1} \qquad [\mathrm{erg\ cm^3 s^{-1}}] \tag{3.2.33}$$

is implemented.

3.2.5.4 Bremsstrahlung Cooling

While electrons move in a medium, they are constantly being deflected by the atoms around them. Their kinetic energy is reduced by deceleration in free-free two-body encounters. Every time the electron is being deflected, some

kinetic energy is transformed into radiation, called Bremsstrahlung or free-free emission.

The total energy loss by Bremsstrahlung can be expressed as

$$\beta\left(T\right) = 1.42 \times 10^{-27} T^{1/2} \left(n_{HII} + n_{HeII} + 4n_{HeIII}\right) n_e \qquad [\mathrm{erg\ cm^{-3}s^{-1}}] \tag{3.2.34}$$

Note, that this is the total energy loss and not a cooling rate.

3.3 Introduction to the Monte-Carlo Method

Monte-Carlo methods can be used, to solve many different kinds of problems. One possible application has been introduced in Chapter 2. By simulating processes that are also random in the real world, this method is the most natural way to deal with such systems. Such systems are often described through partial differential equations.

The propagation of light can be interpreted as such a stochastic process. Rays of light are sent out by a source in random direction. These rays propagate until they are absorbed. Absorption is also a probabilistic process, with a probability of $1 - e^{-\tau}$ (Equation 3.2.4). Electrons recombining with atoms are also stochastic, best described with recombination probabilities, from which recombination rates can be derived. When light is being emitted by a recombining electron, the direction of the photon is also random. Since so many aspects of the processes involved in radiative transfer are stochastic, it is easy to see that simulating all these processes using stochastic algorithms is feasible.

In general, differential equations of any type can be solved using Monte-Carlo algorithms. Sometimes these methods are the only way to handle complex equations. The problem in solving differential equations lie in the integration procedure. Using a Monte-Carlo scheme, these integrals can be sampled and an estimate of its values can be determined efficiently. The quality of the estimate is directly coupled to the number of samples evaluated.

Statistics gives a way, to write integrals as a function of the mean,

$$\int_a^b f(x)dx = (b-a)\overline{f}. \tag{3.3.1}$$

If we find a simple way to approximate the mean $\overline{f}$, the integral is solved. This can be done using a Monte-Carlo method. The function $f(x)$ is evaluated n-times using random numbers ξ_n for x with $\xi_n \in [a, b]$. Then, the mean of all these samples is calculated. The result $\frac{1}{n}\sum_n f(\xi_n)$ is an approximation of the real mean value $\overline{f}$.

To illustrate the idea behind the method, let us look at an example found in many introductory texts to Monte-Carlo techniques (like Sobol' (1994) or Dupree and Fraley (2002)).

It is possible to calculate the value of π using a Monte-Carlo technique. This might not be the easiest way to do this but serves as a good example. The area of a circle is $A = r^2\pi$. We assume $r = 1$, therefore $\pi = A$. We are going

to pick two uniformly distributed random numbers in the interval $0 < x < 1$ and $0 < y < 1$. We then check, if the chosen point lies in the circle or not. We repeat this process n-times and count all the points lying inside of the circle.

This way, we determine the area of the first quadrant, which is just the fraction of the points lying in the circle, compared to the total number of points $A/4 = N_{circle}/N_{total}$. The ratio is an approximation of the value $\pi/4$. This method is called the rejection-method.

The approximation obtained using this method will increase in precision, if the sample number is increased. We can understand this by looking at the estimate of the second central moment which is a measure of the error (also known as the variance):

$$\sigma^2 = \frac{1}{n} \sum_n (x_n - \langle x \rangle)^2 \tag{3.3.2}$$

The square-root of the second central moment is called the standard deviation σ, measuring the mean deviation of the total sample points relative to the mean value. The variance can be reduced in a simple fashion by increasing the number of samples taken. This will move the mean value nearer to the real mean value because more sample points will lie nearer to the mean, reducing the variance.

This sketches the general idea behind Monte-Carlo schemes and the CRASH code briefly. We will look at some aspects in more details, especially at ways to reduce the variance in a Monte-Carlo calculation and whether or not they could be implemented in the CRASH scheme.

3.3.1 Random Numbers / Pseudo Random Numbers

The key to good Monte-Carlo simulations lies in how random numbers are realised. Two kinds of random numbers exist: real and pseudo random numbers.

Real random numbers cannot be generated using a determinative algorithm. One has to take natural processes, like radioactive decay of atoms, noise in any analogue to digital converter, or atmospheric noise and convert these to a random number. Generating real random numbers can be complicated and require additional apparatus, which is only justifiable for special applications. On the internet, services exists, where real random numbers are obtainable using atmospheric noise, but for solving the radiative transfer equation, billions of numbers are needed at high speed. Using real random numbers is not useful in that case. Further real random numbers are not reproducible, because they gives a new set of numbers for each run of the simulation. This makes verification of a code very hard, since errors cannot be reproduced and tracked down.

Algorithms exist, that can mimic the behaviour and statistical properties of real random numbers, but unfortunately only to a certain degree and with a certain periodicity. These so called pseudo random number generators produce big series of numbers, that start to repeat themselves after a certain period. One has to be careful, that this does not happen in a Monte-Carlo simulation, since this will turn the simulation useless.

To illustrate, how these pseudo random numbers can be found, we will sketch one of the first algorithms used for this purpose, the mid-square method developed by John von Neumann.

One takes for example a four digit number $\xi_0 = 0.1234$, and takes the square $\xi_0^2 = 0.01522756$. From this new number represented by 8 digits after the decimal point, we take the four digits in the middle $\xi_1 = 0.5227$ and do the same thing again $\xi_1^2 = 0.27321529$ and so on. It can be shown, that this algorithm does not produce a good uniform distribution. Further, since this method is recursive and dependant on the preceding value, it is clear that at one point the random number will coincide with one already drawn and the series will be periodic from that point on. For example $\xi_0 = 0.1000$ will only produce 1 different number ($\xi_0^2 = 0.01000000$ with $\xi_1 = 0.0000$)! So, more sophisticated algorithms are needed and exist.

In our version of CRASH, we used the fast MT19937 Mersenne Twister pseudo random number generator, developed by Matsumoto and Nishimura (1998). It has been developed, with Monte-Carlo simulations in mind. The MT19937 has very desirable properties. It has passed all the statistical tests to date. A very desirable property of this generator, besides being very fast, is its extreme periodicity of $2^{19937} - 1$, making it ideal for Monte-Carlo simulations.

Just as a side note: When profiling our code, the random number generator uses so little time, that it does not even show up and uses at least less than 1% of the simulation time. Therefore we do not pre-tabulate any randomly derived quantity.

Since the random number generator produces uniformly distributed number between 0 and 1, a method to alter the distribution needs to be implemented.

3.3.2 Modelling Probability Distributions

It is very important for processes that are simulated with Monte-Carlo methods to be calculated with the correct set of random numbers. The sampled process needs to represent the process in the real world. This can be done, by realising the probability distribution of the random numbers to correspond to the right laws. This is called sampling and is needed for a “fair-play” in a simulation.

The easiest way to ensure a “fair-play” is to directly mimic the probability distribution of the real process. There are situations, where this could be a problem. Let us consider some spectral distribution, where the probability of a photon to have a frequency around the ionisation barrier is high, and the probability of the higher energy photons is low. By directly using this probability distribution, the frequency around the ionisation barrier is sampled more often, than the higher energies. Lets pretend, that the higher energy photons have a bigger impact than all the lower ones. In this case, we will always get many photons that have no effect, and only a few that really matter to the problem discussed. To sample these important high energy photons sufficiently, one would need to choose from an extremely large sample (this is the case in CRASH at the moment).

There is a solution to this problem. One could sample the unimportant low energy photons with a lower frequency, than the high energy photons, while

maintaining a “fair-game” using different weighting methods discussed in the next chapter. This process is called stratification or biasing and can greatly reduce the variance of a Monte-Carlo simulation.

We have seen, that it is important, to sample probability distributions correctly, since not all processes have uniform probability. Before discussing how this is achieved, we need to define two important quantities.

The probability distribution function PDF has already been introduced. Recapitulating, the PDF $f(x)$ gives the probability at every point x that an event occurs. The PDF $f(x)$ is by definition non-negative $f(x) \geq 0$. With this, the cumulative distribution function $F(x)$ can be defined as

$$F(x) = \int_{-\infty}^{x} f(t)dt \tag{3.3.3}$$

By definition the total integral over the cumulative distribution function is unity

$$\int_{-\infty}^{\infty} f(t)dt \equiv 1 \tag{3.3.4}$$

The cumulative distribution function is a function in the interval $[0, 1]$ and can now be used to map a uniform distribution to any kind of PDF. A uniformly distributed number is chosen, which corresponds to the value of the cumulative distribution function

$$\xi = F(x) = \int_{-\infty}^{x} f(t)dt \tag{3.3.5}$$

This can now be used to model any kind of PDF.

3.3.2.1 Sampling from the Inverse of the Cumulative Distribution Function

With the randomly chosen value of the cumulative distribution function, the corresponding number x can be found using the inverse of Equation (3.3.5).

$$x = F^{-1}(\xi) \tag{3.3.6}$$

If this can be solved (which is seldom the case), then a way to transform a uniform distribution has been found. If Equation (3.3.6) has no analytical solution or a solution to the problem can only be determined numerically, then another method needs to be used. But first we will demonstrate this method by modeling random numbers, that are uniformly distributed on a sphere.

In spherical coordinates on the unit sphere, a infinitesimally small surface element is

$$dS = \sin\varphi \, d\varphi d\psi \tag{3.3.7}$$

The probability, that a point P belongs to the surface element dS is $dS/(4\pi)$. So the probability density is

$$p(\varphi, \psi) \, d\varphi d\psi = dS/(4\phi) \tag{3.3.8}$$

With (3.3.7) this becomes

$$p(\varphi, \psi) = \frac{\sin \varphi}{4\pi}$$

The probability density along each of the two coordinates can be found by integrating over one of the angles

$$\begin{aligned} p_\psi(\varphi) &= \int_0^{2\pi} p(\varphi, \psi)\, d\psi = \frac{1}{2} \sin \varphi \\ p_\varphi(\psi) &= \int_0^{\pi} p(\varphi, \psi)\, d\varphi = \frac{1}{2\pi} \end{aligned} \tag{3.3.9}$$

We were thus able to decouple the components and it can be seen, that $p(\varphi, \psi) = p_\psi p_\varphi$ holds. Now the inverse (3.3.6) can be found for each component

$$\xi = F(\varphi) = \int_0^{\varphi} p_\psi(t)\, dt = \frac{1}{2}(1 - \cos \varphi)$$

By solving for φ we get

$$\varphi = \arccos(1 - 2\xi) \tag{3.3.10}$$

The inverse cumulative distribution function for the other coordinate is found analogously

$$\psi = 2\pi\xi \tag{3.3.11}$$

3.3.2.2 Rejection Technique

When Equation (3.3.6) has no analytical solution or a solution can only be determined numerically, then a technique called the rejection technique needs to be used. The principles of this method were already shortly discussed in the example where we introduced the Monte-Carlo technique for caclulating π. Since the cumulative distribution function is the area of the probability function $f(x)$ from $-\infty$ to x, the area under $f(x)$ can be sampled uniformly.

By randomly selecting a point in the rectangle spanned by $a \leq x \leq b$ and $0 \leq f(x) \leq M$, where M is the maximum value of $f(x)$ in the interval $[a, b]$, the desired PDF can be modelled. Two uniform random numbers ξ_1 and ξ_2 are drawn and then scaled to the size of the rectangle using

$$y = M\xi_1$$

and

$$x = a + (b - a)\,\xi_2$$

Now we determine whether the point (x, y) lies underneath the function graph or not. If it is not under the graph, the point is rejected and a new one is chosen. Else, the value of x is a random number drawn from the corresponding PDF $f(x)$.

This method is very useful, if the number of rejected points is small. If the area underneath the function $f(x)$ is small, compared to the chosen sampling rectangle, then this method will be very slow.

Some faster methods exist, using intelligent transformation of the PDF into a form that can be sampled better. One of the first of such transformations is discussed in Kinderman and Monahan (1977). This method can be used to accelerate sampling in the generation of blackbody or diffuse photons. At the moment, other portions of the code require more computer time, so this method has not yet been implemented and is just given for reference.

3.3.3 Variance and Variance Reduction

The mean or expected value of $f(x)$ is in the case of a continuous distribution defined as

$$\bar{f} = \frac{1}{b-a}\int_a^b f(x)dx \tag{3.3.12}$$

or for a discrete distribution

$$\langle f \rangle = \frac{1}{n}\sum_n f(x_i) \tag{3.3.13}$$

Another formulation of the mean will be important in later considerations. The expected value of a continuous distributed random variable V with the PDF $f(x)$ is the weighted average of the variable over its PDF

$$\overline{V} = \int_{-\infty}^{\infty} V(x)f(x)dx \tag{3.3.14}$$

The mean deviation of all discrete points from the mean value, i.e. the variance, is then

$$\sigma^2 = \frac{1}{n}\sum_n \left(f(x_i) - \langle f(x)\rangle\right)^2 \tag{3.3.15}$$

which can be used as an error estimate. This quantity is very important in Monte-Carlo simulations, since we want to determine the expected value of a process. For this to be accurate, we would like the variance to be as low as possible.

Therefore ways of reducing the variance, while still enabling a “fair game”, is very important, since it can increase accuracy, or decrease calculation time for a given accuracy.

3.3.3.1 Stratified Sampling

The method of stratified sampling has been mentioned quickly in the introduction. The idea is, to undersample regions of the PDF with higher probability than regions with lower probability. Each region or stratum is then sampled separately. This could be used in CRASH to undersample photons near the ionisation edge as compared with higher energy photons.

For each stratum a specific density function $f_1, f_2, \ldots$ is chosen, so that $V_i(x)f_i(x)$ is identical to the problem being evaluated. In the example given in Dupree and Fraley (2002), stratification increased the accuracy by more

than a magnitude. Stratification always reduces the variance if the number of samples in each stratum is proportional to the stratum size. The proof is given in the book mentioned above.

3.3.3.2 Biased Sampling

By looking at Equation (3.3.14), it can be easily seen, that choosing $V(x)$ and $f(x)$ intelligently, the "trivial" uniform integrand can be reproduced. These alternative formulations of the PDF and random variable not only solve the problem, but reduce the variance as well.

Let us suppose the expected value of V, $\overline{V}$, is given by

$$\overline{V} = \int_R V(x) f(x) dx \tag{3.3.16}$$

It is possible to find a different PDF $g(x)$ with $g(x) > 0$, so that

$$\overline{V} = \int_R \frac{V(x) f(x)}{g(x)} g(x) dx \tag{3.3.17}$$

The new random variable assigned to the new PDF $g(x)$ is thus

$$V' = \frac{V(x) f(x)}{g(x)} \tag{3.3.18}$$

with $\overline{V} = \overline{V'}$. The variance of V' can differ from V and by selecting $g(x)$ cleverly, the variance can be reduced. This method is called biasing. In the example given in Dupree and Fraley (2002), biasing increased the accuracy by a factor of 10. Combining biasing and stratification is also possible.

Work discussing these methods in the context of radiative transfer are (Juvela (2005)) and (Jonsson (2006)). The later work resulted in a polychromatic Monte-Carlo scheme. On how these methods can be included in CRASH will be part of further investigation. At the moment we restrict ourselves to the original CRASH scheme. Investigations whether and how the discussed techniques can be implemented in CRASH will be work to come.

3.4 The CRASH Radiative Transfer Scheme

The general idea behind CRASH is simple. Given a source and an initial density field, photon packages are sent out at random by each source. Since it is impossible to follow every photon produced by the source, they are combined into bigger entities called photon packages. Each package contains the number of photons produced by the source during a time step.

These photon packages are sent out by the source in random directions. The angular distribution can be easily controlled and modified. Distributions like homogeneous ones or beams of light are possible. The total number of packages produced by the source determines the angular sampling resolution.

Due to the limited number of photon packages, this quantity is relatively low and a high number of packages need to be realised.

Each photon package represents a monochromatic beam of light. The frequency of the package needs to be determined using the appropriate spectrum of the source. Again, this is done probabilisticly by sampling the spectrum randomly. Algorithms on polychromatic package propagation exist but have only been used in galactic settings (see Jonsson (2006)). Plans to include this technique in our code exist but are out of the scope of this master thesis.

Each photon package is then propagated at the speed of light through the simulation box. The amount of absorption is calculated each time a package crosses a cell and is subtracted from the propagating package. Are the number of photons in the package below a certain limit, then the package is viewed as absorbed and is not followed any further.

The CRASH code is also able to include a diffuse radiation field produced by recombining photons. When a cell is crossed by a package, all the electrons recombining in the cell will be counted and saved. If a certain level of recombinations has been reached, a photon package is being released from the cell in a random direction and the number of recombined electrons in this cell is set to zero.

This gives a short overview of the CRASH scheme. Details will be discussed below, where we will also show how we implemented each step. When referring to our implementation of CRASH, we will use our working name ACRASH (Adrian CRASH) from now on. ACRASH solves all the physics in comoving coordinates. All the atomic data must be transformed with the scale factor $a(z) = 1/(1+z)$.

3.4.1 Package Creation

The main idea behind Monte-Carlo radiative transfer schemes are photon packages. It is very important to note, that these photon packages do not resemble real photons. They resemble a collection of many photons to one package, i.e. a photon packages combines the energy of many photons into one photon energy package.

Our version of CRASH can handle three different kinds of packages. “Normal” photon packages produced by a source, like a star or a galaxy, background field packages and photons produced by a diffuse component, like photons stemming from recombining electrons.

3.4.1.1 Normal Package

ACRASH can produce standard photon packages in three different ways. The easiest realisation of a photon package is produced by a monochromatic source. Additionally ACRASH is able to handle black body sources and sources with any given spectral form.

Since photon packages resemble energy packages, the energy of a package is one of the main parameters. Given a time step $t_i = i \cdot \Delta t$ and a bolometric

luminosity $L_s(t)$ the energy in a package is

$$\Delta E_i = \int_{t_{i-1}}^{t_i} L_s(t)dt \tag{3.4.1}$$

The way a time step is chosen in CRASH is given by the total simulated time t_s and the number of photon packages used N_p. The time step is thus

$$\Delta t = t_s/N_p \tag{3.4.2}$$

In ACRASH we have created the possibility to loosen the time step criteria to

$$\Delta t_{ACRASH} = N_t \cdot \Delta t \tag{3.4.3}$$

where N_t describes the number of photons produced in each time step per source. We therefore do not limit the package production to one package per time step per source which has considerable benefits to the performance of our code, especially in the OpenMP parallel version. The total energy produced by the source in one timestep Δt_{ACRASH} is then distributed equally to the N_t photon packages.

The next important quantity of a package is its frequency ν. The frequency is determined by sampling the source spectrum S_ν. In the case of a black body spectrum, or an unspecific spectrum given by an input file, we sample the spectrum using the rejection method. The spectra are sampled above the ionisation threshold $13.6\,\mathrm{eV}$ only. For a monochromatic source, we do not need to sample any spectrum and just assign the monochromatic frequency to the package.

Using the frequency ν we can now determine the number of photons in the package. We do not use the energy as a parameter. Instead the number of photons in a package is used. The number of photons in the package is now

$$N_{\gamma,i} = \frac{\Delta E_i}{h\nu} \tag{3.4.4}$$

where h is the Plank constant.

In ACRASH we do not use the total number of photons in a package as a variable, since the numbers are too big. We will see, that it makes sense, to use

$$\tilde{N}_{\gamma,i} = \frac{N_{\gamma,i}}{(\Delta x)^3} \tag{3.4.5}$$

where Δx is the size of one cell. This transforms the package energy content into the units of energy density.

The origin of the photon package is given by the source location. The direction in which the package is being propagated is determined by choosing the two angles φ and ψ using the scheme described in Chapter 3.3.2.1.

A photon package is determined by the following 8 variables: the origin $\vec{P}$, the direction $\vec{D}$, the frequency ν and the number of photons in the package $N_{\gamma,i}$.

3.4.1.2 Background Field Package

A background radiation field can be implemented similarly to a normal source. However it is not that straightforward as one might think in the beginning. Two different implementations have been proposed in the literature. One is to let photon packages be created at the faces of the simulation box and then let them propagate into the box.

Another more sophisticated approach was proposed by Maselli and Ferrara (2005). They proposed to randomly choose a cell in the box where a background radiation photon is produced isotropically. This is coupled to a density threshold, since it is not initially certain that cells with high densities are exposed to the background radiation. The energy of the background field could be too weak to penetrate into these high density regions and they could be shielded. When implementing the background field in ACRASH we used the first method in the begining but had change for a compromise between the two. The reason for this is to ensure homogeneous sampling of the box.

It is not trivial to assign the energy content to a background photon package. Simply transforming the background flux J_{912} into energy is too naive, since this only resembles the amount of energy deposited in a cell. In reality the photon package has more energy and only J_{912} is deposited in a cell. To be able to propagate background packages in the CRASH way, Maselli and Ferrara (2005) proposed the following:

Starting from the ionisation equilibrium in its discrete form

$$\Delta n_{HII} = \Gamma_{HI} n_{HI} \Delta t \tag{3.4.6}$$

where Γ_{HI} is the ionisation rate, we can say that the amount of absorbed photons in a cell correspond to

$$\Delta n_{HII} = \frac{N_\gamma \left(1 - e^{-\Delta\tau}\right)}{\Delta x^3} \tag{3.4.7}$$

This transforms Equation (3.4.6) into

$$\Gamma_{HI} n_{HI} \Delta t \Delta x^3 = N_\gamma \left(1 - e^{-\Delta\tau}\right) \tag{3.4.8}$$

For the optical thin case $\Delta\tau \ll 1$ we can write $\left(1 - e^{-\Delta\tau}\right) \approx \Delta\tau$. In Equation (3.2.3) we have seen that $\Delta\tau = \sigma_{HI} n_{HI} \Delta x$, where σ_{HI} is the photoionisation cross-section of hydrogen. With this we can find an expression for the total photon content of the package

$$N_\gamma = \frac{\Gamma_{HI} \Delta t \Delta x^2}{\sigma_{HI}} \tag{3.4.9}$$

or in the case of the comoving coordinates in ACRASH

$$N_\gamma = \frac{\Gamma_{HI} \Delta t \Delta x^2 \cdot a(z)^2}{\sigma_{HI}} \tag{3.4.10}$$

This is the photon package content arriving at one cell. Firstly we have chosen to let background packages emerge from the sides, we need to multiply Equation (3.4.9) with N_{cells}^2 to get the amount of photons passing through one side

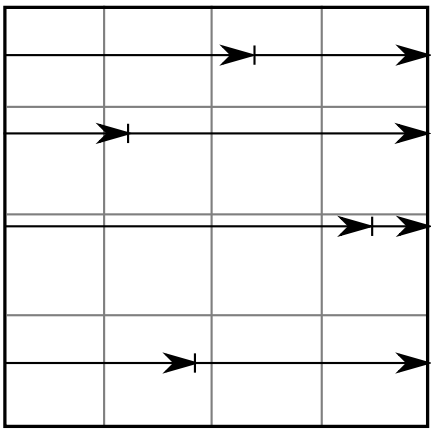

Figure 3.4.1: Schematic drawing of background photon propagation in one dimension only. A random starting point is chosen. Then the background package is propagated using periodic boundary conditions out of the box, and back in at the other side for one box length.

of the simulation box. Equation (3.4.9) is further converted into our chosen units for the package energy $\tilde{N}_\gamma$.

It must be cautioned, that the parameter f_l for the mean cell crossing length (see Equation 3.4.16) needs to be changed to $f_l = 1.0$ when propagating photons perpendicular to the box border. This is to prevent systematic underestimation of the energy content deposited in the cell. Since packages now have preferred directions, the original value of $f_l = 0.56$ in the CRASH scheme cannot be used and the mean cell crossing length changes.

As mentioned before, we experienced some issues with letting the background radiation simply emerge from the sides. The core cells in the middle of the box will have a systematically reduced energy deposit by background photons than cells near the border. This is problematic, so we decided to choose a different scheme. As in Maselli and Ferrara (2005), we start by determining a random cell in the box as the origin of a background photon. The density of the origin cell is checked and if the density is higher than a certain threshold δ_{BG} (we chose $\delta_{BG} = 1$), a new cell is randomly picked. Now instead of randomly determining a direction for the photon, a direction perpendicular to one of the box faces is chosen randomly.

Then, the background package is propagated using periodic boundary conditions, but only for the length of one box length. A schematic illustration of this procedure is found in Figure 3.4.1. This ensures homogenic sampling of the background radiation.

3.4.1.3 Diffuse Component Package

The spectrum produced by recombining electrons has already been discussed. The technical implementation of this diffuse component is also quite straight

forward. The diffuse component of recombining electrons is isotropic, but the scheme easily allows for non isotropic components as well.

To determine the frequency of the monochromatic diffuse photon package, Equation (3.2.25) is sampled using the rejection technique. This assumes, that all recombination events occur to the same atomic level and that all recombining electrons possessed the same kinetic energy. The only problem is to determine the energy content of the package and how and when diffuse photon packages are produced.

For this, an additional variable for the physical properties is saved in the grid. For each cell, the number of recombinations in each cell is saved. For a time interval Δt the number of recombinations are

$$\Delta N_{rec} \simeq \alpha\left(T_{i-1}\right) n_{e,i-1} n_{HI,i-1} \Delta t \Delta x^3 \tag{3.4.11}$$

or in comoving coordinates

$$\Delta N_{rec} \simeq \frac{\alpha\left(T_{i-1}\right)}{a(z)^3} n_{e,i-1} n_{HI,i-1} \Delta t \Delta x^3 \tag{3.4.12}$$

where the index $i-1$ indicates, that these variables are evaluated for the time t_{i-1}. ΔN_{rec} is added to the total recombination events counted for each cell $N_{rec,c}$ at coordinates $c=(x,y,z)$ every time a photon package crosses a cell (we have chosen $N_{rec,c}/\Delta x^3$ as units).

A photon package is produced by a cell, when a certain fraction from the total atom number in the cell has recombined.

$$N_{rec,c} > f_r N_a \tag{3.4.13}$$

Here N_a is the total number atoms in a cell. After a cell produced a diffuse photon, $N_{rec,c}$ is set to zero.

Since $\alpha\left(T_{i-1}\right)$ captures all recombining electrons, including the ones to different energy levels, we need to determine the fraction of photons stemming from direct recombination to the ground level. Two possible recombination algorithms have been implemented in ACRASH. The original one of CRASH proposes sampling the fraction of $\alpha_{HI,1}/\alpha_{HI}$, where $\alpha_{HI,1}$ is the direct recombination probability to the first level. A random number is chosen and if this number is smaller than $\alpha_{HI,1}/\alpha_{HI}$, a photon package is released. This could bias the diffuse component, since many relevant photons are ommited, especially when the fraction is very low, but the number of reemitted photons is high. ACRASH therefore implements a second method, where a photon package is produced at each recombination event (3.4.13), but the number of photons in the package is reduced accordingly to the fraction $\alpha_{HI,1}/\alpha_{HI}$. This results in more photon packages and can increase calculation time greatly, but samples the diffuse component better.

It is noted that in ACRASH, only the production of recombining photon packages is treated discretely. The treatment of recombination in solving the rate equations is continuous. If recombination is also treated discretely in the chemistry solver, adiabatic cooling would be over estimated.

3.4.2 Package Propagation

As has been mentioned, photon packages are produced in a Monte-Carlo fashion. Each type of source will produce a certain number of photon packages per time step. For this, the spectral energy distribution function and the angular distribution of each source is sampled. We now want to discuss, how photon packages are treated further in the integration process. Once they are produced by the source, they will be propagated through the simulation box at the speed of light. This is a major difference to the original CRASH scheme and whether this has an effect on the solution or not will be investigated.

The direction $\vec{D}$ with which the packages are propagated is known, after they habe been created. The equation of a straigt line is then used to determine the current position of the package. Instead of evaluating the equation of a straigt line each time a package is processed, we simply advance the package by the direction vector $\vec{D}$ which has the length of one step-length $f_l \Delta x$. The factor f_l determines how big a step is and will gain a more important meaning later.

We then calculate the cycle time, when the photon package arrives at the next step along its ray. This is when the time for the package to travel the distance $f_l \Delta x$ at the speed of light passed. In CRASH, this is omitted and the package is propagated along its ray until it leaves the box or is absorbed, without considering the propagation time. This corresponds to an infinite speed of light.

It is possible, that the photon package has not travelled out of the cell it was in. If this happens, we should not sample the same cell again and we just advance the package without depositing any photons and without solving the chemistry again.

Once again, we remind that our photon packages are monochromatic. Because we are only interested in the ionisation process, photoionisation is the only process affecting a package. The opacity contribution of the current cell needs to be determined and the energy content (i.e. the number of photons) of the package reduced accordingly. The absorption probability at the current cell with the discrete optical depth $\Delta\tau^l$ is then

$$P(\tau) = 1 - e^{-\Delta\tau^l} \tag{3.4.14}$$

The contribution $\Delta\tau^l$ of the l-th cell to the total optical depth along the ray is in case of hydrogen only

$$\Delta\tau^l = \sigma_{H^0}(\nu) n^l_{HI} f_l \Delta x \tag{3.4.15}$$

or in the comoving case

$$\Delta\tau^l = \frac{\sigma_{H^0}(\nu)}{a(z)^2} n^l_{HI} f_l \Delta x \tag{3.4.16}$$

where $\sigma_{H^0}(\nu)$ is the neutral hydrogen photoionisation cross-section, $n^l_{H^0}$ is the neutral hydrogen number density in the cell and $f_l \Delta x$ is the mean crossing path of a ray through a cell with the size Δx. CRASH uses the mean crossing path through a cell instead of the real crossing path and ACRASH adopts the

same strategy. f_l is determined through randomly intersecting rays through a box and has the value $f_l = 0.56$.

In the course of testing our code, we have realised, that this strategy is not as good as it might seem. Artifacts are introduced due to over- and underestimating the optical depth in certain cells. In the case of a point source, cells where the absorption is systematically underestimated are the ones parallel and diagonal to the box edges. The problem of underestimation was severe in our treatment of background radiation photons. In this special case f_l should be unity, since packages are propagated parallel to the box faces. In future versions of our code, we will therefore determine the correct intersection length of the ray using fast methods used in computer graphics (Amanatides and Woo (1987)).

To determine how many photons are absorbed in a cell N_A^l we use

$$N_A^l = N_\gamma^l \left(1 - e^{-\Delta\tau^l}\right) \tag{3.4.17}$$

where N_γ^l is the number of photons still remaining in the package after propagating up to the l-th cell. N_A^l is then subtracted from the photon package and is propagated further along the ray

$$N_\gamma^{l+1} = N_\gamma^l - N_A^l \tag{3.4.18}$$

Sometimes it can occur, that N_A^l is bigger than the number of remaining neutral atoms N_{ion}^l in a cell. This needs to be checked and if true, $N_A^l = N_{ion}^l$. Of course, the exceeding number of photons remains in the package.

The package is followed until it exits the box (open boundary conditions) or is considered extinct. This is the case when $N_\gamma^l < 10^{-p} N_\gamma$ where N_γ was the original amount of photons at creation time. Energy is conserved to an equivalent accuracy of 10^{-p}. In (Maselli et al. (2003)) they adopted $p \in [4, 9]$ where for our calculations presented here we constantly used $p = 8$.

3.4.3 Solving for the Chemistry

Now that the number of absorbed photons is know, physical quantities need to be updated. Using this information, the rate equations of the gas and the temperature equation can be solved. In the present version of ACRASH, the system of equations to be evaluated is simple, i.e. one equation for the ionisation fraction $x_{HII} = n_{HII}/n_H$ and one for the temperature T.

The system of coupled ordinary differential equations is thus

$$n_H \frac{dx_{HII}}{dt} = \gamma_{HI}(T) n_{HI} n_e - \alpha_{HII}(T) n_{HII} n_e + \Gamma_{HI} n_{HI} = I_{HII} \tag{3.4.19}$$

$$\frac{dT}{dt} = \frac{2}{3 k_B n_{tot}} \left[k_B T \frac{dn_{tot}}{dt} + \sum_{A,B} \mathcal{H}(T, x_{A,B}) - \sum_{A,B} \Lambda(T, x_{A,B}) \right] \tag{3.4.20}$$

The first equation gives the evolution of the ionisation fraction of hydrogen. Different mechanisms need to be accounted for. The first term on the right hand

side gives the contribution to ionised hydrogen by collisional ionisation. The second term describes recombination and the third considers photoionisation. Equation (3.4.20) gives the temperature evolution representing the equation ensuring energy conservation. Here k_B is the Boltzmann constant, n_{tot} is the total atom number density, $\mathcal{H}(T, x_{A,B})$ the heating function for species A ionisation state B and $\Lambda(T, x_{A,B})$ the cooling function. All the contributions to the heating and cooling term from all species need to be accounted for. Equations (3.4.19) and (3.4.20) are general equations and need to be discretized. To include more species, analogue equations to (3.4.19) have to be added to the system.

The discretisation process in general is straight forward

$$\begin{aligned} x_{HII}(t+\Delta t) &= x_{HII}(t) + I_{HII}(t)\Delta t/n_H \\ T(t+\Delta t) &= T(t)+ \\ &+\frac{2}{3k_B n_{tot}}\left[k_B T \Delta n_{tot} + \Delta t\left\{\sum_{A,B}\mathcal{H}(T, x_{A,B}) - \sum_{A,B}\Lambda(T, x_{A,B})\right\}\right] \end{aligned} \tag{3.4.21}$$

where $\Delta n_{tot} = n_{tot}(t+\Delta t) - n_{tot}(t)$. This system is solved every time a photon package crosses a cell. All the rates need to be transformed to comoving coordinates accordingly.

A difficulty of equation (3.4.21) and the CRASH scheme is Δt. The time between two crossings of the same cell by two photons varies from cell to cell due to stochasticity. A scheme which would fix Δt for every cell, would be the normal ray-tracing scheme. If Δt is fixed, each cell must be reached by a photon in every time-step. In CRASH the idea is to minimize the amount of ray-tracing needed, which is done through the Monte-Carlo scheme.

To determine Δt in CRASH for each cell, a new grid is allocated in memory, where the integer cycle number is stored in the cell, every time a photon passes through it. The time difference can then be easily computed by determining the difference between the current cycle number and the last passage $\Delta t = [j_{curr} - j_{last}(x, y, z)]\, dt$. j_{curr} is the current cycle number, j_{last} the one of the last passage through the cell and dt is the physical time step.

As pointed out in Maselli et al. (2003), it is not straightforward to recover continuous quantities that directly depend on its intensity, since the radiation field is discretized in photon packages. These quantities are photoionisation and photoheating rates. Photoionisation rates are easy to determine, since they are direct proportional to the number of photons absorbed in one cell. For species A in its neutral state BI the change in ionisation fraction would be

$$\Delta x_A = \frac{n_{A,BI}}{n_A}\Gamma_{AI}\Delta t \equiv \frac{N^l_{A,BI}}{N^l_A} \tag{3.4.22}$$

where $n_{A,BI}$ is the neutral (ground) species number density, n_A the total number density of the species, $\Gamma_{A,BI}$ the photoionisation rate of neutral (ground) species. N^l_A gives the atom number of species A in the cell and $N^l_{A,BI}$ gives

the number of photons absorbed in the cell due to the neutral (ground) species BI.

Since only opacity contributions of each species in the cell and the total number of absorbed photons are passed to the chemistry solver, the contribution $N^l_{A,BI}$ needs to be expressed through the absorption probability $1 - e^{-\Delta\tau^l_A}$. With this in mind (3.4.22) becomes for species A_i in state B

$$\Delta x_{A_i,B} = \frac{N^l_{A_i,B}}{n^l_{A_i,B}(\Delta x)^3} \left(\frac{1 - e^{-\Delta\tau^l_{A_i,BI}}}{\sum_{A,B}\left(1 - e^{-\Delta\tau^l_{A,B}}\right)} \right) \tag{3.4.23}$$

where Δx is the cell size, and $\sum_{A,B}\left(1 - e^{-\Delta\tau^l_{A,B}}\right)$ is the sum of all absorption probabilities from all species A and states B in the simulation.

The discrete contributions to photoheating are adiabatic heating due to the increase in total number density at constant pressure and volume, and the energy deposit due to the ionised electron's remaining energy. With these two effects in mind, the discretised contribution to the temperature is given by

$$\Delta T = \frac{2}{3k_B n_{tot}} \left\{ k_B T \Delta n_{tot} + \sum_{A,B} \left[n^l_{A,B} \left(h\nu - h\nu_{th,A,B} \right) \right] \right\} \tag{3.4.24}$$

where $n^l_{A,B}$ is the photon energy density $n^l_{A,B} = N^l_{A,B} / (\Delta x)^3$ of species A in state B, ν is the current wavelength of the photon package, and $\nu_{th,A,B}$ is the ionisation threshold wavelength.

All the other contributions like recombinations, collisional ionisations and cooling are treated as continuous processes. This can cause problems with the time stepping, since continuous processes need smaller time steps, than the actual time step of the discretised components. Therefore it is essential to check, if Δt in the cell is smaller or bigger than the smallest characteristic timescale of the continuous processes, i.e. $\Delta t \ll t_{min} = \min\left[t_{rec,B}, t_{coll,A}, t_{cool}\right]$.

If this condition is not met for the current cell, then the integration process of the chemical equations needs to be reduced to n_s sub-cycles with

$$n_s = \mathrm{int}\left[\frac{\Delta t}{f_s t_{min}} \right] \tag{3.4.25}$$

where f_s is the so called fudge factor. This factor is given as $f_s = 50 - 100$ by Maselli et al. (2003). We went for $f_s = 10$ for all the work presented here, since we found this to be reasonable accurate.

3.4.4 Time Stepping and Errors

In the section above, we mentioned that time stepping can be very important in reaching the desired accuracy, since continuous processes are intertwined with discretised processes.

It is very hard to sample the total 7D parameter space of the radiative transfer equation equally well in each parameter. The sampling is controlled through

the number of photon packages chosen. Since with each photon package many different dimensions of the parameter space are sampled simultaneously, the overall sampling is quite poor. With each package, the frequency space and the angular parameter of the source is sampled. Then, through propagating the packages through the simulation box, the spatial parameters are sampled. But sampling is not constant, it is proportional to the distance from the source. Cells nearer to the source will have a higher probability to be hit by a photon package than cells further away.

All these effects make time stepping for the CRASH scheme hard. In the current version of ACRASH, the only parameter governing the sampling resolution is the number of photons and number of time steps. No care is taken, whether the amount of photons is sufficient for a simulation or not. Further the code does not check, if the conditions for good sampling presented below are maintained at all times. Further versions of the code will be able to do this, but at the moment it was crucial that total control over execution time was present, and that we were able to study resolution effects in more detail.

The sampling resolution of the CRASH scheme depends on the following input parameters: N_p the number of photon packages emitted per source, N_c^3 the number of grid cells and N_s the number of sources in the simulation. With these parameter, a simple resolution criteria can be derived, as has been done for the original CRASH scheme.

To determine how well the problem is sampled, one can calculate the mean number of times a cell is crossed by photon packages. For this the total number of packages in the simulation $N_s N_p$ is taken. Now we determine how many cells are crossed on average by one package $f_d N_c$ where f_d is $f_d \approx 1$ for optically thin media and $f_d \approx N_c^{-1}$ for optically thick media. It is therefore between $f_d = \left[N_c^{-1}, 1\right]$. The number of crossings is thus

$$N_{cr} = \frac{N_s N_p f_d N_c}{N_c^3} = f_d \frac{N_s N_p}{N_c^2} \tag{3.4.26}$$

This can now be coupled to a time step criteria. To properly account for all continuous processes, the minimum time-scale in the simulation box t_{min} needs to be determined. For this, mean values of the recombination, collisional ionisation, and cooling time-scale are determined. We set $t_{min} = \min\left[t_{rec,B}, t_{coll,A}, t_{cool}\right]$ and

$$\langle \Delta t \rangle = \frac{t_s}{N_{cr}} \ll t_{min} \tag{3.4.27}$$

must hold. With this, the number of crossings need to be

$$N_{cr} = f_d \frac{N_s N_p}{N_c^2} \gg \frac{t_s}{t_{min}} \tag{3.4.28}$$

This criterium has to be met at all times during the simulation, and the time step should be adjusted accordingly if it is not fulfilled. ACRASH is not able to do so at the moment, but later version of the code will.

Another important parameter is the fraction of atoms that in one cell could be ionised by a photon package N_γ / N_a. The lower this factor is, the higher

the resolution. This would make photoionisation and photoheating processes more continuous.

A rough estimate for the compuational cost of the CRASH scheme is given through the total number of photons that need to be evaluated, i.e. $N_c^3 N_{cr} = f_d N_c N_p N_s$. But in reality this is only valid, if recombination processes are excluded.

3.5 Flowcharts

Red colour symbolises program parts not yet implemented.

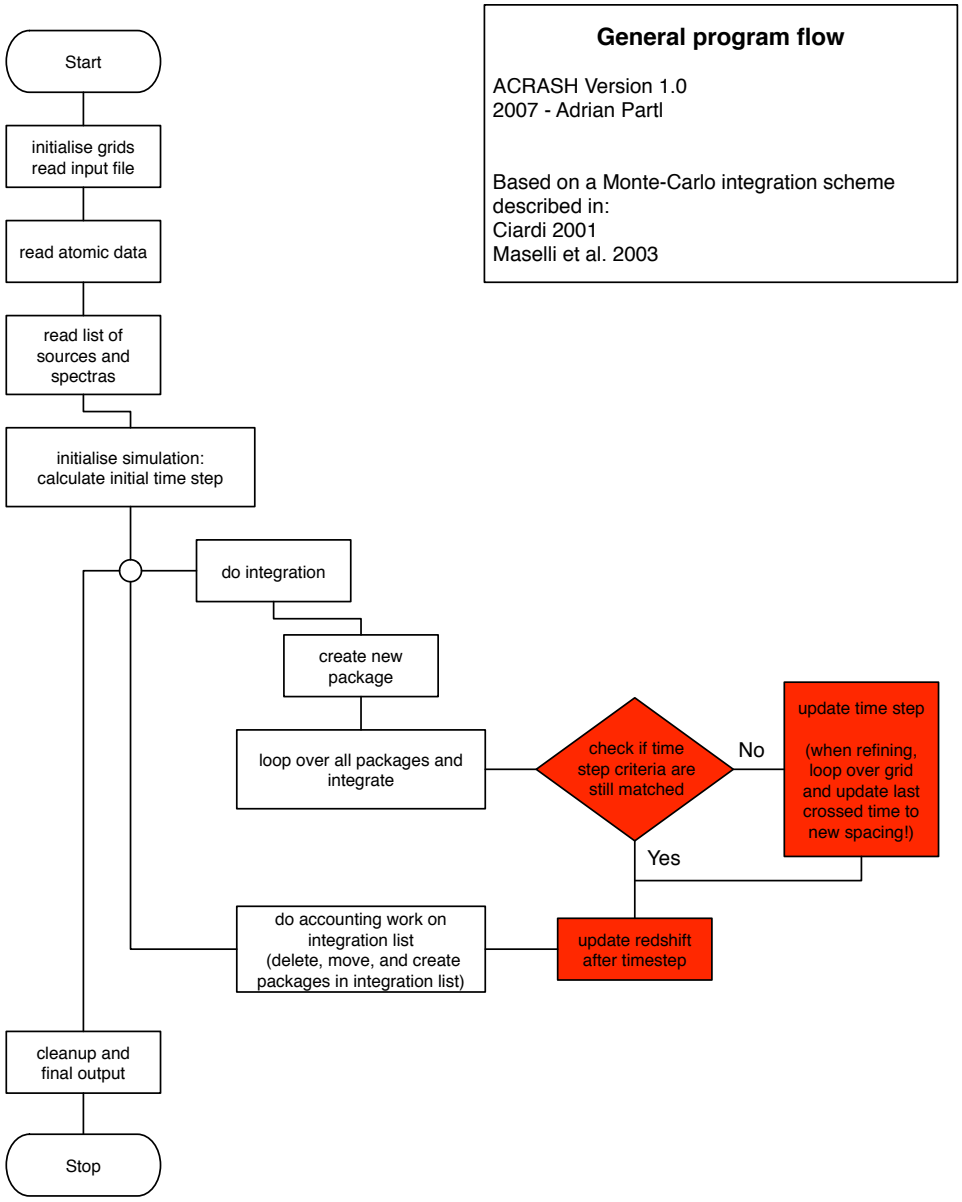

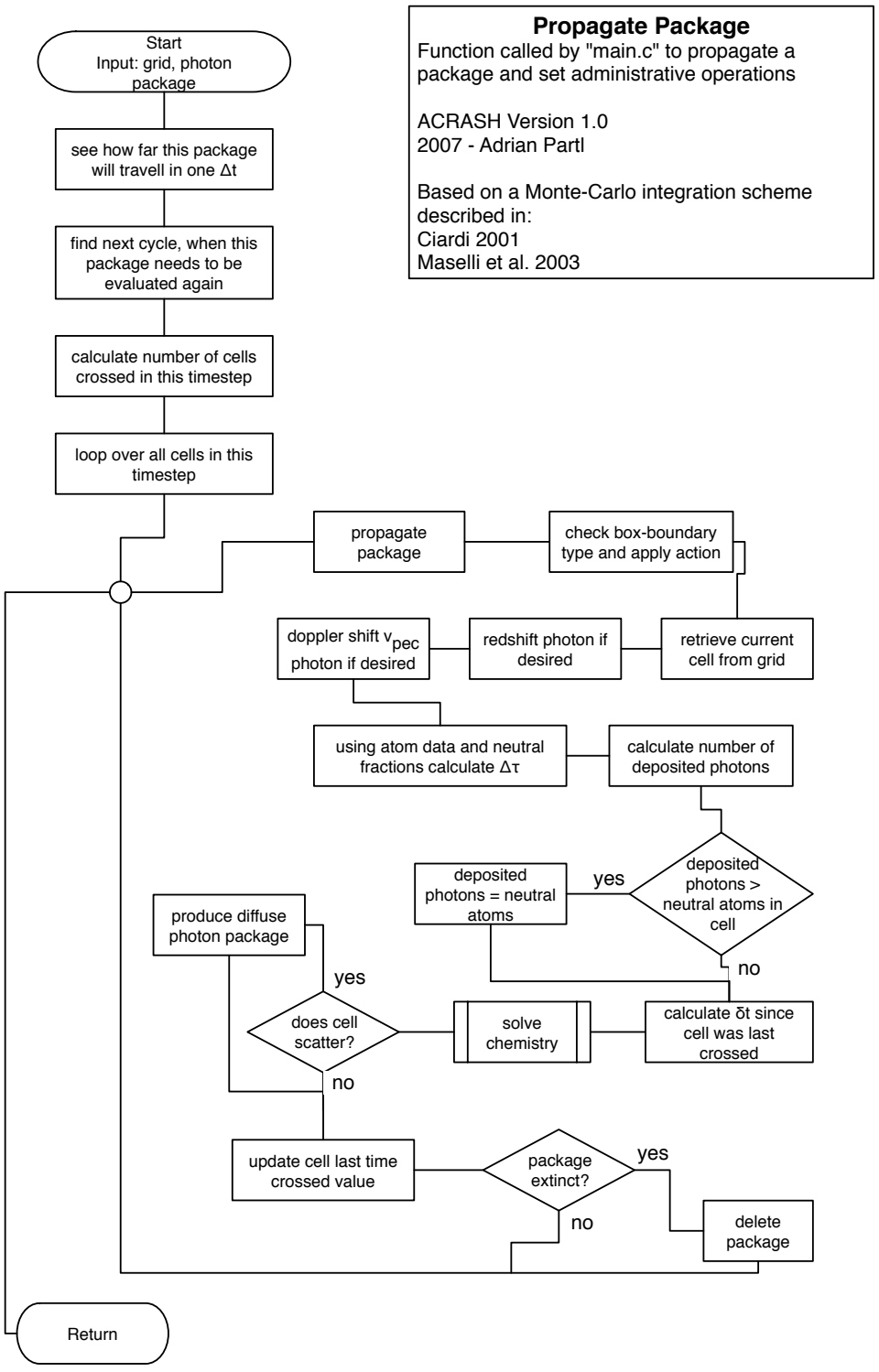
Propagate Package
Function called by "main.c" to propagate a package and set administrative operations
ACRASH Version 1.0
2007 - Adrian Partl
Based on a Monte-Carlo integration scheme described in:
Ciardi 2001
Maselli et al. 2003
Start
Input: grid, photon package
see how far this package will travell in one Δt
find next cycle, when this package needs to be evaluated again
calculate number of cells crossed in this timestep
loop over all cells in this timestep
propagate package
check box-boundary type and apply action
retrieve current cell from grid
redshift photon if desired
doppler shift v_pec photon if desired
calculate number of deposited photons
using atom data and neutral fractions calculate Δτ
deposited photons > neutral atoms in cell
yes
deposited photons = neutral atoms
no
calculate δt since cell was last crossed
solve chemistry
does cell scatter?
yes
produce diffuse photon package
no
update cell last time crossed value
package extinct?
yes
delete package
no
Return

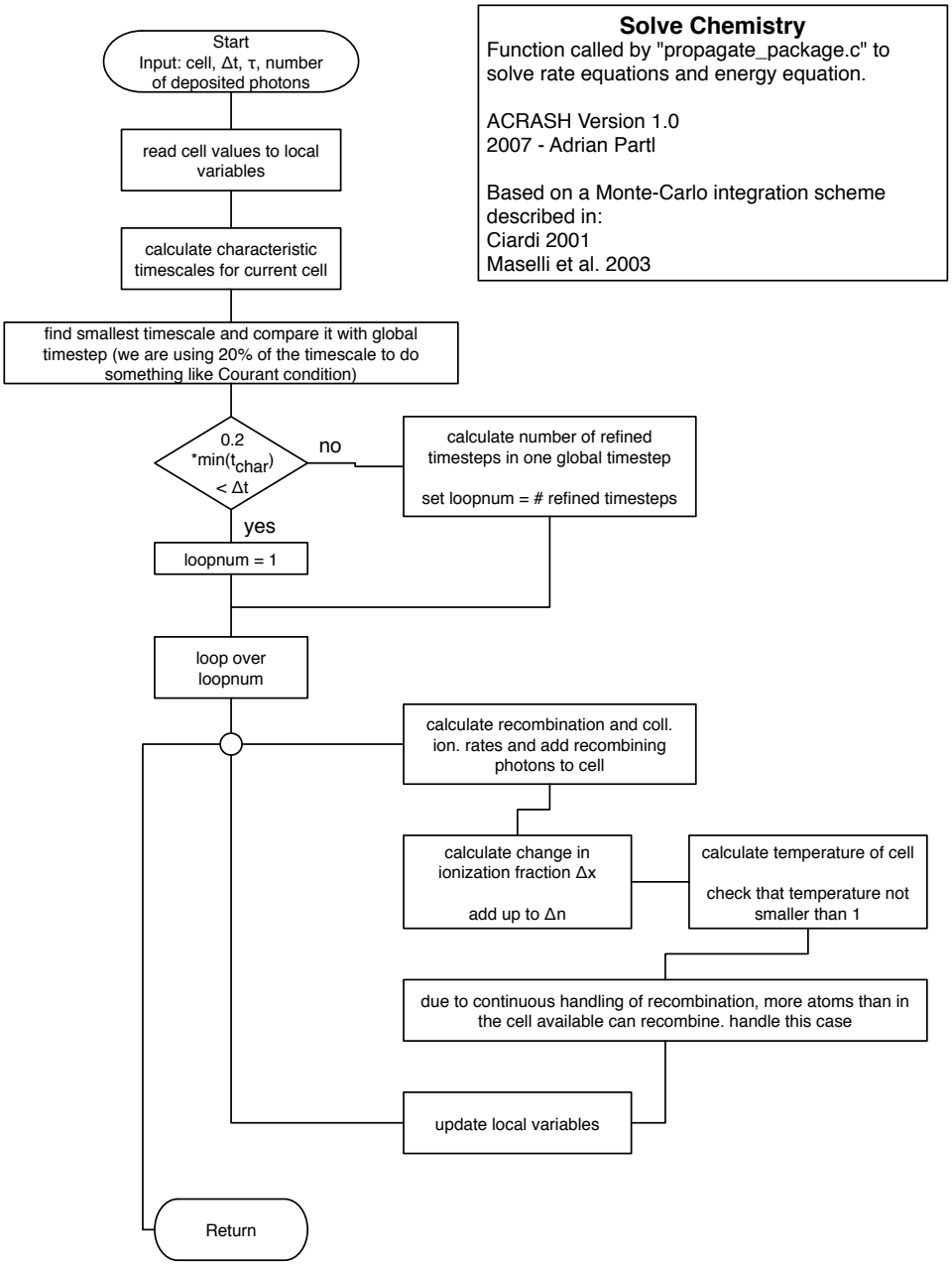
Solve Chemistry
Function called by "propagate_package.c" to solve rate equations and energy equation.
ACRASH Version 1.0
2007 - Adrian Partl
Based on a Monte-Carlo integration scheme described in:
Ciardi 2001
Maselli et al. 2003
Start
Input: cell, Δt, τ, number of deposited photons
read cell values to local variables
calculate characteristic timescales for current cell
find smallest timescale and compare it with global timestep (we are using 20% of the timescale to do something like Courant condition)
0.2 *min(t_char) < Δt
no
calculate number of refined timesteps in one global timestep
set loopnum = # refined timesteps
yes
loopnum = 1
loop over loopnum
calculate recombination and coll. ion. rates and add recombining photons to cell
calculate change in ionization fraction Δx
add up to Δn
calculate temperature of cell
check that temperature not smaller than 1
due to continuous handling of recombination, more atoms than in the cell available can recombine. handle this case
update local variables
Return

4 Testing the Code

4.1 Isothermal Strömgren Sphere Test

A basic test for any continuum transfer code is the Strömgren sphere test. This is one of the few cases, where an analytical solution is available. For this test, numerous approximations are made. The test is carried out in homogeneous hydrogen gas, using a monochromatic source with constant flux at its center. The HII region then expands in this medium without depositing any thermal energy (isothermal approximation).

The Strömgren sphere will grow until an equilibrium between ionisation and recombination is reached. The radius of this sphere is called the Strömgren radius R_S

$$R_S = \sqrt[3]{\frac{3}{4\pi}\frac{\dot{N}_\gamma}{n_H^2 \alpha_{HI,B}}} \tag{4.1.1}$$

where $\dot{N}_\gamma$ is the photon number flux and $\alpha_{HI,B}$ is the hydrogen recombination coefficient to all levels excluding events to the first $\alpha_{HI,B} = \alpha_{HI} - \alpha_{HI,1} \approx 3 \times 10^{-13}\mathrm{cm}^3\mathrm{s}^{-1}$ (Shu (1991)). The approximation of the Strömgren sphere uses the on-the-spot approximation. This should be kept in mind when comparing our results with the analytic solution. The evolution in time is given by (Spitzer (1998))

$$R_a(t) = R_S \left(1 - e^{-n_H \alpha_B t}\right)^{1/3} \tag{4.1.2}$$

In a cosmological context, the Strömgren radius needs to be multiplied by the scale factor $a(z) = 1/(1+z)$ and becomes $R_{S,co}(z) = R_S \cdot a(z)$ (Shapiro and Giroux (1987)). This is for comoving coordinates. Since in ACRASH comoving coordinates are used, all distances below are given in comoving coordinates.

In our test runs, we used the setup proposed in Maselli et al. (2003). The Strömgren sphere should form in a homogeneous medium with $n_H = 1\mathrm{cm}^{-3}$ at a fixed temperature of $T = 10^4\mathrm{K}$. The initial ionisation fraction was set at $X_{HI} = 1.2 \times 10^{-3}$. For redshift $z = 0$ a box with $L_{box} = 70\mathrm{pc}$ and $N_c^3 = 128^3$ grid cells is used. For the tests at other redshifts, the box size is scaled with the scale length $a(z)$ to ensure similar spatial resolution. We let the simulation run for about five recombination time-scales.

The monochromatic source emits photons at $13.6\ \mathrm{eV}$ with a photon rate of $\dot{N}_\gamma = 10^{48}\mathrm{s}^{-1}$. It is located at the center of the box. For redshift $z = 0$ we run this test with and without recombination scattering to see, if its implementation is correct. Further the redshift zero run has been used to identify effects of the f_r parameter, regulating the production of diffuse photons. A comprehensive resolution study has been carried out. Possible effects of our time step criteria are studied as well. Then we checked the cosmological implementation with

Redshift	Scattering	Box size [pc]	Simulation time [yr]
$z = 0$		$d = 70.0$	$t_{sim} = 6.0 \times 10^5$
$z = 0$	x	$d = 70.0$	$t_{sim} = 6.0 \times 10^5$
$z = 3$	x	$d = 16.0$	$t_{sim} = 1.0 \times 10^5$
$z = 6$	x	$d = 10.0$	$t_{sim} = 1.0 \times 10^4$

Table 4.1: Simulation parameters for the Strömgren sphere test. A monochromatic source with $\dot{N}_\gamma = 10^{48}\mathrm{s}^{-1}$ and $\lambda = 912$ Å has been used. The initial density was $n_H = 1.0\ \mathrm{cm}^{-3}$ comoving for each redshift. The initial ionisation fraction was set at $X_{HI} = 1.2 \times 10^{-3}$ at a constant temperature of $T = 10^4$ K. The grid resolution was 128^3 and the box-size was chosen to result in similar numerical resolution for each redshift. A scattering parameter $f_r = 0.1$ has been used.

runs for redshift $z = 3$ and $z = 6$. A summary of all test runs is found in Table 4.1.

To derive quantities that are comparable to the analytical solution (i.e. the Strömgren radius), we adapted the method proposed in Maselli et al. (2003). The radius is derived from the total volume of the ionised region using

$$R_n = \sqrt[3]{\frac{3}{4\pi} V_n} \tag{4.1.3}$$

where V_n is the volume of the sphere. The volume is measured using

$$V_n = \sum_{ix,iy,iz} x_{HII} \left(\Delta x\right)^3 \tag{4.1.4}$$

4.1.1 Without a Diffuse Component

The first test performed was the Strömgren sphere test without recombination scattering, to see, if scattering is implemented reasonably and to see, if the implementation of the source and propagation of photon packages work well. The tests were carried out using $N_p = 10^6, 10^7, 10^8$ photon packages. The results are then compared to the analytical result (Figure 4.1.1).

As is seen in Figure 4.1.1, the solution converges with $N_p = 10^7$ which corresponds to $N_{cr} = 5$ crossings of one cell. The sampling criteria for this simulation is $N_p = N_{cr} \times 2 \times 10^6$. It is therefore not surprising, that convergence is not yet reached for $N_p = 10^6$.

It is interesting, that the solution without scattering differs by about 10% to the analytical solution. This means, that in reality a diffuse component greatly influences the Strömgren sphere and is needed to reproduce HII regions properly. Of course it can be argued that this is not necessary, since the on-the-spot approximation can be used. As has been discussed in Ritzerveld (2005) this is problematic, since large parts of a HII region are dominated by a diffuse component, for example the outer parts of the HII region. He shows, that the outer 12% of the region is dominated by this diffuse component, comparing well with our results, where the region is 10% too small.

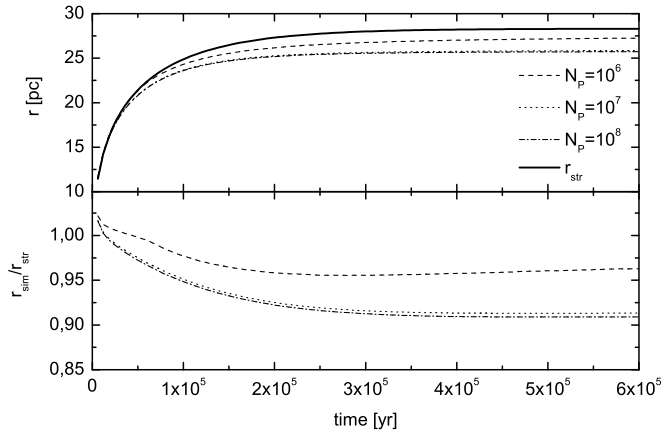

Figure 4.1.1: Evolution of the Strömgren sphere test without a diffuse component. The results of our simulations are compared to the analytical result (thick black line). Different resolutions have been used. The bottom plot gives the percental deviation from the analytical result.

4.1.2 With a Diffuse Component

As has been seen above, the correct Strömgren radius cannot be reached without a diffuse component. It is thus very important in the formation of HII regions. In order to correctly simulate this diffuse component, the simulation parameter f_r regulating the sampling of the diffuse field needs to be assessed.

We conducted the Strömgren sphere test with sufficient photon packages ($N_p = 10^8$) to see, how this parameter effects the overall solution. We compare test runs for $f_r = 0.30, 0.20, 0.10, 0.05, 0.01$ and compared the resulting Strömgren radius with the analytic solution. Results are shown in Figure 4.1.2.

It can be seen, that including the diffuse component, the Strömgren radius is reproduced up to 1%. The influence of f_r can be clearly seen. If sampling of the diffuse component is too low, the Strömgren sphere does not evolve smoothly, as is visible in the wiggles of $f_r = 0.3$ and $f_r = 0.2$ in Figure 4.1.2. For lower values, the evolution is smooth and seems to converge. The solutions of $f_r = 0.05$ and $f_r = 0.01$ only differ by some tenth of a percent.

A note on the solution of $f_r = 0.20$ should be added. At $t = 5 \times 10^6$ yr a sudden rise is present. This is due to the low resolution sampling of the diffuse component. Cells in the simulation need to wait until 20% of its content have recombined before a package is sent out. This will lead to a retardation of the influential effect and if f_r is too high, a big quantity of cells will suddenly trigger photon production. This leads to an artificially high photon flux which is responsible for the sudden expansion of the sphere. The same would probably happen, if the simulation for $f_r = 0.3$ would have been run longer. This effect is smeared out for lower values.

We can confirm the claim in Maselli et al. (2003), that a value of $f_r = 0.1$ is

a reasonable compromise between accuracy and performance. In the Strömgren tests presented below, this value has been used. In our production runs, we have used $f_r = 0.01$ to be sure that the diffuse component is sampled correctly.

We have seen, that the diffuse component plays an important role in reproducing HII regions correctly. Thus we cannot ignore recombination, at least in the context of the CRASH scheme. The effect is quite important and further attention on how the diffuse component is treated needs to be given in the

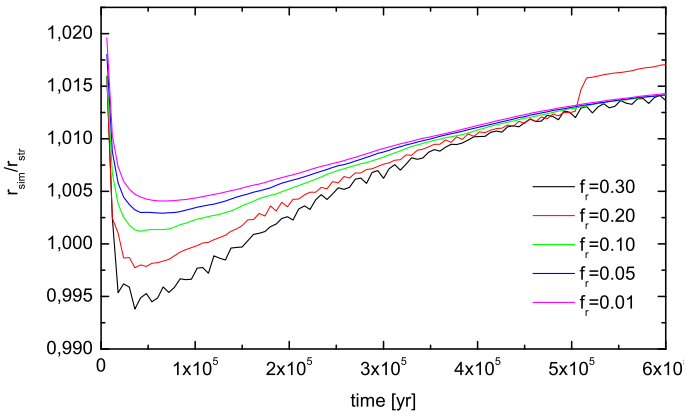

Figure 4.1.2: The influence of f_r on the evolution of the Strömgren radius with $N_p = 10^8$. Different values have been examined. The results are compared to the analytical solution.

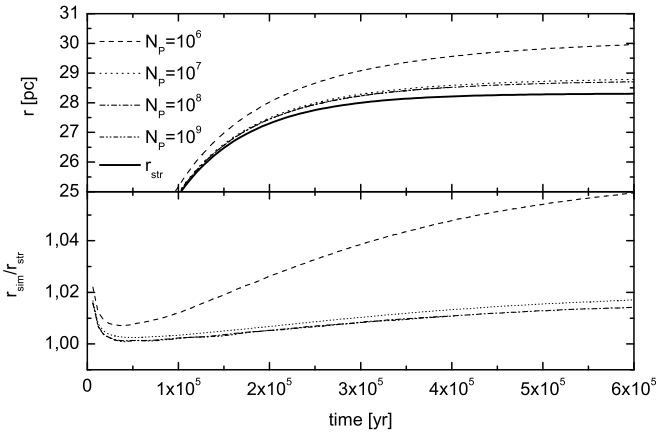

Figure 4.1.3: Evolution of the Strömgren sphere test with a diffuse component at $z = 0$. The results of our simulations are compared to the analytical result (thick black line). Different resolutions have been studied. The bottom panel gives the percental deviation from the analytical result.

future.

To test the resolution criteria and see, if convergence is reached, we conducted runs with $N_p = 10^6, 10^7, 10^8, 10^9$ for redshift $z = 0$. The $N_p = 10^9$ run had to be aborted, since it used too much memory (over $32\mathrm{GB}$). This run can only be carried out, if propagation at the speed of light is disabled. Then photon packages need not to be stored in memory from each time step to the next and memory consumption drops to $50\mathrm{MB}$. This is one of the extreme drawbacks of the speed of light implementation in ACRASH.

The results are shown in Figure 4.1.3. As in the test without the diffuse component, convergence is reached at around $N_p = 10^7$. A higher number of packages increases accuracy only by a slight factor. The difference between the 10^8 and 10^9 runs are barely seen. The Strömgren radius can thus be reproduced with an accuracy of about 2%. This is in accordance with the CRASH code, as can be seen in Maselli et al. (2003) Figure 3.

The CRASH code, and with this ACRASH as well, can handle ionisation spheres up to an accuracy of 2%. This is well in the accuracy regions of other existing codes (see Iliev et al. (2006)).

In Figure 4.1.4 we plot ionisation fraction cuts through the central region of the Strömgren spheres for all resolution runs. In the low resolution run with $N_p = 10^6$ the Monte-Carlo nature of the transport scheme is clearly seen. It is clear, that in this case sampling is too low to correctly reproduce the Strömgren sphere. But if one is only roughly interested in the position of the ionisation front, even a low sampling can produce a reasonable result.

These sampling artifacts disappear with higher package numbers and with 10^8 packages, a smooth and thin ionisation front can be produced. In the 10^9 run, the Monte-Carlo nature is completely invisible.

To test our redshift dependency implementation of the radiative transport problem, we conducted similar Strömgren sphere tests at different redshifts. The temperature and number densities were kept constant. The box size had to be adjusted, since the Strömgren radius shrinks in comoving coordinates with higher redshift. We wanted to keep the spatial resolution as similar as possible and reduced the box sizes accordingly. The spatial resolutions at high redshifts are thus comparable to the one at present.

For our redshift tests at $z = 3$ and $z = 6$ we obtained good results for $N_p = 10^8$ packages. It seems, that convergence is not reached as fast as with the redshift zero test. This is due to different densities, at higher redshift density is increasing. Higher densities can reduce the accuracy of the result and more photon packages are needed. This is best seen in Maselli et al. (2003) in their Figure 3, where they tested how accurate CRASH is working for different densities. Accuracy can decrease with higher densities.

The results of the redshift dependant Strömgren sphere tests are shown in Figures 4.1.5 and 4.1.6. For redshift $z = 3$, the highest resolution run used too much memory and had to be aborted.

We then studied if our changed time step criteria 3.4.3 has any influence on the solution. Three different time steps have been tested. First the case where one photon is emitted in each time step, then the cases with ten and one hundred photons per time step. The test has been carried out with 10^8

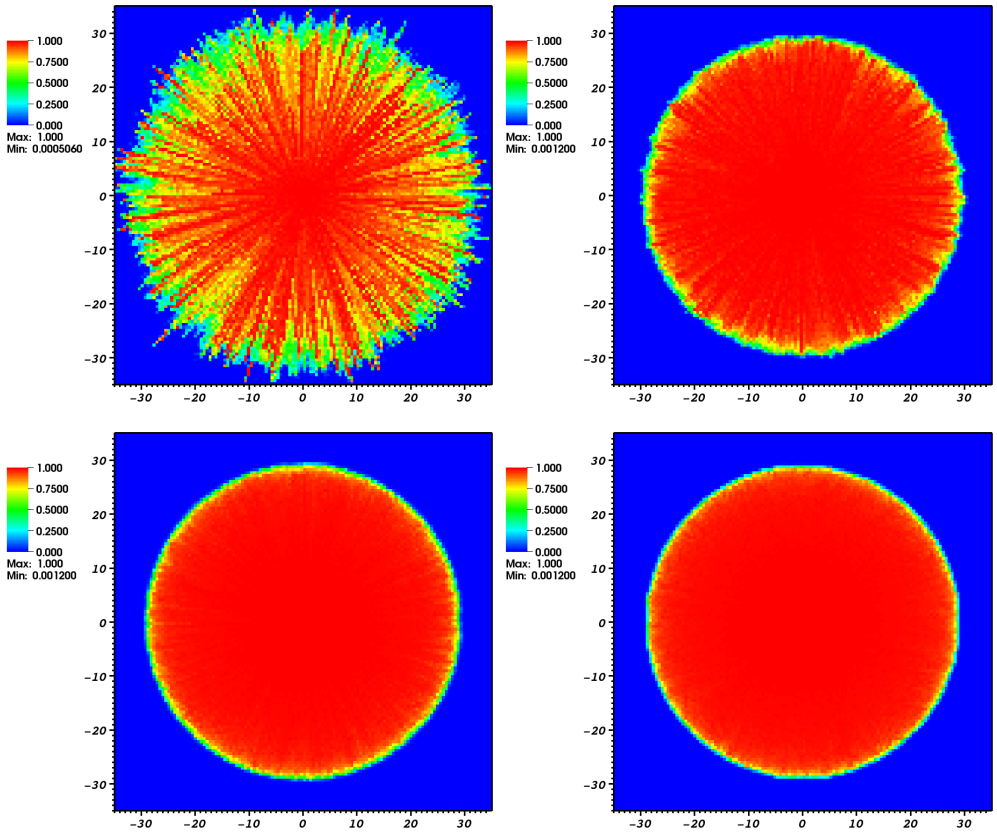

Figure 4.1.4: Visualisation of the central plane of the Strömgren sphere. Shown is the hydrogen ionisation fraction. The spatial axis are in parsec scale. From left to right and top to down are runs at different resolution $N_p = 10^6, 10^7, 10^8, 10^9$.

photon packages. As can be seen in 4.1.7, the modification of the time stepping criteria has no effect on the solution. At least to a factor of one hundred. It must be noted, that this must not be true in the infinite speed of light case.

4.2 Realistic Strömgren Sphere

The isothermal Strömgren sphere test cannot test CRASH/ACRASH ability to solve the energy equation. To test photo heating, a realistic Strömgren sphere needs to be calculated. Unfortunately there is no analytic solution to this test case.

We therefore compare our result to the well established 1D radiative transfer code CLOUDY, which is publicly available at www.nublado.org (Ferland et al. (1998)). We used the latest version of the code to obtain a reference. It must be noted, that CRASH and CLOUDY differ in many parts. CLOUDY uses complex models of atoms, instead CRASH/ACRASH uses a simple one level atom with $n = 1$ and the continuum $n = \infty$. The rate equations also differ slightly, which

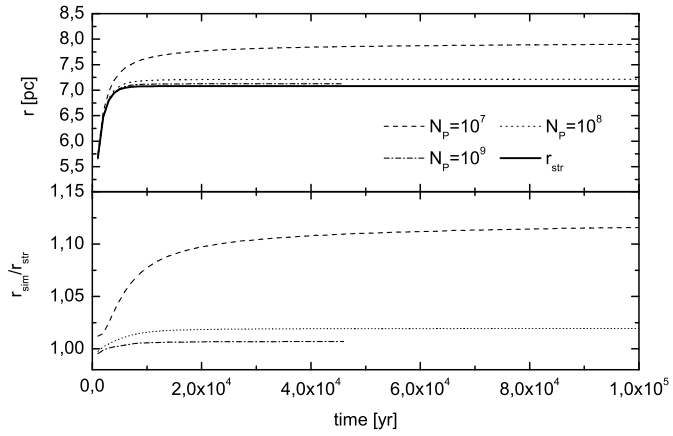

Figure 4.1.5: Evolution of the Strömgren sphere test with a diffuse component at $z = 3$. The results of our simulations are compared to the analytical result (thick black line). Different resolutions have been studied. The bottom panel gives the percental deviation from the analytical result.

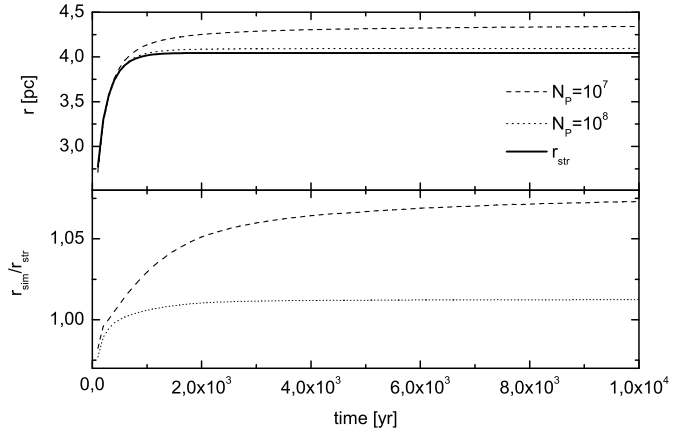

Figure 4.1.6: Evolution of the Strömgren sphere test with a diffuse component at $z = 6$.

is also a source for possible differences.

The HII region is being evolved in homogeneous hydrogen with a number density of $n_H = 1\mathrm{cm}^{-3}$ at an initial temperature of $T = 100\mathrm{K}$. The medium is totally neutral in the beginning. The box length is set at $L_{box} = 140\ \mathrm{pc}$ with a resolution of $N_c^3 = 256^3$. The simulated time is again $t_s = 6 \times 10^5 \mathrm{yr}$.

A black body radiator is used as source with a temperature of $T = 60000\mathrm{K}$ and luminosity of $L = 10^{38}\mathrm{erg\ s}^{-1}$. The source is located at the center of the box.

Once again the effects of a diffuse component are investigated. Another

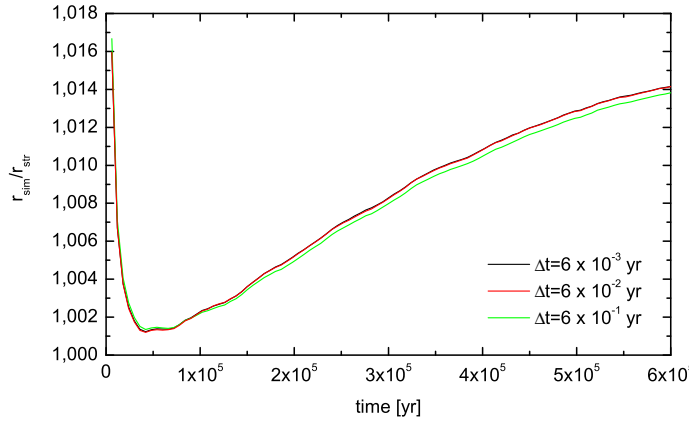

Figure 4.1.7: Time resolution test, with different time steps. For this test, 10^8 photon packages have been used. The time steps corresponds to one, ten, or one hundred photons produced per step.

emphasis is laid on the impact of resolution.

To transform our 3D solution into 1D for comparison with CLOUDY, we cast rays from the source to each cell on the face of the box extracting values along it. We then calculated the mean of all these rays and compared this with the CLOUDY result.

4.2.1 Without Recombination Scattering

In Figure 4.2.1 the resulting temperature and ionisation fraction profiles are compared to the reference calculation. To see the effects of numerical resolution, we again performed this test with $N_p = 10^6, 10^7, 10^8$ photon packages.

It is evident, that the 10^6 simulation provides a wrong result. The peaks in the solution are due to the noise introduced by the Monte-Carlo method. Since now a black body spectra is sampled, the energy contents of the packages can vary drastically. If a high energy photon is produced, it will have a very big energy content. The energy is even higher if less packages are being used. This is due to the bigger time step. This gives the high energy tail a bigger weighting, which is responsible for the very bad result. When including the energy equation, special care needs to be taken, that the sampling criterion in equation (3.4.27) is met at all times.

For higher number of photon packages, the solution converges. It is not surprising after our insights gained with the isothermal case, that lack of a diffuse field hinders the HII region to evolve properly. Again, the diffuse component is important in correctly replicating HII regions.

A note shall be added on the temperature profile of CLOUDY. As can be seen in Figure 4.2.1, the CLOUDY ionisation front is not sharp. Maselli et al. (2003) argue that this feature could result from heat transfer, which is included in CLOUDY. But the exact origin of this feature is unclear. Effects due to the boundary conditions are also a possible explanation.

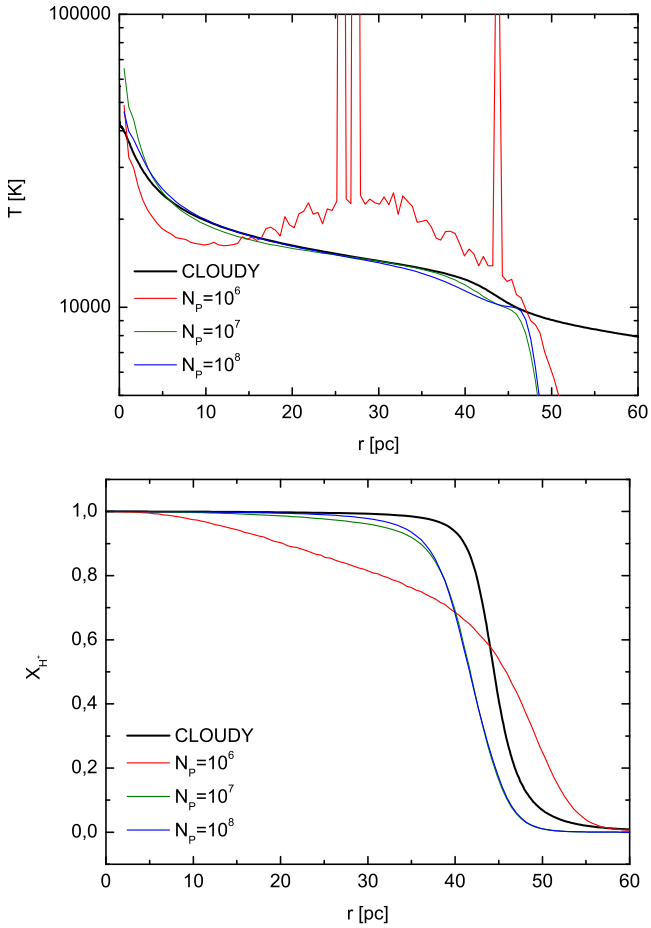

Figure 4.2.1: Temperature (top) and ionisation fraction (bottom) profiles of the test HII region in the equilibrium state. The results are compared to the CLOUDY reference calculation.

4.2.2 With Scattering

When turning the diffuse component on, our results compare favorably to the reference calculation. Again, the 10^6 resolution run is too low, but the 10^7 and 10^8 runs converge nicely. As can be seen in Figure 4.2.2 the profiles match quite well with the CLOUDY result. Small differences are present, but these are probably due to different handling of atomic processes and different rate equations. The position of the ionisation front deviates by about 10% to the reference position.

A closer look at the 10^7 run shows, that the ionisation front produced by that run is not as sharp, as the one in the 10^8 run. This can be clearly seen in the ionisation fraction profile, since it is declining earlier than the 10^8 run.

In Figure 4.2.3 the mean evolution of all cells $d = 40\mathrm{pc}$ away from the source is shown. Once more, the 10^6 package run is not reproducing the result well enough. The other two runs converge nicely. CRASH is performing very well

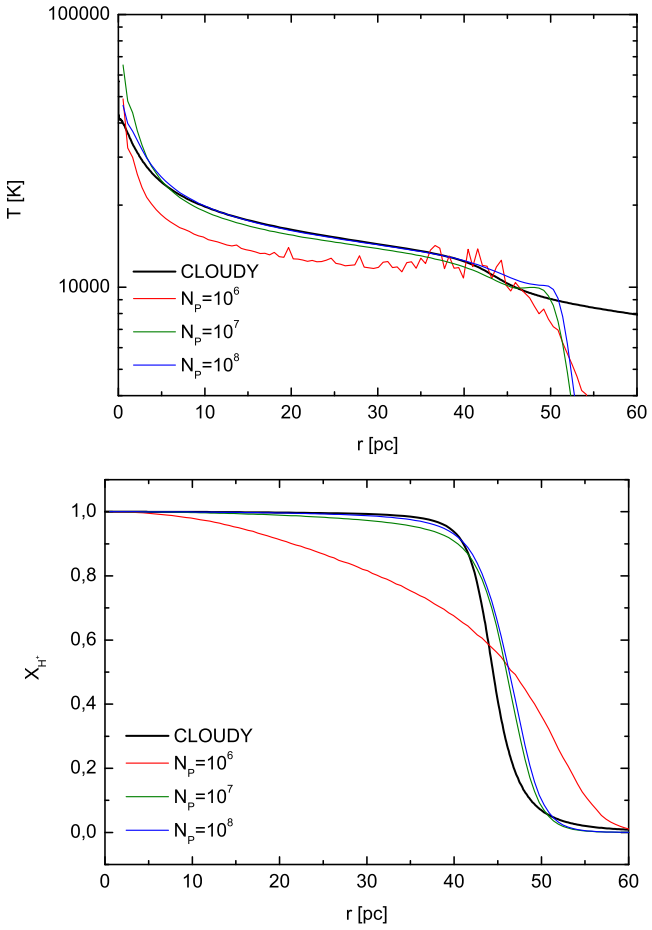

Figure 4.2.2: Temperature (top) and ionisation fraction (bottom) profiles of the test HII region in the equilibrium state. The results are compared to the CLOUDY reference calculation.

in capturing the sudden step in the ionisation fraction. The transition phase is very narrow and is almost a step function.

We can conclude, that CRASH/ACRASH is reproducing the evolution and structure of Strömgren spheres accurately to about 10%.

In Figure 4.2.4 we show cuts through the ionisation fraction and temperature data cube of the $N_p = 10^8$ run, our highest resolution run. Since the source is not monochromatic, the source spectrum needs to be sampled. This sampling is very poor and imprints into the ionisation and temperature fields. A polychromatic Monte-Carlo transport would reduce this effect drastically, because one would gain total control over frequency sampling.

Once again we checked, if our time step implementation could be influencing the solution. Since no analytical solution is available this time, we compared the ten and one hundred packages per Δt runs, with the highest time resolution run. For this test $N_p = 10^8$ packages have been used. The results are shown

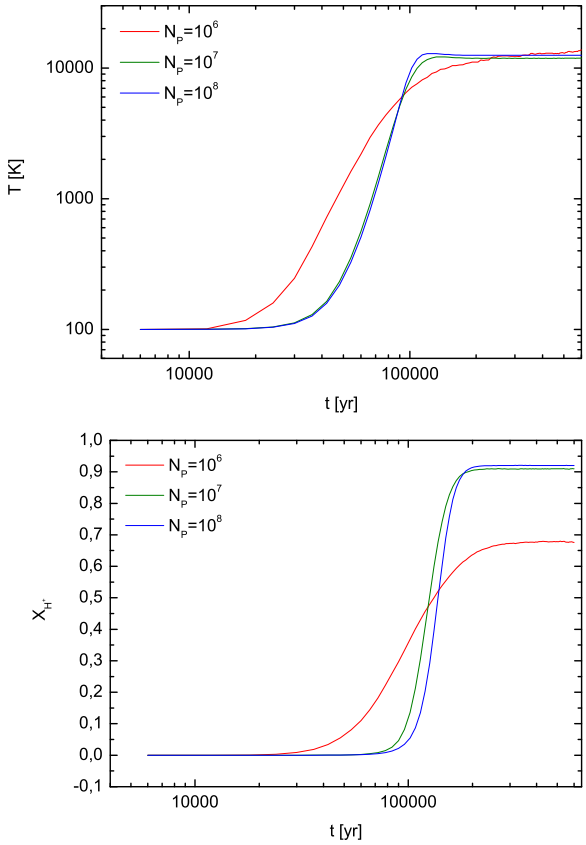

Figure 4.2.3: Mean evolution of all cells at $d = 40\mathrm{pc}$ distance to the source. The temperature (top) and ionisation fraction evolution is show. The clear jump in the ionisation fraction shows, that CRASH is able to reproduce the sharpness of the jump well.

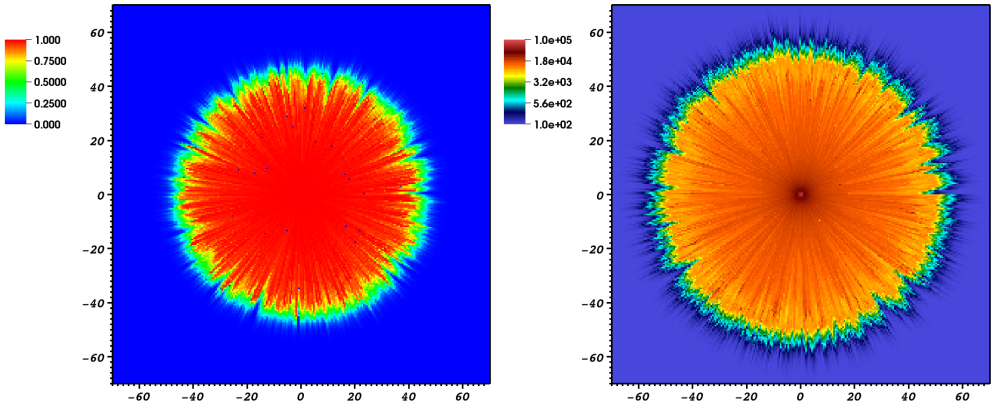

Figure 4.2.4: Visualisation of the central plane of a realistic Strömgren sphere. Shown are the hydrogen ionisation fraction (left) and temperature (right) of the HII region. This is the $N_p = 10^8$ run. The spatial axis are in parsec scale. The bad Monte-Carlo sampling due to limitations in sampling the source spectrum are clearly seen.

in Figure 4.2.5.

Deviations occur way beyond the position of the ionisation front at around 50 pc. This indicates, that scattering photons are penetrating into neutral regions. These diffuse photons stem from the ionisation front itself, which is consistent with results by Ritzerveld (2005). We thus conclude, that time resolution only has a bigger impact on the diffuse component. The error introduced with this scheme are about 0.5% in temperature and almost 1% in ionisation fraction for the lowest resolution run.

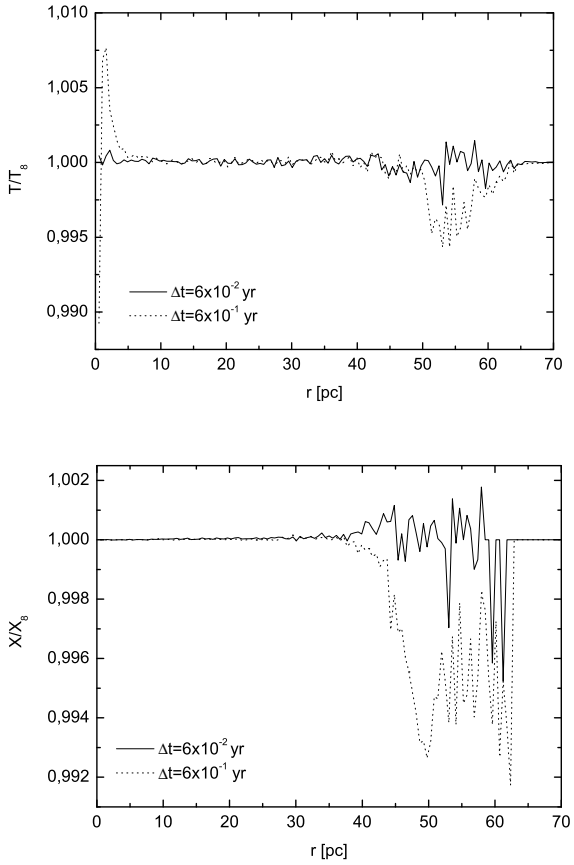

Figure 4.2.5: Effects of the time resolution on the final temperature and ionisation fraction results. Two different time resolutions are compared to the highest resolution run $\Delta t = 6 \times 10^{-3}\mathrm{yr}$. The position of the ionisation front is at about 50 pc, but deviations are visible beyond this, which is due to scattering photons.

4.2.3 Background Photon Test

To test our implementation of background photons, we developed a special test case. As has been seen in Chapter 2.3, we found an analytic formulation to the evolution of the ionisation fraction in one cell. The solution is given in

Equation (2.3.3). We will use this for testing our implementation.

Equation (2.3.1) is only valid, if the whole cell is drenched in photons, i.e. if they are not attenuated by the medium in the cell, but still ionise it. We modified ACRASH accordingly for this test by keeping the number of photons in a package constant while it propagates through the box.

The idea behind this test is, that we use a box with length $L_{box} = 5\mathrm{pc}$ and use different spatial resolutions, to see, whether this has any effect on the result. A possible source of such an effect is the formulation of the energy content in a package or how much energy is deposited in a cell. With this, we have discovered a problem with the CRASH scheme described in Section 3.4.1.2.

The test is carried out at redshift $z = 2$ for three different overdensities $\delta = 100, 0, -0.5$ in a neutral homogenic medium. The spatial resolution is varied to contain $N_c = 1, 4, 16, 32, 64$ cells. A number of $N_p = 10^6$ photon packages are used.

To obtain comparable quantities, we calculated the mean ionisation fraction in the box to compare with the analytic result, which is valid for one cell only. With this we pretend that the whole box behaves like one cell. The results are shown in Figure 4.2.6.

In the test runs for $\delta = 0$ and $\delta = -0.5$ ACRASH is able to reproduce the analytic solution for any number of box divisions. This was only achievable, after the mean crossing length parameter f_l was set to $f_l = 1.0$, which is the only correct value for our treatment of background photons.

For the $\delta = 100$ test, our result deviates from the analytical solution. The analytic solution does not include collisional ionisation, which is important at high densities. We attribute the difference of ACRASH to the analytical solution to exactly this effect.

As can be seen, our implementation of background photons is robust and valid. We ensure a homogenic sampling without the need of calibration factors as is the case in the implementation described in Maselli and Ferrara (2005).

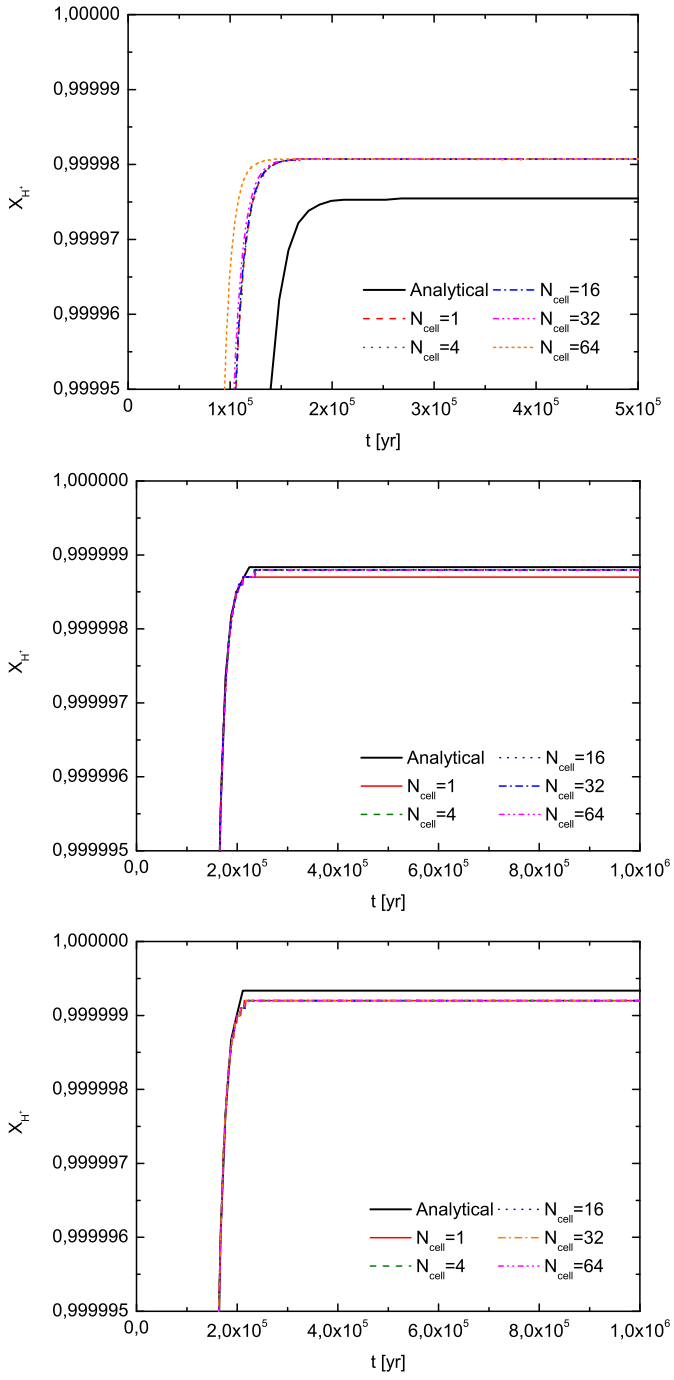

Figure 4.2.6: Mean time evolution of our box at different spatial resolution for different overdensities $\delta = 100$ top panel, $\delta = 0$ middle panel, and $\delta = -0.5$ for the lower panel. The thick black line gives the analytical result.

5 Radiative Transfer Effects on the Ly-α Forest

With ACRASH, we can study radiative transfer effects on the Ly-α forest and compare the results with the Gnedin model. By mapping our dark matter simulations to hydrogen density fields using methods described in Chapter 2, it is possible to apply a background radation field in ACRASH. With this we obtain proper ionisation fractions which can be used for synthesising Ly-α forest spectra. The temperature field is determined using the effective equation of state (equation 2.2.2) and is kept constant throughout our calculations.

Different effects not included in the Gnedin model could influence the Ly-α forest. These are shadowing effects and diffuse recombination radiation emitted by hydrogen. Using ACRASH it is now possible to check any influence of all these effects.

Unfortunately we cannot solve the whole 50 Mpc density field, due to restriced computational power that was available. ACRASH is not properly parallised for this task. For this an MPI version needs to be created. We therefore restrict our analysis to a 25 Mpc subbox, which might bias our final statistical analysis of the box. This needs to be kept in mind, when comparing our results with the ones optained through the Gnedin model.

But before applying ACRASH to the cosmological box, we want to create a controlled experiment, to see how the Ly-α spectrum is influenced by all these different effects.

5.1 Numerical Experiment

In order to understand effects on the spectra more clearly, a numerical experiment is conducted. By setting up a simulation box with two thin sheets resembling two filaments, we can check our method and look for possible deviations to the Gnedin model. These two filaments were chosen and placed in such a way, that the resulting absorption profiles do not blend.

We took a 12.5 Mpc box using $N_c^3 = 100^3$ cells and filled the box completely with hydrogen at the mean density $\delta = 0$. Embedded in this homogeneous medium are two dense layers. They lie parallel to each other and are separated by 57 cells. One of the layers is 2 cells thick and has an overdensity of $\delta = 50$, the other is only 1 cell thick with an overdensity of $\delta = 10$. The experiment setup is sketched in Figure 5.1.1.

Hydrogen densities are then calculated from the overdensities by using Equation (2.1.11). The temperature field is generated using the effective equation of state with its parameters given in our models in Table 2.1. We then propagate

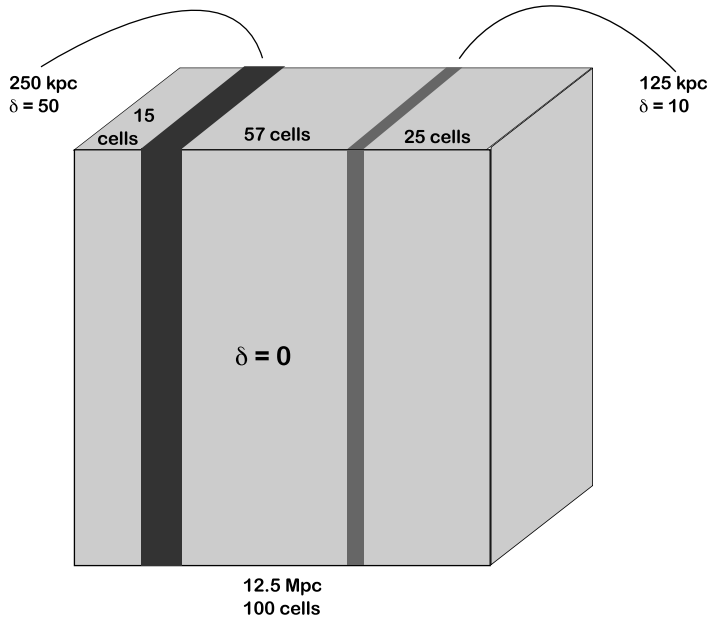

Figure 5.1.1: Detailed sketch of our numerical experiment setup.

a UV background field with ACRASH. The field is parametrised with the values given in the afore mentioned table.

The simulation is run for $t_s = 2.5 \times 10^8$ yrs using $N_p = 4 \times 10^8$ photons and $N_t = 2 \times 10^7$ time steps. Since numerical noise is always present in Monte-Carlo simulations, we average the resulting ionisation fractions over many outputs at different times of the simulation. Care has been taken, that only snapshots where an equilibrium solution has been reached have been used for averaging. The rate equations used by ACRASH were changed to the ones included in the Gnedin model (see Hui and Gnedin (1997)).

The ionisation fraction output of the simulation was then entered into the Gnedin model, replacing its formulation of the ionisation fractions. From these outputs artificial spectra were created. These are compared to spectra derived with the Gnedin model using its simple analytic formulation for the ionisation fractions.

Results for redshifts $z = 1.0, 3.0, 4.0$ are shown in Figure 5.1.2. It can be clearly seen, that our code reproduces the Gnedin model correctly. Variations in the density field at different times due to the Monte-Carlo method are around 0.025 in transmission (the gray area in the plots). Our results show no deviations from the Gnedin model at redshifts $z = 1.0$ and $z = 3.0$.

For redshift $z = 4.0$ transfer effects can be identified. If we assume, that the mean solution is converging to the correct solution and if we pay no attention to the Monte-Carlo error, we see an increase in transmission around the high density peak absorption line. This is due to recombination radiation. The filament in itself is emitting photons and increases the ionisation fraction in its surrounding slightly.

To emphasize this finding, control calculations without scattering have been

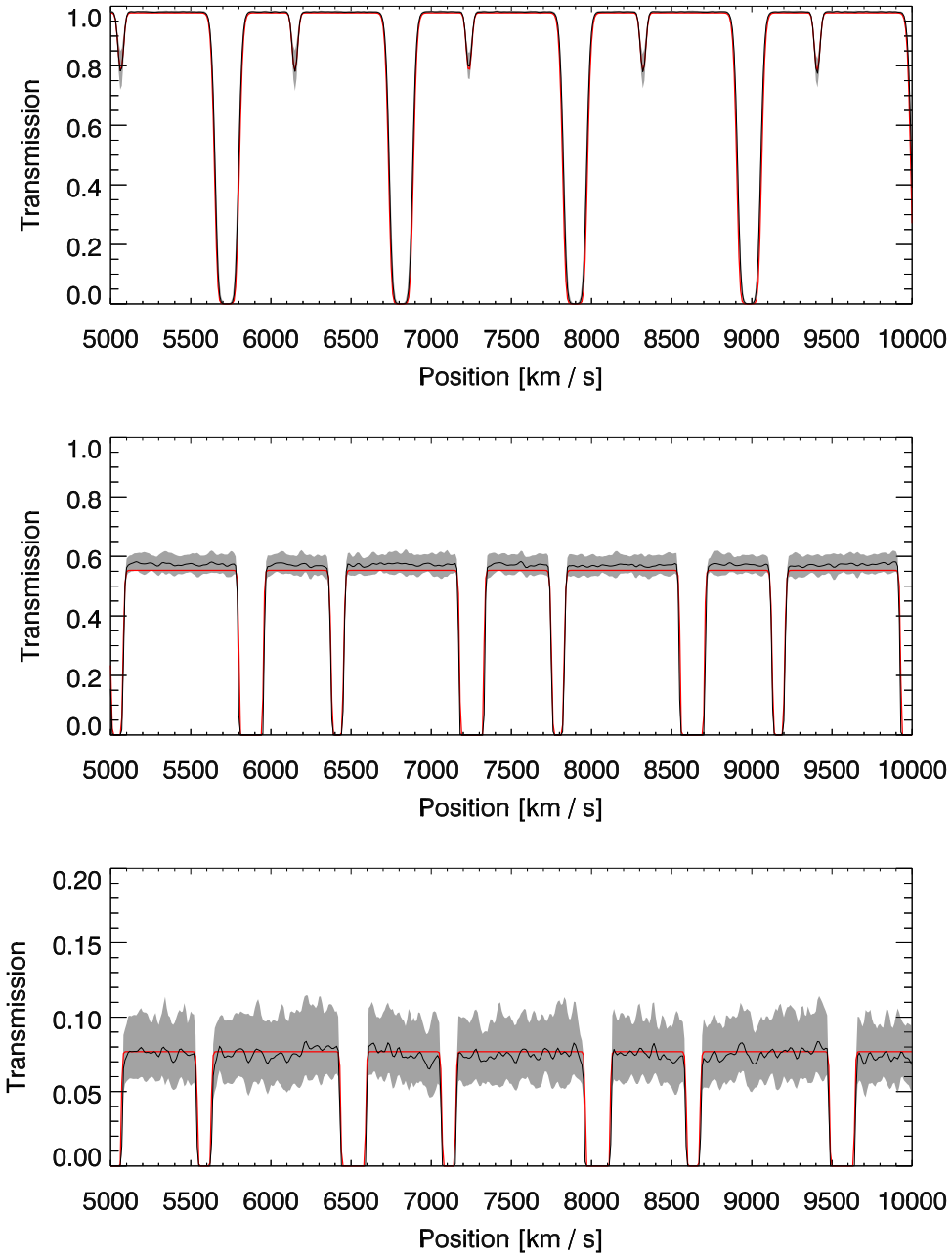

Figure 5.1.2: Results of the numerical experiment. Comparing spectras derived using the original Gnedin model (red line) with spectras using ionisation fraction fields derived with ACRASH (black line). The gray area around the ACRASH solution gives one sigma variations due to Monte-Carlo method. Top panel is for redshift $z = 1$, middle panel for $z = 3$, and lower panel for $z = 4$.

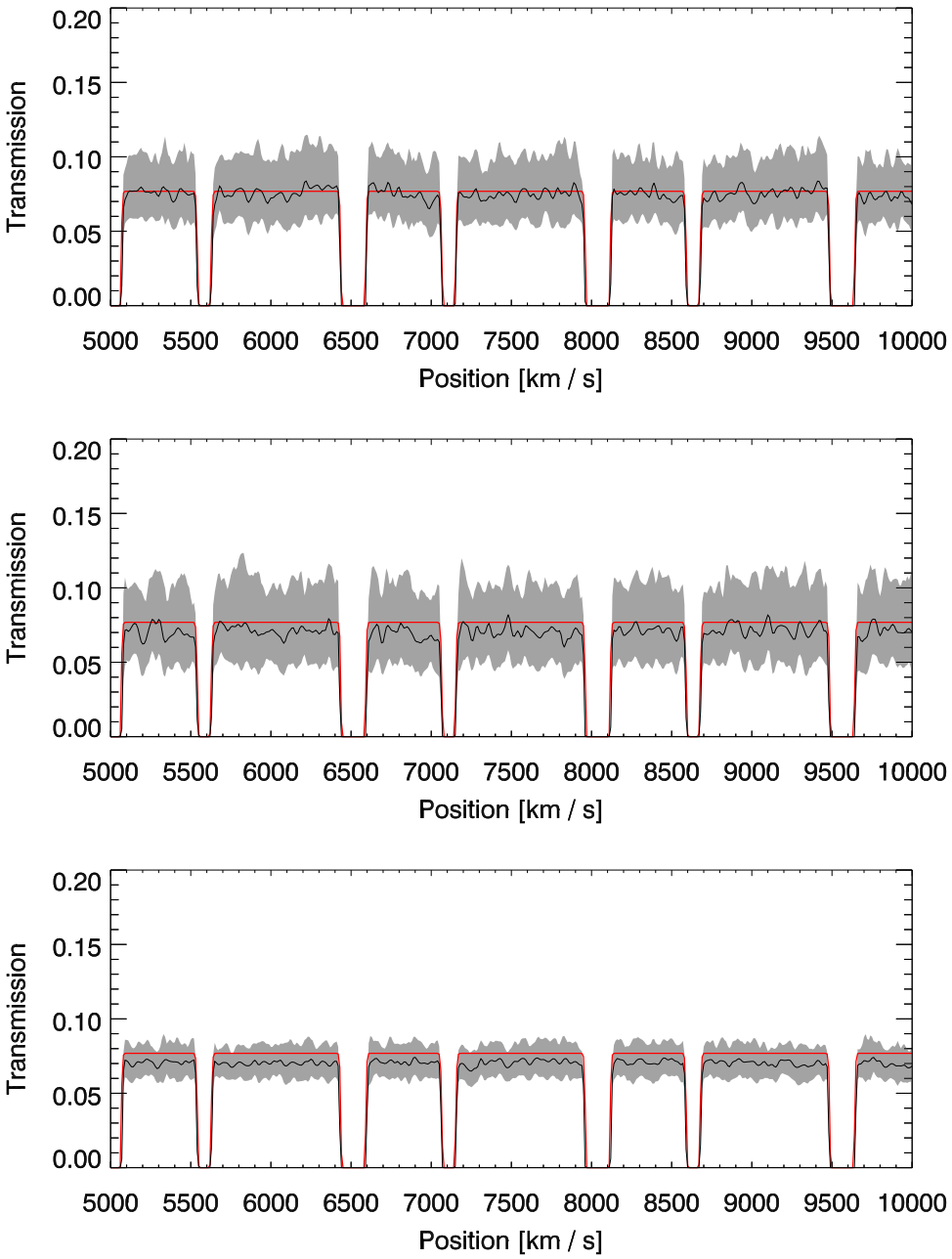

Figure 5.1.3: Effects of recombination radiation on the spectrum at redshift $z = 4.0$. The top panel gives the results including recombination, the panel below without. A clear increase in transmission can be seen around the big absorption line. The bottom panel gives a high resolution run with $N_p = 2 \times 10^9$ photons. The Monte-Carlo variance is greatly reduced, but the mean result does not change greatly, compared to the low resolution run.

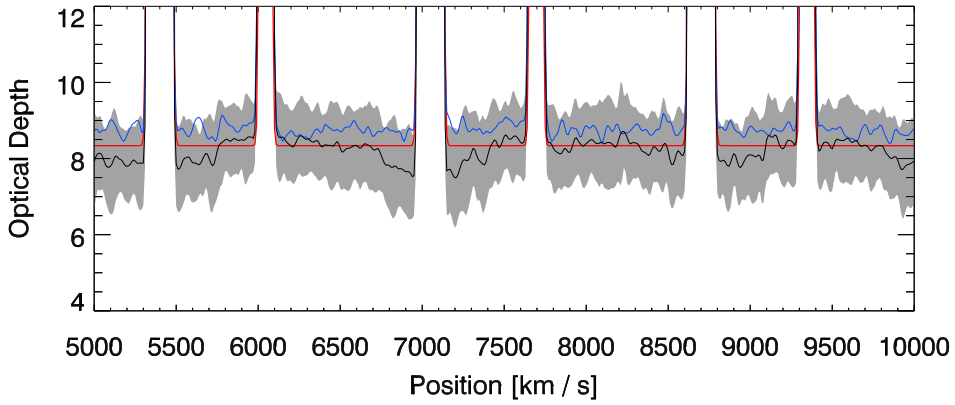

Figure 5.1.4: Optical depths of our numerical experiment at redshift $z = 4.9$. Red gives the original Gnedin model, blue our solution without the diffuse component, and black with the component. The gray area gives variations in the Monte-Carlo solution at different time steps.

carried out. We also used a higher photon resolution to verify our claim, that the mean solution converges to the actual one. In order to increase the photon number, we had to switch to the original CRASH scheme, where photons are propagated at an infinite speed of light. This was necessary, because memory limitations were reached quite fast with higher numbers of photons. Since we are only interested in the equilibrium solution, the choice of the speed of light makes no difference, as is seen in Figure 5.1.3.

By comparing results including and excluding recombination radiation, its effects are clearly seen. The denser filament affects its surroundings more than the other. This is easily understood, since in a denser ionised medium, more ionic cores will capture electrons. Therefore dense filaments radiate more diffuse light.

One can now argue, that all these effects are a lot smaller than the actual errors due to the simulation. We therefore compare the solution excluding the diffuse component with a high resolution run using $N_p = 2 \times 10^9$ photons. The higher resolution run confirms the mean solution of the low resolution run quite well. The result does not differ greatly. Only noise in the mean solution is reduced a little. Variations due to the Monte-Carlo nature of the simulations are also lower with higher resolution. We therefore conclude, that the mean solution of the low resolution run can be trusted well below the error bars and only noise in the mean result should be used as an estimate for the error of the solution.

The amount of influence by the diffuse component increases with redshift. At higher redshift, the medium is denser and recombines more easily. Since at redshift $z = 4.9$ we cannot plot transmission anymore (everything is saturated), we discuss our results in terms of optical depth. Again we compare our results with and without the diffuse component. Again we can confirm the influence of

the diffuse component around the high density filament, as is clearly seen in Figure 5.1.4. The diffuse component reduces the optical depth from 9 to 8.

Concluding we can say, that effects due to the diffuse component can be seen in our simple experiment. The influence starts to be noticeable at redshifts higher than $z = 4.0$. How greatly the diffuse component affects the Ly-α forest will be discussed below. In this simple test we could not identify any shadowing effects.

5.2 Real Box

To see if radiative transfer effects are visible in the Ly-α forest and how these affect the Ly-α statistics, the Gnedin model is compared with a full radiative transfer calculation using ACRASH. To do this, the same dark matter densities as in Chapter 2 were mapped to gas and temperature fields. This is done identically as in the toy model.

The Gnedin model does not contain radiative transfer effects. They will have an impact on the resulting spectra. For example shadowing effects increases optical depths around high density regions by shielding from UV background flux. Remember that a certain threshold is assumed, below which the UV background is considered to dominate the medium (it is not shielded). This is the place where background photons are produced in ACRASH. All areas with higher densities than the threshold will cast shadows. A threshold of $\delta_{BG} = 1$ was used.

Recombination radiation also has an impact near high density regions. Recombination events are more probable there and lead to lower optical depths around regions with high recombination rates.

In order to run our simulation, the original box size of 50 Mpc had to be reduced, because the resulting calculation times would have been too high for a detailed study. A sub box of 25 Mpc was used. To study possible effects introduced by this reduction, a comparison run with the complete box and similar resolution as the small one was carried out for redshift $z = 4$. This box took two weeks to reach the equilibrium solution on four CPUs.

For the small box $N_p = 2 \times 10^9$ photon packages have been sampled using $N_t = 1 \times 10^7$ time steps over $t_s = 2.5 \times 10^8\,\mathrm{yrs}$. The original CRASH formulation for recombination scattering has been used with $f_r = 0.01$. We solved the radiative transfer for redshifts $z = 3, 4, 4.9$ with and without recombination radiation. Parameters for the UV background flux and the effective equation of state can be found in Table 2.1. The rate equations given in Hui and Gnedin (1997) have been used for all runs.

As above to minimize Monte-Carlo variance in the equilibrium solution, an average of different snapshots having reached the equilibrium solution were used. With this, one sigma Monte-Carlo variances were derived using a Poisson distribution and are shown as gray areas in all the plots below, as in all the plots of the toy model.

All the statistical quantities discussed below, are obtained in the same fashion as in Chapter 2.5 by averaging over one hundred different lines of sights.

5.2.1 Transfer Effects on the Spectra

Analogue to the toy model, mock spectra (black lines in Figure 5.2.1 and 5.2.2) have been derived from the ionisation fraction fields. They are compared to the Gnedin model (red). In Figure 5.2.1 small sections of spectras from the redshift $z = 4$ simulation are shown. The upper plot gives results for the run including a diffuse component, the lower for the one without. In Figure 5.2.2 we plotted a sample from the redshift $z = 4.9$ run.

First of all, we can confirm the Gnedin model with ACRASH. We can reproduce the overall shape of the model spectra. Deviations are present and by looking at the lower panel of Figure 5.2.1 and 5.2.2, the effect of shadowing can be clearly seen. These spectras were calculated without the diffuse component. Deviations therefore can only stem from shadows.

This effect should manifest itself more next to high density regions and indeed this is the case in our mock spectra. In Figure 5.2.1 some examples for shadowing can be found at $1.755 \times 10^4\,\mathrm{km/s}$ or $1.70 \times 10^4\,\mathrm{km/s}$. These effects show up as differences between the prediction of the Gnedin model and the radiation transfer solution independent of scattering effects (i.e. in the upper and lower panel of Figure 5.2.1). In the direct vicinity of these lines are saturated lines, which indicate the presence of higher density regions.

In the $z = 4.9$ case shadowing should be more prominent due to the higher densities involved and indeed this is the case in Figure 5.2.2. At $1.15 \times 10^4\,\mathrm{km/s}$ shadowing affects this region. Again, it is right besides a high density region.

By just looking at the mock spectra, we can conclude that shadowing influences the ionisation state of the medium around high density regions. How this will influence statistical properties, is discussed later.

The second transfer effect studied is the influence of a diffuse component. The impact of this component is small as compared to shadowing. But still it is noticeable by comparing the full transfer mock spectras (black lines) including the diffuse component (upper panels) with the ones lacking it (lower panels). At redshift $z = 4$ we identify three areas where the effect is visible. These would be at $1.605 \times 10^4\,\mathrm{km/s}$, $1.63 - 1.67 \times 10^4\,\mathrm{km/s}$, and $1.83 - 1.85 \times 10^4\,\mathrm{km/s}$ in Figure 5.2.1 (upper panel). The differences are slight but can be best seen at places, where in the lower panel the spectra does not match the Gnedin model, but in the upper it does.

It would be expected, that a diffuse component is more prominent around high density regions. There the probability for electrons to recombine is higher and more diffuse photons are produced. This can be confirmed in the mock spectra. For example the differences at $1.83 - 1.85 \times 10^4\,\mathrm{km/s}$ are right next to a saturated line.

In the redshift $z = 4.9$ case we expect the diffuse component to have a greater effect, again due to the higher densities involved. By simply looking at the mock spectra in Figure 5.2.2 we again identify three regions in the spectra where the effect is observable. It manifests itself at $1.025 \times 10^4\,\mathrm{km/s}$, $1.11 \times 10^4\,\mathrm{km/s}$, and at $1.29 \times 10^4\,\mathrm{km/s}$. Again the differences to the no diffuse component run are quite small. As before, they are located around high density regions.

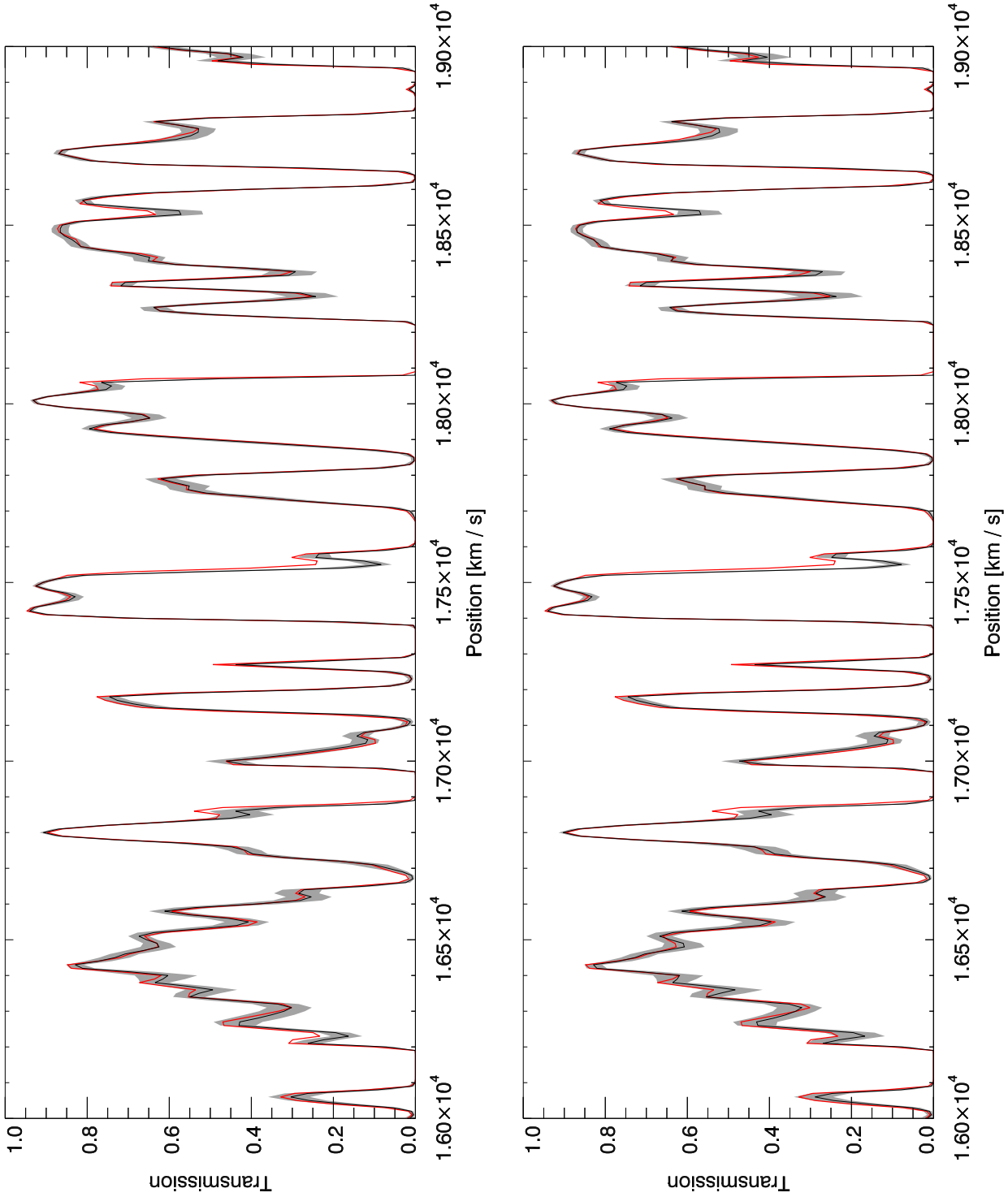

Figure 5.2.1: Spectra of one sample line of sight at redshift $z = 4$. Spectras derived with ACRASH (black line) and the Gnedin model (red line) are compared. The gray area gives the variation due to the Monte-Carlo method. Top panel includes diffuse radiation, the lower one is without it.

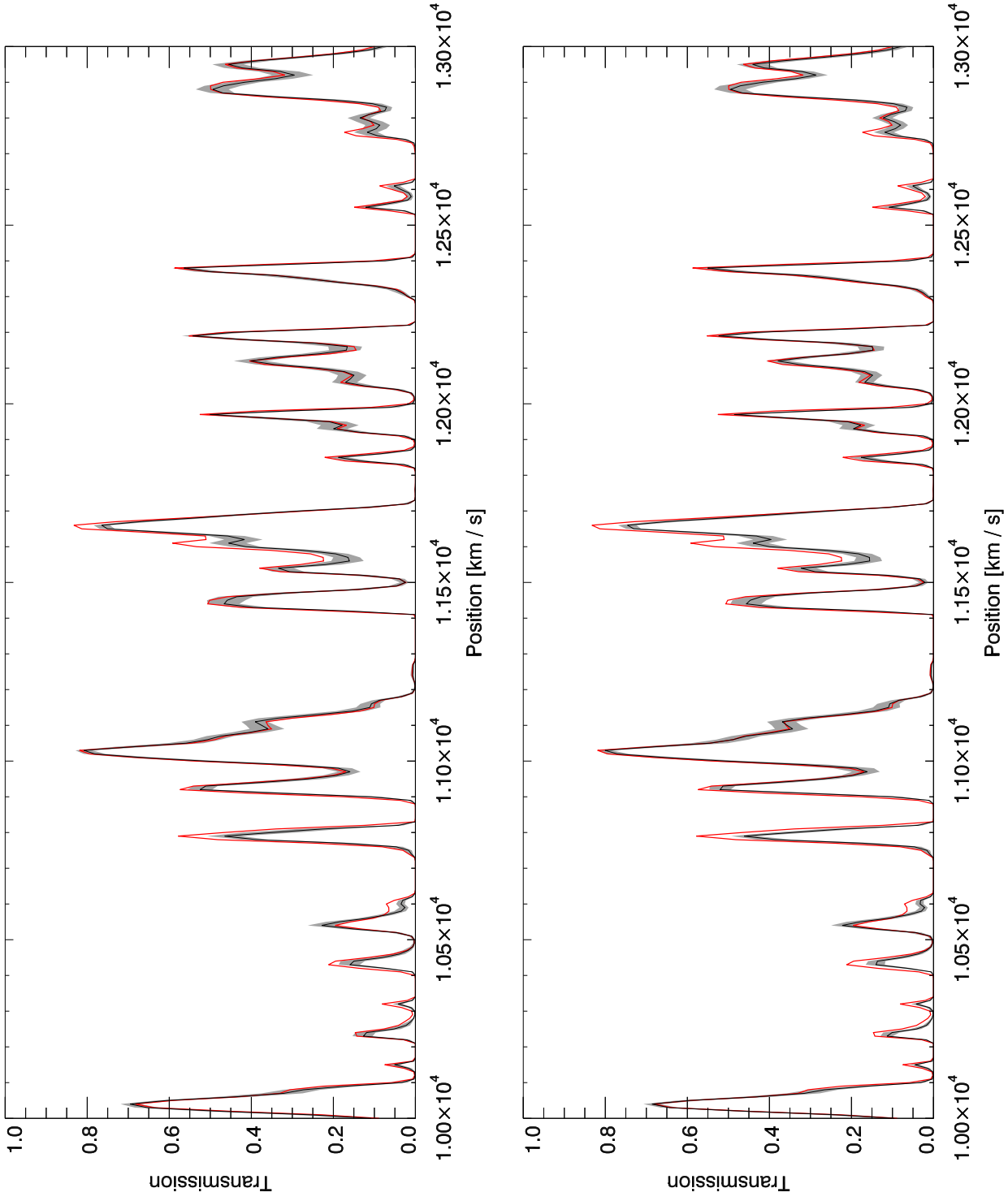

Figure 5.2.2: Spectra of one sample line of sight at redshift $z = 4.9$. Spectras derived with ACRASH (black line) and the Gnedin model (red line) are compared. The gray area gives the variation due to the Monte-Carlo method. Top panel includes diffuse radiation, the lower one is without it.

By analysing mock spectra and comparing them with spectra obtained through the Gnedin model we can identify radiative transfer effects. The biggest influence has shadowing. A diffuse component arising from recombination events only has a marginal effect on the spectra. All these effects are higher around more saturated and therefore denser regions, as predicted.

5.2.2 Mean Effective Opacities

We want to proceed with our analysis similar to Chapter 2.5. We begin by computing the simplest statistical property of the Ly-α forest, the mean effective optical depth τ_{eff}. In Figure 5.2.3 the mean effective opacities are given for our three runs (black stars), comparing them to the results of the Gnedin models (gray stars) and observational data by Schaye et al. (2003).

Overall we can replicate the values deduced with the Gnedin model. In general, the ACRASH models are a bit optically thicker than the Gnedin model. This is mainly due to shadowing effects, but the influence is quite small. In order to completely reproduce the observational data with our models, a small increase in the UV background flux J_{HI} would be necessary. But it should be noted that the UV background is independently restricted by the proximity effect and the QSO luminosity function. Only within our model it is a free parameter.

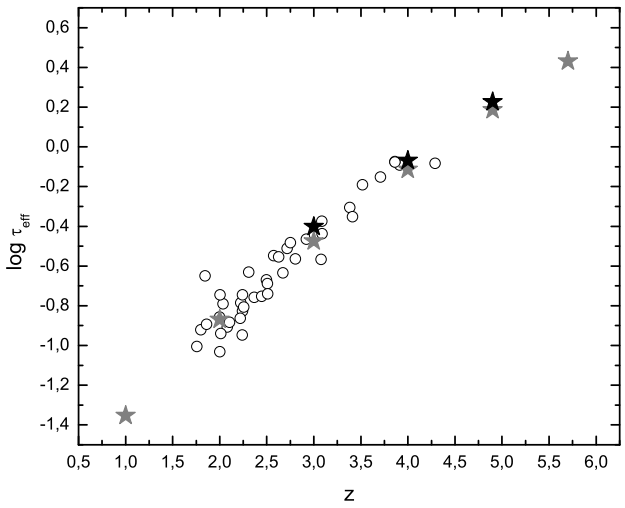

Figure 5.2.3: The effective optical depth of the Gnedin models (gray stars) compared to the ones derived with ACRASH. Open circles represent measurements by Schaye et al. (2003).

5.2.3 Probability Distribution Function

We now want to turn our attention to the transmission probability distribution function PDF. We compare the PDF at redshift $z = 3, 4, 4.9$ with observational data and the PDF obtained with the Gnedin models. The results can be seen in Figures 5.2.4 and 5.2.5. PDFs including a diffuse component (green lines) and models excluding it (red line) are set side by side where available.

At redshift $z = 3$ the PDF matches the Gnedin data in the low transmission part. This can be seen in Figure 5.2.4 upper panel. The results are identical up to a transmission value of 0.45. Then the PDF of the radiative transfer solution starts to deviate slightly. It seems, that low density regions are optically thicker than in the Gnedin model. The differences to the observational data in the high opacity part are similar to the Gnedin model. In the low opacity part, our solution lies slightly above the observed data. This corresponds to the small increase in the mean effective optical depth stemming from redistribution of the total transmission to higher opacities.

The mean optical depth is slightly bigger in the ACRASH solution. This results in a redistribution of the PDF at the low opacity end. The number of completely ionised regions is smaller compared to the Gnedin model, which is seen slightly below one hundred percent transmission. Shadowing effects are probably responsible for the small difference.

Variations from the reference model in our result start to increase with higher redshift. At redshift $z = 4$ (see Figure 5.2.5 lower panel) the results start to differ stronger in the opaque region. At high opacities our model seems to match very well. The ACRASH solution is more or less straight on the observed PDF. But at around 0.8 deviations start to increase. We cannot be sure, if we do not introduce errors in our results due to sampling only a smaller simulation box. This will be discussed later in our analysis.

Scattering processes only play a minor role at redshift $z = 4$ if the results with (green line) and without it (red line) are compared. In principle the two results are identical.

At redshift $z = 4.9$ the gap between the full transfer solution and the Gnedin model is about the same as before. Strikingly in the higher opacity region, the radiative transfer solution is very good at reproducing the Gnedin model. We get a perfect match, but at a transmission level of about 0.4, our PDF starts to deviate from the reference. The differences are quite small, but still big enough to smooth out the 'S'-form that is present in the Gnedin model. The overall shape of our PDF matches better the observational data and the gap between the two could be removed with a higher background. Again the differences should be due to shadowing effects. The steep rise of our solution at the right hand side of the PDF is probably introduced by only sampling a smaller box.

At this redshift, the solution including a diffuse component is slightly different at some parts to the solution without it. It seems, that the low density regions are more sensible to recombination radiation than at lower redshift. This is a little bit surprising, since in the direct comparison of mock spectras, the effect was not that eminent.

Concluding we can say, that our models reproduce the Gnedin model well. Some small radiative transfer effects can be identified in the PDF which we identify as shadowing effects. We come to this conclusion through the analysis of our mock spectra, where the effects are better visible. To produce better matching models, the UV background flux J_{HI} needs to be slightly adjusted. Deviations at low opacities stem from numerical errors which we will demonstrate later. We now want to address possible objections to the picture presented above and critically discuss various effects (physical and numerical) that could influence our results.

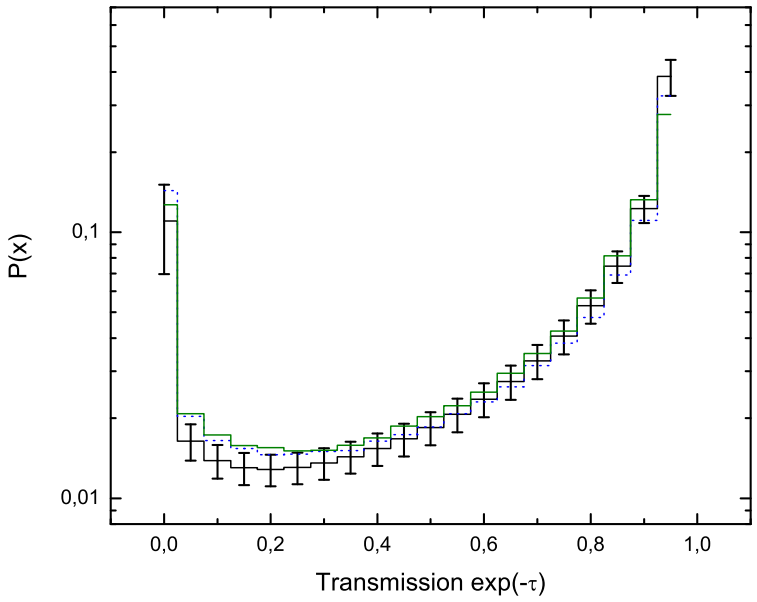

Figure 5.2.4: Probability distribution function at redshift $z = 3$. Compared are observations by Becker et al. (2006) (black line), the Gnedin model (blue dotted), and the ACRASH result with a diffuse component (green).

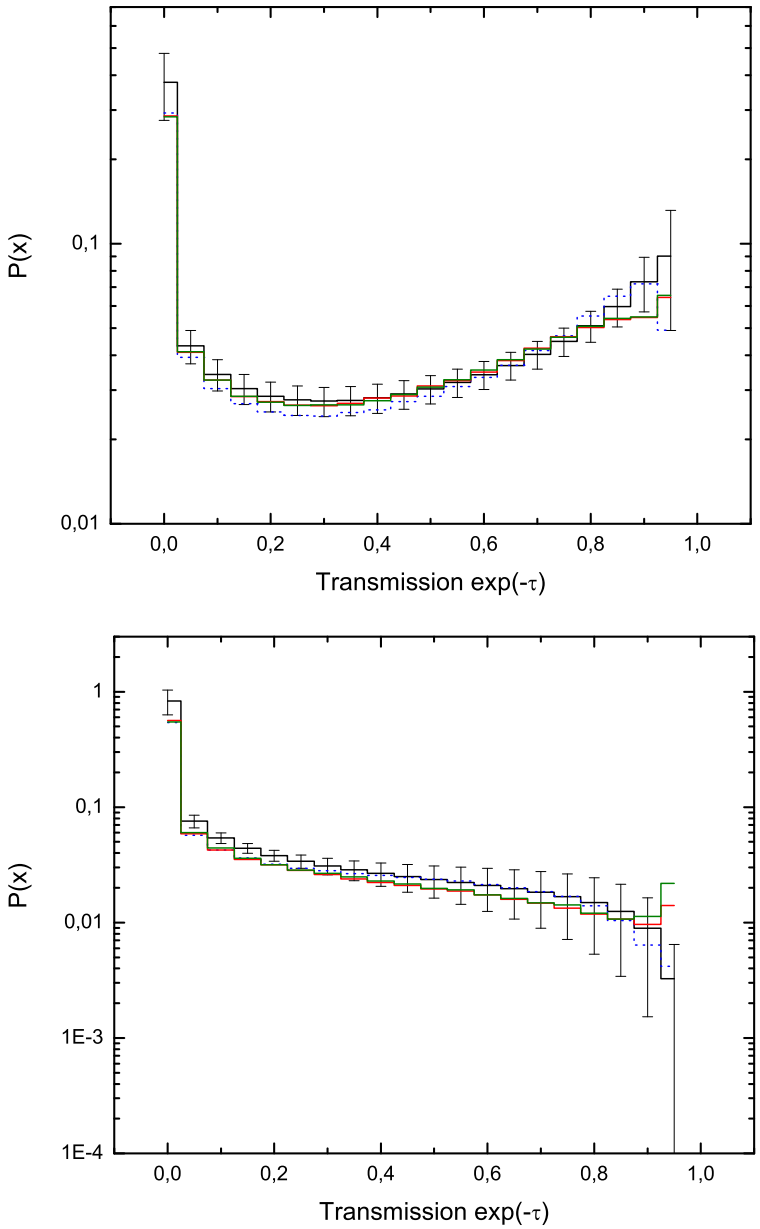

Figure 5.2.5: Probability distribution function at redshift $z = 4$ (upper) and $z = 4.9$ (lower panel). Compared are observations by Becker et al. (2006) (black line), the Gnedin model (blue dotted), and the two ACRASH solutions with (green) and without (red) a diffuse component.

5.2.3.1 Identifying Possible Methodical Problems

During our analysing process, we checked many different possible error sources to see, whether the differences in the PDF are physical or purely numerical. This section is organised as such, that we “play” a game of question and an-

swer for the redshift $z = 4$ run. This allows for a better representation of this error analysis.

It could be, that we do not sample low density regions sufficiently well. What happens with a higher sampling resolution? When increasing the number of photons from $N_p = 2.0 \times 10^9$ packages to $N_p = 1.0 \times 10^{10}$ packages, nothing changes. The shape of the resulting PDF stays the same and differences to the lower resolution runs are barely recognisable. This can be seen in Figure 5.2.6

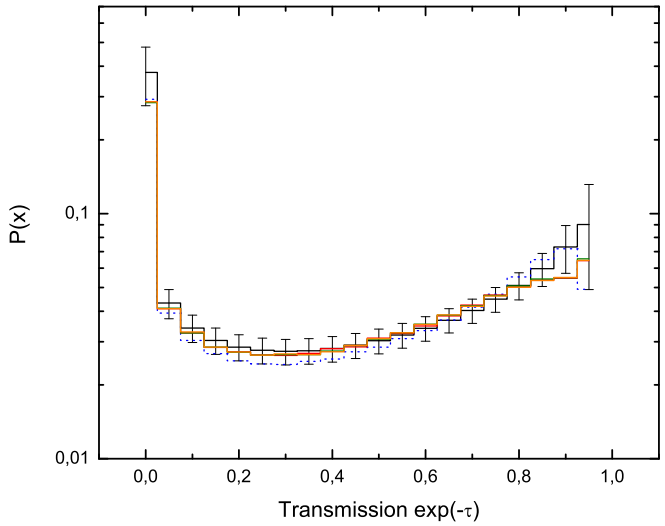

Figure 5.2.6: Probability distribution function at redshift $z = 4.0$. Comparison of our low resolution runs discussed above (green line, mostly below the orange line) with a high resolution run of $N_p = 1.0 \times 10^{10}$ photon packages (orange line).

Could the differences stem from undersampling the PDF? Since we are only sampling a 25 Mpc sub box of the whole box, it could be, that we are not sampling the box properly when determining the PDF. It is possible that the 25 Mpc sub box is not representative. To check this, we calculated the radiative transfer for the whole 50 Mpc box using $N_p = 1.0 \times 10^{10}$ photon packages at redshift $z = 4$. This corresponds more or less to the same sampling resolution as used in the 25 Mpc case.

Unfortunately ACRASH is not yet efficient enough to solve the transfer equation in a reasonable time. To reach a solution that is in equilibrium it took about two weeks on the 4 CPU shared memory cluster of the Astrophysical Institute in Potsdam. With this solution we calculated once more the PDF using one hundred line of sights (unfortunately we were not able to average the result over different snapshots in equilibrium). The result is seen in Figure 5.2.7.

The PDF of the small box suffers from incomplete sampling. This is best seen at the low opacity end of the PDF. The PDF starts to fall and does not keep on rising as in the 25 Mpc result. In the middle part of the PDF discrepancies are also present to the sub box result. It seems that the relative number of highly ionised regions is higher in the sub box than in the big run. It still needs to be studied in more detail, whether this is related to our implementation of the background radiation.

For this we want to see if we can identify visually, where this discrepancies might come from and if our implementation of the background radiation introduces any unwanted effects or not.

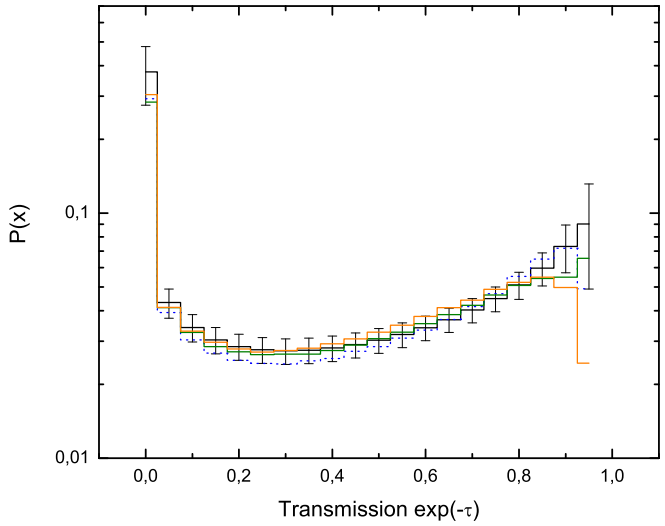

Figure 5.2.7: Probability distribution function at redshift $z = 4.0$ derived from the whole 50 Mpc simulation box (orange line) compared to the 25 Mpc result (green line).

Is there a visual difference in the ionization fraction fields? To clearly compare the Gnedin model with the result obtained using ACRASH, we visualised the ionisation fraction fields of both methods. This can be seen in Figure 5.2.8 for the 50 Mpc run at $z = 4$. The colour coding is exactly the same for both figures and by looking at the two plots, no striking differences can be seen.

By looking a little closer it can be observed, that the filaments of the ACRASH solution (bottom panel) are by about one cell bigger and that some small parts in high density regions are shielded.

In Figure 5.2.9 we plot the absolute differences of the two models to further understand, where our results deviate. In this plot, we are able to identify one of the possible problems. The differences could stem from shadowing effects which would lead to inhomogeneous UV background fluxes at different places in the box.

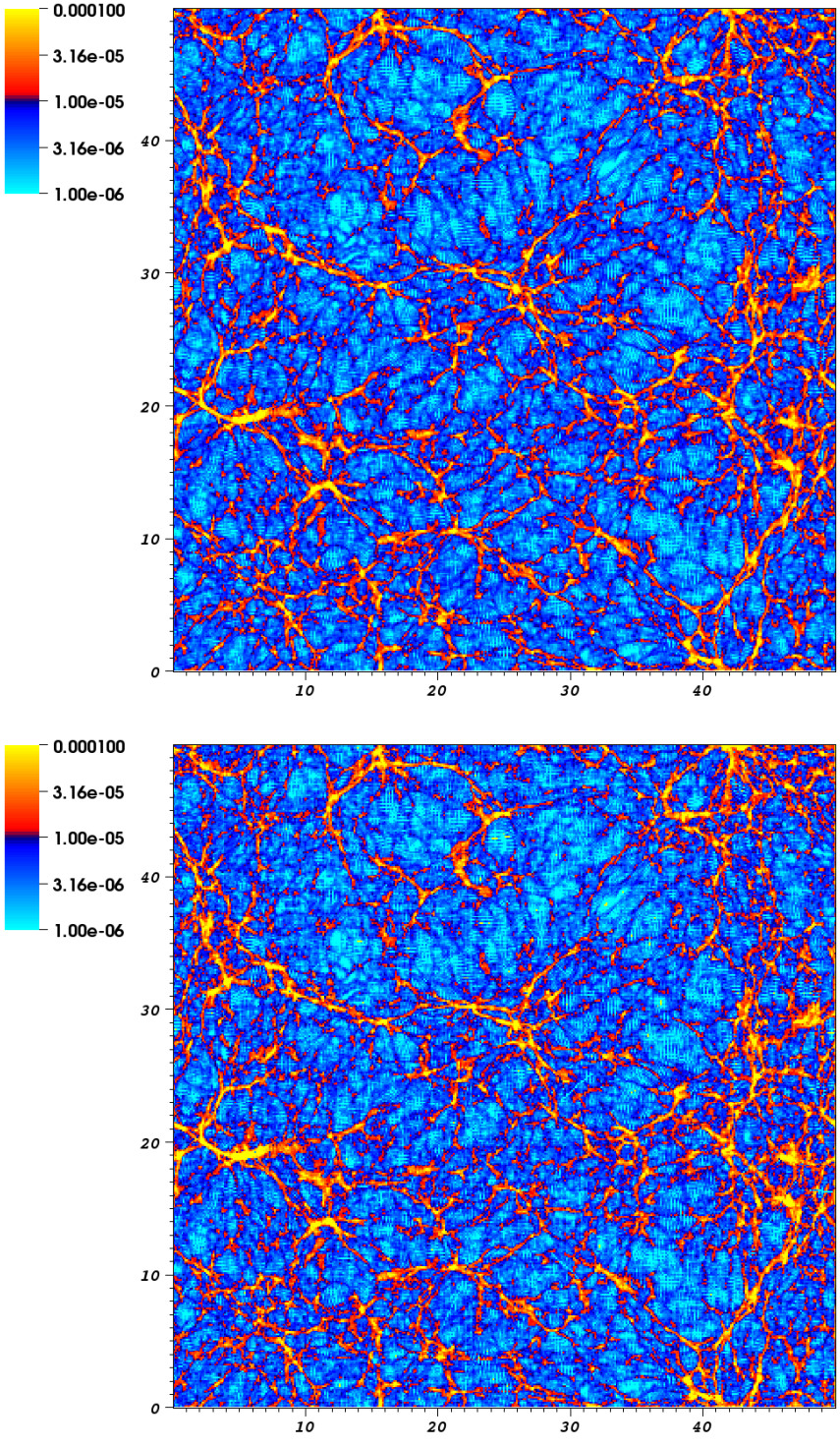

Figure 5.2.8: Visualisation and comparison of slices from our 50 Mpc run at $z = 4$ (lower panel) and the Gnedin model (upper panel). Shown is the neutral ionisation fraction logarithmically colour coded.

This can be clearly seen at the right side of the plot. There a very dense web of filaments is present and deviations from the Gnedin model in the voids seem to be bigger than in other voids. The dense filamentary structure is thus shielding UV background radiation.

We also identify a problem with our implementation of the background field. Since we are only propagating background photons parallel to the box faces, shadowing effects have a preferred direction. This needs to be addressed in future versions of our code.

To see how well our code performs compared to the Gnedin model, we show the relative differences $(X_{Gnedin} - X_{sim}) / X_{Gnedin}$ of the neutral fraction in Figure 5.2.10. With this it should be possible to determine the overall error of ACRASH and whether any real flux inhomogeneities exist. It can be seen, that the average deviation from the Gnedin model is around 10 to 20%. Then there are regions, where the errors are bigger (white colour). This has to be connected to the way the background field is implemented, since preferred directions are present.

There are certain strips in the plot (for example in the middle from top to bottom), where the difference is very small. But then there are strips, in which more white colour (and therefore bigger deviations) can be seen. Either this is a numerical issue with our background implementation or an indication for inhomogeneities in the UV background caused by shielding.

Another interesting feature in the plot are diagonal rays which stem from the diffuse component.

It is necessary to do further testing with our background implementation and to adjust the method by propagating rays in arbitrary directions. It is also interesting to see, how ACRASH could be improved to reduce the overall error.

From this we identify our discrepancies in the low density regions as stemming from a mixture of an inhomogeneous UV flux field and in the low opacity regions as numerical errors.

If some of the deviations are due to shadowing, the problem should lessen if attenuation of photon packages is turned off? To test our hypothesis, that shadowing is one of the responsible effects for the observed discrepancies, we turned off attenuation similar to all our tests of the background radiation implementation. The resulting PDF is found in Figure 5.2.11.

The change in the PDF is quite small and only noticeable in the opaque part of the PDF. A slight shift upward is visible right to the transmission value of 0.8 is seen. Shadowing effects only influence the overall properties of the PDF slightly. The main problem is thus the accuracy of the CRASH/ACRASH scheme.

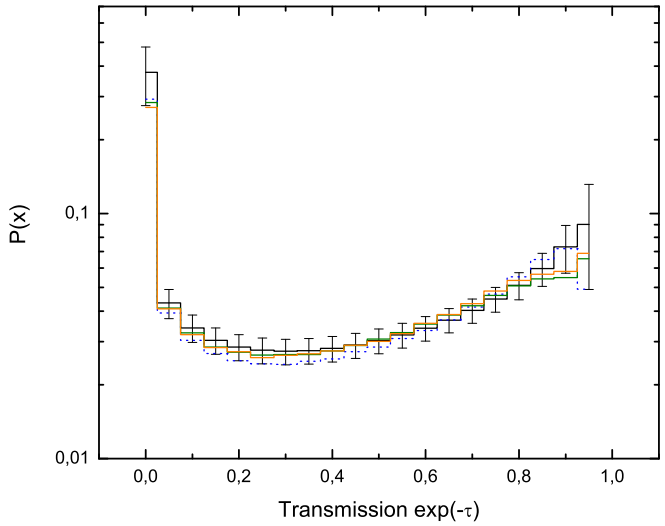

Figure 5.2.11: Probability distribution function at redshift $z = 4.0$. Comparison of the run without attenuation (orange line) with the original results.

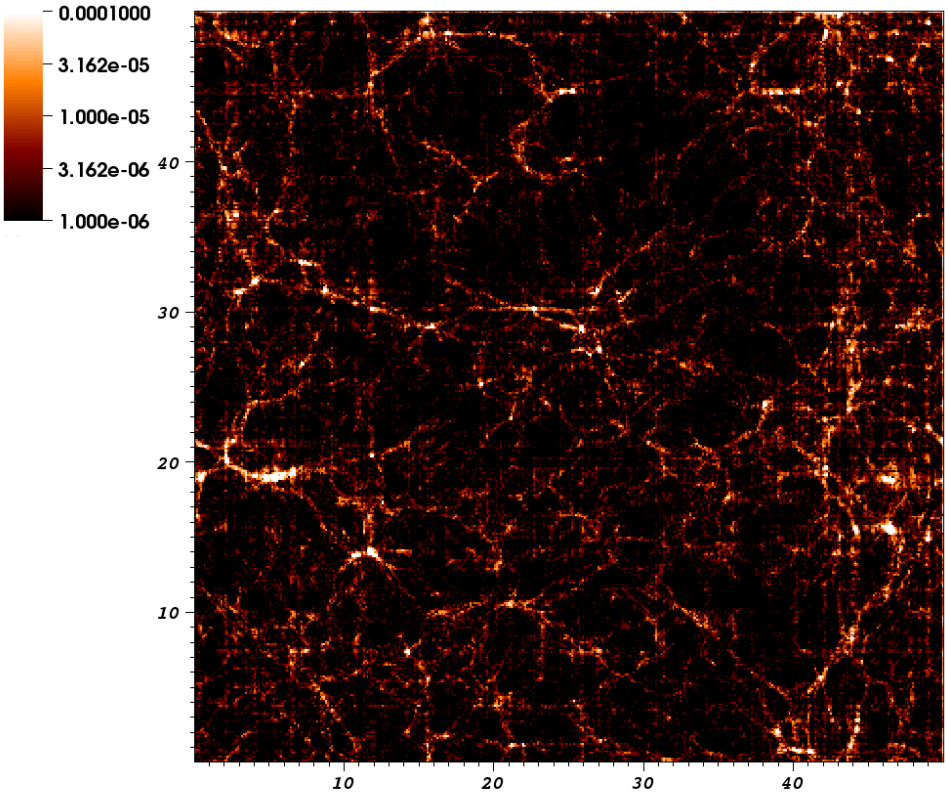

Figure 5.2.9: Visualisation of absolute deviations from the Gnedin model to the ACRASH solution. Color coding gives absolute errors $|X_{sim} - X_{Gnedin}|$ to the Gnedin model in a logarithmic scale.

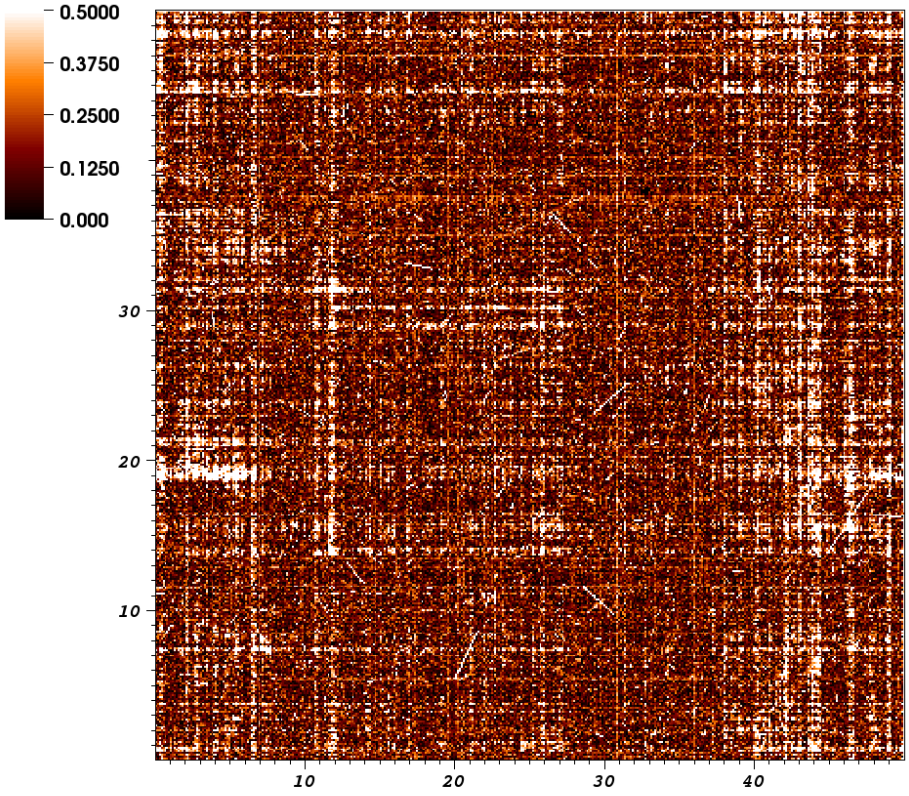

Figure 5.2.10: Visualisation of relative deviations from the Gnedin model to the ACRASH solution. Color coding gives relative errors $(X_{Gnedin} - X_{sim})/X_{Gnedin}$ of the ACRASH result in relation to the Gnedin model.

5.2.4 b-Parameter Distribution

The last statistical property studied is the b-parameter distribution. As in our discussion of our Gnedin models, we analysed the results obtained with ACRASH using our Voigt-profile fitter. The results are found in Figure 5.2.12. We compare both the ACRASH results (green lines) with the Gnedin results (red dotted lines) and see practically no difference.

This is not really surprising since the b-parameter is an indicator for the gas temperature. Since we did not alter the gas temperature due to photoheating, the line broadening should be identical as in the Gnedin case.

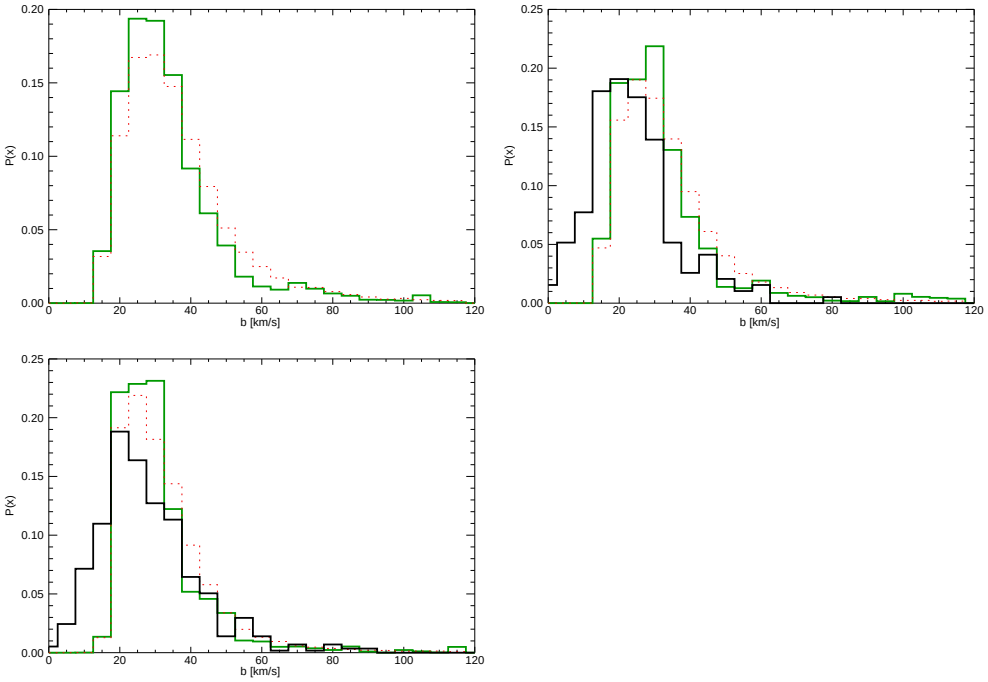

Figure 5.2.12: b-parameter distribution in our spectra using the Gnedin model (red dotted line) compared with results from ACRASH calculations (gree line). Where available, observational data by Kim et al. (2001) is shown (black line). Redshifts shown from left to right and top to bottom are: 4.9, 4.0, and 3.0.

6 Conclusions

In this thesis we wanted to reevaluate a simple analytical model of the Ly-α forest developed by Hui et al. (1997). As a first step model parameters for this analytical model were sought for our 50 Mpc dark matter simulations. These simulations used a WMAP3 cosmology.

Model parameters able of reproducing observational data were found for redshifts $z = 1, 2, 3, 4, 4.9, 5.7$ and are summarised in Table 2.1. We studied the analytical model extensively and analysed different physical effects influencing the results. The effects of an additional peculiar velocity field and a component resembling an additional temperature term (micro turbulence) were discussed.

To test the analytical Gnedin model, a general radiative transfer code was developed. We implemented our own version of the cosmological Monte-Carlo continuum transfer code CRASH by Maselli et al. (2003) . At the moment our version only incorporates hydrogen gas. An implementation for a background radiation field was developed and implemented into our version of CRASH. We named our code ACRASH. This implementation and the whole code as such was extensively tested.

To check the Gnedin model, we mapped our dark matter simulations to hydrogen gas densities and used the effective equation of state to derive the gas temperature. This is an identical setup as in the Gnedin model. We then solved the full transfer equation for an UV background field using ACRASH.

In general we can confirm the model by Hui et al. (1997) with radiative transfer. We expect several radiative transfer effects to be observable. These are shadowing effects and changes in the ionisation fraction due to electron recombination radiation. We identify shadowing to affect the Ly-α forest. The diffuse component only plays a minor role. Radiative transfer effects start to become important at a redshift of $z = 3$ and increase at higher redshifts.

Statistical properties of our models were studied and compared with properties of the Gnedin model. The ACRASH solution differs greatly at low opacities to the Gnedin model. We thoroughly analysed the differences and could identify two sources for the differences.

The first is the overall performance of the CRASH/ACRASH scheme. The mean deviation of our results from the Gnedin model lie at around 10 to 20%. This is a major problem if statistical properties of the Ly-α forest at low opacities are studied.

Another factor is that the UV background is not homogeneous in our simulations and is partly responsible for the deviations. These inhomogeneities stem from shadowing effects and are also intrinsic to our implementation of the background field. Our implementation does not seem to be perfect and different numerical effects arise. Whether and how these issues are responsible for the discrepancy needs to be studied in more detail.

We therefore cannot conclusively identify radiative transfer effects and quantify them. Problems with ACRASH's background flux implementation need to be definitively ruled out first and corrected if necessary. The question of accuracy of the scheme needs to be addressed and whether a higher sampling resolution could reduce the errors. An MPI parallelised version of the code would help with this task.

Also further comparison tests with other radiative transfer codes need to be realised. It is especially interesting to see, how other codes perform in the low density regime of the Ly-α forest.

Acknowledgment

First I want to thank the Astrophysical Institute in Potsdam for their hospitality and the permission to use the local supercomputing facilities. I also thank Dr. Volker Müller of the AIP for agreeing to co-supervise this work together with Prof. Gerhard Hensler. Volker showed unlimited patience with all my pesky questions and problems. I am also grateful to Gerhard for his support and for coordinating the cooperation between the University of Vienna and the AIP. I am very grateful for all your support, without this work would never have been possible.

I also want to thank numerous colleagues for helpful and insightful discussions, namely: Sander von Benda-Beckmann, Claudio Llinares, Dr. Tae-Sun Kim, and Steffen Knollmann.

Throughout the work I enjoyed travelling support from the AIP, OeGAA and ESO.

I thank Florian Herzele, Sander von Benda-Beckmann and Jaime Forero for reading parts of my manuscript.

This is also the place to thank the VAPOR team for giving their easy to use volume visualisation tool to the public. It has been extremely useful in the development and analysis of ACRASH. VAPOR can be downloaded at `http://www.vapor.ucar.edu` and is introduced in Clyne and Rast (2005) and Clyne et al. (2007).

I also appreciate any help by people I forgot to mention.

Bibliography

J. Amanatides and A. Woo. A fast voxel traversal algorithm for ray tracing. *Eurographics*, 1987.

S. Bajtlik, R. C. Duncan, and J. P. Ostriker. Quasar ionization of lyman-alpha clouds: The proximity effect, a probe of the ultraviolet background at high redshift. *Astrophysical Journal*, 327:570–583, 1988.

G. D. Becker, M. Rauch, and W. L. W. Sargent. The evolution of optical depth in the ly-alpha forest: Evidence against reionization at z 6. *astro-ph*, astro-ph/0607633, 2006.

S. Bianchi, S. Cristiani, and T.-S. Kim. The contribution of galaxies to the uv ionising background and the evolution of the lyman forest. *Astronomy & Astrophysics*, 376:1–9, 2001.

S. Brandt. *Datenanalyse*. BI-Wissenschaftsverlag, 1992.

R. Cen. A hydrodynamic approach to cosmology: Methodology. *The Astrophysical Journal*, 78:341–364, 1992.

J. Charlton, C. Churchill, and P. Murdin. Quasistellar objects: Intervening absorption lines. *Encyclopedia of Astronomy and Astrophysics*, November 2000. doi: $10.1888/0333750888/2366$.

A. R. Choudhuri. *The Physics of Fluids and Plasmas*. Cambridge University Press, 1998.

B. Ciardi, A. Ferrara, S. Marri, and G. Raimondo. Cosmological reionization around the first stars: Monte carlo radiative transfer. *Mon. Not. R. Astron. Soc.*, 324:381–388, 2001.

J. Clyne and M. Rast. A prototype discovery environment for analyzing and visualizing terascale turbulent fluid flow simulations. *Proceedings of Visualization and Data Analysis*, pages 284–294, 2005.

J. Clyne, P. Mininni, A. Norton, and M. Rast. Interactive desktop analysis of high resolution simulations: application to turbulent plume dynamics and current sheet formation. *New Journal of Physics*, 9:301, 2007.

L. L. Cowie, A. Songaila, T.-S. Kim, and E. M. Hu. The metallicity and internal structure of the lyman-alpha forest clouds. *The Astronomical Journal*, 109 (4):1522–1530, 1995.

R. Davé, L. Hernquist, D. H. Weinberg, and N. Katz. Voigt-profile analysis of the ly-alpha forest in a cold dark matter universe. *The Astrophysical Journal*, 477:21–26, March 1997.

M. A. de Avillez and D. Breitschwerdt. Global dynamical evolution of the ism in star forming galaxies. *Astronomy & Astrophysics*, 436:585–600, 2005.

M. A. Dopita and R. S. Sutherland. *Astrophysics of the Diffuse Universe*. Springer, 2003.

S. A. Dupree and S. K. Fraley. *A Monte Carlo Primer - A Practical Approach to Radiation Transport*. Kluwer Academic / Plenum Publishers, 2002.

G. J. Ferland, K. T. Korista, D. A. Verner, J. W. Ferguson, J. B. Kingdon, and E. M. Verner. Cloudy 90: Numerical simulation of plasmas and their spectra. *Astronomical Society of the Pacific*, 110:761–778, 1998.

T. T. García. Voigt profile fitting to quasar absorption lines: An analytic approximation to the voigt-hjerting function. *Mon. Not. R. Astron. Soc.*, 369: 2025–2035, 2006.

N. Y. Gnedin. Cosmological reionization by sellar sources. *Astrophysical Journal*, 535:530–554, 2000.

N. Y. Gnedin and T. Abel. Multi-dimensional cosmological radiative transfer with a variable eddington tensor formalism. *New Astronomy*, 6:437–455, 2001.

L. Hui and N. Y. Gnedin. Equation of state of the photoionized intergalactic medium. *Mon. Not. R. Astron. Soc.*, 292:27–42, 1997.

L. Hui, N. Y. Gnedin, and Y. Zhang. The statistics of density peaks and the column density distribution of the ly-alpha forest. *The Astrophysical Journal*, 486:599–622, September 1997.

D.G. Hummer. Total recombination and energy-loss coefficients for hydogenic ions at low density for 10 <= te/z2 <= 1e7 k. *Mon. Not. R. Astron. Soc.*, 268: 109–112, 1994.

I.T. Iliev, B. Ciardi, M.A. Alvarez, A. Maselli, A. Ferrara, N.Y. Gnedin, G. Mellema, T. Nakamoto, M.L. Norman, A.O. Razoumov, E.-J. Rijkhorst, J. Ritzerveld, P.R. Shapiro, H. Susa, M. Umemura, and D.J. Whalen. Cosmological radiative transfer codes comparison project - i. the static density field tests. *Mon. Not. R. Astron. Soc.*, 371:1057–1086, September 2006. doi: 10.1111/j.1365-2966.2006.10775.x.

P. Jonsson. Sunrise: polychromatic dust radiative transfer in arbitrary geometries. *Mon. Not. R. Astron. Soc.*, 372:2–20, 2006.

M. Juvela. Efficient monte carlo methods for continuum rediative transfer. *Astronomy & Astrophysics*, 440:531–546, 2005.

T.-S. Kim, S. Cristiani, and S. D'Odorico. The ly-alpha forest at 1.5 < z < 4. *Astronomy & Astrophysics*, 373:757–781, 2001.

A. J. Kinderman and J. F. Monahan. Computer generation of random variables using the ratio of uniform deviates. *Transactions on Mathematical Software*, 3(3):257–260, 1977.

J. Lequeux. *The Interstellar Medium*. Springer, 2005.

R. Lynds. The absorption-line spectrum of 4c 05.34. *Astrophysical Journal*, 164:L73–L78, 1971.

A. Maselli and A. Ferrara. Radiative transfer effects on the ly-alpha forest. *Mon. Not. R. Astron. Soc.*, 364:1429–1440, 2005.

A. Maselli, A. Ferrara, and B. Ciardi. Crash: a radiative transfer scheme. *Mon. Not. R. Astron. Soc.*, 345:379–394, 2003.

A. Maselli, A. Ferrara, M. Bruscoli, S. Marri, and R. Schneider. The proximity effect arround high-redshift galaxies. *Mon. Not. R. Astron. Soc.*, 350:L21–L25, 2004.

M. Matsumoto and T. Nishimura. Mersenne twister: A 623-dimensionally equidistributed uniform pseudo-rondom number generator. *Transactions on Medling and Computer Simulation*, 8(1):3–30, 1998.

C. Maulbetsch, V. Avila-Reese, P. Colín, S. Gottlöber, A. Khalatyan, and M. Steinmetz. The dependence of the mass assembly history of cold dark matter halos on environment. *Astrophysical Journal*, 654:53–65, 2007.

P. McDonald, J. Miralda-Escudé, M. Rauch, W. L. W. Sargent, T. A. Barlow, R. Cen, and J. P. Ostriker. The observed probability distribution function, power spectrum, and correlation function of the transmitted flux in the ly-alpha forest. *The Astrophysical Journal*, 543:1–23, November 2000.

P. McDonald, U. Seljak, R. Cen, P. Bode, and J. P. Ostriker. Physical effects on the ly-alpha forest flux power spectrum: Damping wings, ionizing radiation fluctuations and galactic winds. *Mon. Not. R. Astron. Soc.*, 360:1471–1482, 2005.

G. Mellema, I. T. Illiev, M. A. Alvarez, and P. R. Shapiro. C2-ray: A new method for photon-conserving transport of ionizing radiation. *New Astronomy*, 11: 374–395, 2006.

D. Mihalas. *Stellar Atmospheres*. W.H. Freeman and Company, 1978.

V. Müller and C. Maulbetsch. Simulating the formation of compact groups. *Astronomische Nachrichten Supplement*, 325:107, August 2004.

T. Nakamoto, M. Umemura, and H. Susa. The effects of radiative transfer on the reionization of an inhomogeneous universe. *Mon. Not. R. Astron. Soc.*, 321:593–604, 2001.

M. L. Norman, P. Paschos, and T. Abel. Simulating inhomogeneous reionization. *Mem. S.A.It.*, 1998.

A. Oemler and C. R. Lynds. The absorption spectrum of 4c 25.05. *Astrophysical Journal*, 199:558–564, 1975.

D. E. Osterbrock. *Astrophysics of Gaseous Nebulae and Active Galactic Nuclei*. University Science Books, 2006.

J. A. Peacock. *Cosmological Physics*. Cambridge University Press, 1999.

A. Peraiah. *An Introduction to Radiative Transfer*. Cambridge University Press, 2002.

M. Rauch. The lyman alpha forest in the spectra of quasistellar objects. *Annu. Rev. Astro. Astrophys.*, 36:267–316, 1998.

M. Rauch, W. L. W. Sargent, and T. A. Barlow. Small-scale structure at high redshift. ii. physical properties of the c iv absorbing clouds. *Astrophysical Journal*, 554:823–840, 2001.

A. O. Razoumov and C. Y. Cardall. Full threaded transport enging: New method for multi-scale radiative transfer. *Mon. Not. R. Astron. Soc.*, 362: 1413–1417, 2005.

E.-J. Rijkhorst, T. Plewa, A. Dubey, and G. Mellema. Hybrid characteristics: 3d radiative transfer for parallel adaptive mesh refinement hydrodynamics. *Astronomy & Astrophysics*, 452:907–920, 2006.

J. Ritzerveld. The diffuse nature of strömgren spheres. *Astronomy & Astrophysics*, 439:L23–L26, 2005.

J. Ritzerveld. *The Simplicity of Transport - Triangulating the First Light*. PhD thesis, University of Leiden, Netherlands, 2007.

W. L. W. Sargent, P. J. Young, A. Boksenberg, and D. Tytler. The distribution of lyman-alpha absorption lines in the spectra of six qsos: Evidence for an intergalactic origin. *Astrophysical Journal*, 42:41–81, 1980.

J. Schaye, T. Theuns, M. Rauch, G. Efstathiou, and W. L. W. Sargent. The thermal history of the intergalactic medium. *Mon. Not. R. Astron. Soc.*, 318: 817–826, 2000.

J. Schaye, A. Aguirre, T.-S. Kim, T. Theuns, M. Rauch, and W. L. W. Sargent. Metallicity of the intergalactic medium using pixel statistics. ii. the distribution of metals as traced by civ. *The Astrophysical Journal*, 596:768–796, 2003.

J. Schaye, R. F. Carswell, and T.-S. Kim. A large population of metal-rich, compact, intergalactic civ absorbers - evidence for poor small-scale metal mixing. *Mon. Not. R. Astron. Soc.*, 379:1169–1194, 2007.

P. R. Shapiro and M. L. Giroux. Cosmological hii regions and the photoionization of the intergalactic medium. *Astrophysical Journal*, 321:L107–L112, 1987.

Frank H. Shu. *The Physics of Astrophysics - 1. Radiation*, volume Volume 1. University Science Books, 1991.

Ilya M. Sobol'. *A Primer for the Monte Carlo Method*. CRC Press, 1994.

D. N. Spergel, R. Bean, O. Doré, M. R. Nolta, C. L. Bennett, J. Dunkley, G. Hinshaw, N. Jarosik, E. Komatsu, L. Page, H. V. Peiris, L. Verde, M. Halpern, R. S. Hill, A. Kogut, M. Limon, S. S. Meyer, N. Odegard, G. S. Tucker, J. L Weiland, E. Wollack, and E. L. Wright. Wilkinson microwave anisotropy probe (wmap) three year results: Implications for cosmology. *astro-ph*, astro-ph/0603449, 2006.

L. Spitzer. *Physical Processs in the Interstellar Medium*. Wiley-Interscience Publication, 1998.

V. Springel. The cosmological simulation code gadget-2. *Mon. Not. R. Astron. Soc.*, 364:1105–1134, 2005.

V. Springel, S. D. M. White, A. Jenkins, C. S. Frenk, N. Yoshida, L. Gao, J. Navarro, R. Thacker, D. Croton, J. Helly, J. A. Peacock, S. Cole, P. Thomas, H. Couchman, A. Evrard, J. Colberg, and F. Pearce. Simulating the joint evolution of quasars, galaxies and their large-scale distribution. *Nature*, 7042: 629–636, 2005.

M. Tegmark, M. R. Blanton, M. A. Strauss, F. Hoyle, D. Schlegel, R. Scoccimarro, M. S. Vogeley, D. H. Weinberg, I. Zehavi, A. Berlind, T. Budavari, A. Connolly, D. J. Eisenstein, D. Finkbeiner, J. A. Frieman, J. E. Gunn, A. J. S. Hamilton, L. Hui, B. Jain, D. Johnston, S. Kent, H. Lin, R. Nakajima, R. C. Nichol, J. P. Ostriker, A. Pope, R. Scranton, U. Seljak, R. K. Sheth, A. Stebbins, A. S. Szalay, I. Szapudi, L. Verde, Y. Xu, J. Annis, N. A. Bahcall, J. Brinkmann, S. Burles, F. J. Castander, I. Csabai, J. Loveday, M. Doi, M. Fukugita, J. R. I. Gott, G. Hennessy, D. W. Hogg, Ž. Ivezić, G. R. Knapp, D. Q. Lamb, B. C. Lee, R. H. Lupton, T. A. McKay, P. Kunszt, J. A. Munn, L. O'Connell, J. Peoples, J. R. Pier, M. Richmond, C. Rockosi, D. P. Schneider, C. Stoughton, D. L. Tucker, D. E. Vanden Berk, B. Yanny, and D. G. York. The three-dimensional power spectrum of galaxies from the sloan digital sky survey. *Astrophysical Journal*, 606:702–740, May 2004. doi: $10.1086/382125$.

A. Verhamme, D. Schaerer, and A. Maselli. 3d ly-alpha radiation transfer. *Astronomy & Astrophysics*, 460:397–413, 2006.

D. Whalen and M. L. Norman. A multistep algorithm for the radiation hydrodynamical transport of cosmological ionization fronts and ionized flows. *Astrophysical Journal*, 162:281–303, 2006.